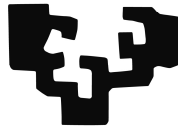


eman ta zabal zazu



Universidad
del País Vasco


Euskal Herriko
Unibertsitatea

Infrared spectral emissivity studies on metals and materials for solar thermal applications

A dissertation presented by

Telmo Echániz Ariceta

telmo.echaniz@ehu.eus

 orcid: orcid.org/0000-0002-0330-0653

In partial fulfillment of the requirements for the Degree
of Doctor in Physics in the Basque Country University

March 2016



Servicio Editorial de la Universidad del País Vasco (UPV/EHU)
- *Euskal Herriko Unibertsitateko (UPV/EHU) Argitalpen Zerbitzua*
- University of the Basque Country (UPV/EHU) Press
- ISBN: 978-84-9082-486-3

Contents

Figure Index.....	7
Table Index.....	13
1 Introduction and objectives	15
2 Experimental: calibration and measurement methods.....	19
2.1 Introduction	21
2.2 Experimental setup.....	21
2.3 Previous measurement and calibration methods	24
2.4 New contributions on the experimental system.....	27
2.4.1 Improvement on the calibration method	27
2.4.2 Improvement on the measurement method.....	29
2.4.3 Temperature measurement.....	35
2.5 Total normal emissivity calculation	38
3 Spectral emissivity of pure metals.....	41
3.1 Introduction	43
3.2 Sample description.....	45
3.3 Copper	47
3.4 Silver	52
3.5 Nickel	56
3.6 Magnesium.....	60
3.7 Hagen-Rubens equation.....	63
3.8 Total normal emissivity	65
3.9 Conclusions.....	66

4	Optical properties of metals: the anomalous skin effect	67
4.1	Introduction	69
4.2	Background.....	70
4.3	Numerical calculations.....	75
4.3.1	Numerical Integrations and series expansions	75
4.3.2	Temperature dependence.....	80
4.3.3	Angular dependence.....	81
4.4	Experimental results.....	83
4.5	Conclusions.....	91
5	Emissivity of solar selective stacks at working temperature	93
5.1	Introduction	95
5.2	Sample fabrication.....	99
5.3	Thermo-radiative properties of solar selective stacks	101
5.3.1	AISI 321 stainless steel substrate	101
5.3.2	Sm ₄ SiO ₂ based stack.....	105
5.3.3	S10 Si ₃ N ₄ based stack.....	108
5.4	Data comparison and total emissivity calculation.....	110
5.5	Conclusions.....	112
6	Emissivity of solar thermal energy harvesting PCM Mg-Zn-Al based alloys	115
6.1	Introduction	117
6.2	Sample description.....	118
6.3	Mg-51%Zn.....	124
6.4	Mg-47%Zn-4%Al	133

6.5 Zn-3%Mg-4%Al	136
6.6 Conclusions.....	142
Appendix I.....	143
Bibliography	157
Resumen en castellano	171
Agradecimientos.....	177
Publication	181

Figure Index

Figure 2.1 Schematic view of the experimental setup.....	22
Figure 2.2 Picture of the HAIRL radiometer at UPV in Leioa.	23
Figure 2.3 Schematic view of the radiometer when the a factor is calibrated. a) Signal measurement from the blackbody side and b) signal measurement from the sample chamber side.	28
Figure 2.4 Signals at $T= 526$ °C from both blackbody (left) and chamber side (right). The peaks in the spectra are due to CO_2 and H_2O absorptions.	28
Figure 2.5 $a(\lambda)$ spectrum between 1.43 and $25 \mu\text{m}$	29
Figure 2.6 Schematic view of a) exiting normal radiation and b) exiting radi- ation at an angle α . The blue arrows refer to the sample emitted radiation; the continuous arrows being transmitted light and the dashed ones the reflected radiation on the KBr window. The red arrows refer to the detector radiation whereas the green ones indicate the surrounding radiation.	30
Figure 2.7 Directional spectral emissivity of platinum at wavelength $\lambda = 2 \mu\text{m}$ [19].	32
Figure 2.8 Directional spectral emissivity of magnesium measured at wave- length $\lambda = 11.5 \mu\text{m}$ at $T= 300^\circ\text{C}$	33
Figure 2.9 Comparison of the calculated emissivity with the previous <i>blacksur</i> method at 0° and the new method at a 10° angle inclination.	34
Figure 2.10 Comparison between the Planck curve at $T= 52$ °C, $T= 60$ °C and the detector contribution.	35
Figure 2.11 Schematic drawings of the three different thermocouple placing methods: a) standard welding (welded together), b) intrinsic welding (welded separately) and c) inserted in holes.	37
Figure 2.12 Method A (Figure 2.11a), Method B (Figure 2.11b) and Method C (Figure 2.11c) temperature measurements normalized to the Method B tem- perature values on an ARMCO iron disc.	38
Figure 2.13 The spectral emissivity curve of pure nickel at $T= 394$ °C with the overestimated and underestimated curves are plotted. The Planck curve at $T=$ 394 °C is also plotted.	40
Figure 3.1 X-Ray diffraction patterns of pure Cu, Ag, Ni and Mg.	46
Figure 3.2 Normal spectral emissivity of copper as a function of temperature at two temperatures for two different cycles.	48

Figure 3.3 Normal emissivity values of copper at 5, 10 and 15 μm for the five cycles at all temperatures.....	49
Figure 3.4 Normal spectral emissivity curves of copper from the fifth cycle at seven different temperatures.....	50
Figure 3.5 Normal spectral emissivity evolution with temperature of copper at 5, 10 and 15 μm on the fifth cycle.	51
Figure 3.6 Comparison between normal spectral emissivity curves from this work at 349 and 445 $^{\circ}\text{C}$ and from Bauer et al. [40] at 400 $^{\circ}\text{C}$	52
Figure 3.7 Normal spectral emissivity of silver as a function of temperature at two temperatures for two different cycles.....	53
Figure 3.8 Normal emissivity values of silver at 5, 10 and 15 μm for the three cycles at six temperatures.....	54
Figure 3.9 Normal spectral emissivity curves of silver from the third cycle at six different temperatures.....	55
Figure 3.10 Normal spectral emissivity evolution with temperature of silver at 5, 10 and 15 μm on the third cycle.	55
Figure 3.11 Normal spectral emissivity of nickel as a function of wavelength at two temperatures for two different cycles.....	56
Figure 3.12 Normal emissivity values of nickel at 5, 10 and 15 μm for the five cycles at all temperatures.....	57
Figure 3.13 Normal spectral emissivity curves of nickel from the fifth cycle at seven different temperatures.....	58
Figure 3.14 Normal spectral emissivity evolution with temperature of nickel at 5, 10 and 15 μm on the fifth cycle.	58
Figure 3.15 Comparison between normal spectral emissivity curves from this work at 394 and 779 $^{\circ}\text{C}$ and from Bauer et al. at 400 $^{\circ}\text{C}$ [40] and Teodorescu et al. at 1167 $^{\circ}\text{C}$ [46] respectively.....	59
Figure 3.16 Normal spectral emissivity of magnesium as a function of wavelength at two temperatures for two different cycles.....	60
Figure 3.17 Normal emissivity values of magnesium at 5, 10 and 15 μm for the five cycles at all temperatures.....	61
Figure 3.18 Normal spectral emissivity curves of magnesium from the fifth cycle at four different temperatures.....	62
Figure 3.19 Normal spectral emissivity evolution with temperature of magnesium at 5, 10 and 15 μm on the fifth cycle.....	63

- Figure 3.20** Comparison between the electrical resistivity data from the literature (lines) and the values from the Hagen-Rubens fitting (dots).64
- Figure 3.21** Total normal emissivity data from copper, silver, nickel and magnesium. The four sets of data are fitted to a linear function.65
- Figure 4.1.** Classical emissivity given by Eq. 4.4 (dotted, green), anomalous skin effect emissivity with $p = 1$ by Eq. 4.7 (solid, red), Eq. 4.10 (dashed, black), Eq. 4.11 (dotted-dashed, blue) and series expansion for $p = 0$ by Eq. 4.12 (long-dashed, pink). a) 80 K, b) 293 K and c) 526 K. The physical parameters used are those for copper from Table 4.1.....76
- Figure 4.2.** a) Predicted classical (Eq. 4.4) and anomalous skin effect emissivities (Eq. 4.7), b) fraction between both anomalous and classical curves and c) anomalous contribution to the emissivity of five metals at room temperature.79
- Figure 4.3.** a) Predicted classical (Eq. 4.4) and anomalous skin effect emissivities (Eq. 4.7), b) fraction between both anomalous and classical curves and c) anomalous contribution to the emissivity of copper at 80 (blue), 293 (red) and 526 K (green).....81
- Figure 4.4.** Classical and anomalous directional spectral emissivity curves obtained with Equation 4.13 for copper at room temperature for four different emission angles. It can be observed that the λ_{max} does not vary.82
- Figure 4.5.** Classical and anomalous directional spectral emissivity values for $\lambda = 20\mu\text{m}$ from 0 to 80 ° for copper at room temperature.83
- Figure 4.6** Normal spectral emissivity curve of copper at 253 °C (526 K)....84
- Figure 4.7** Copper normal spectral experimental emissivity $\varepsilon(\lambda, T)$: (a) from radiometric measurements at 526 K; (b) from room temperature reflectivity measurements [82] and (c) from Equation 4.14 using experimental complex refractive index [20].85
- Figure 4.8** Theoretical and experimental emissivity ratios $\varepsilon/\varepsilon_{clas}$ and $\varepsilon/\varepsilon_{baseline}$ at 526 K and room temperature [20].....88
- Figure 4.9** Spectral emissivity results on copper at 523 K for eight emission angles. The angular dependence is in agreement with the electromagnetic theory and the asymptotic approach of the anomalous skin effect theory.89
- Figure 4.10** Experimental and theoretical copper directional emissivity for three wavelengths at 523 K. The quantitative differences are associated with the surface roughness.90
- Figure 5.1** Solar irradiance (red) and blackbody radiation at 400 °C (black) together with a SAS emissivity at room temperature of Sm4 (blue) and S10 (orange). The green area shows the emissivity of an ideal collector.97

Figure 5.2 Schematic representation of the solar selective coating based in silicon oxide (Sm4).	100
Figure 5.3 Schematic representation of the solar selective coating based in silicon nitride (S10).	101
Figure 5.4 Normal spectral emissivity of AISI 321 stainless for a substrate around 180 and 700 °C on the first and fifth cycle.	102
Figure 5.5 Emissivity evolution with cycling at 5, 10 and 15 μm for three different temperatures.	102
Figure 5.6 Normal spectral emissivity at seven different temperatures for AISI 321 SS.	103
Figure 5.7 Emissivity evolution with temperature at 2.4 5, 10 and 15 μm .	104
Figure 5.8 Normal spectral emissivity of the substrate for various times during the oxidation process in air at T=600 °C.	105
Figure 5.9 Sm4 stack emissivity as a function of the heating cycle at 5, 10, 15 and 20 μm for a) T=325 °C and b) T=600 °C.	106
Figure 5.10 Normal spectral emissivity of the Sm4 stack for five different temperatures in the fourth heating cycle.	107
Figure 5.11 Normal emissivity of the Sm4 stack as a function of temperature at the fourth heating cycle for five different wavelengths.	107
Figure 5.12 S10 stack emissivity as a function of the heating cycle at 4, 8, 14 and 20 μm for a) T=330 °C and b) T=600 °C.	108
Figure 5.13 Normal spectral emissivity of the S10 stack for five different temperatures in the fifth heating cycle.	109
Figure 5.14 Normal emissivity of the S10 stack as a function of temperature at the fifth heating cycle for four different wavelengths.	110
Figure 5.15 Normal spectral emissivity of the SS321 substrate and the Sm4 and S10 stacks.	111
Figure 5.16 Total normal emissivity values calculated with Equations 5.1 and 2.14 for a) Sm4 and b) S10.	112
Figure 6.1 Mg-Zn binary phase diagram.	119
Figure 6.2 Mg-Zn-Al ternary phase diagram.	120
Figure 6.3 Differential Scanning Calorimetry (DSC) measurements for the three eutectic alloys. The Mg-51%Zn and Zn-3%Mg-4%Al alloys show a solid-solid transition around 330 and 275 °C respectively.	122
Figure 6.4 X-Ray diffractograms for a) Mg-51%Zn, b) Mg-47%Zn-4%Al and c) Zn-3%Mg-4%Al.	123

- Figure 6.5** Schematic representations of the five heating cycles where the emissivity measurements are carried out. In each cycle, except in cycle 5, the sample was slowly heated to the measurement temperature (red dots). This temperature is kept constant for the time indicated. In cycle 5 measurements at various temperatures between 225 and 320 °C are made.124
- Figure 6.6** X-Ray diffractograms after the each heating cycle. Each diffractogram (a-d) is indicated in where it was performed in Fig. 6.5 (green dots). For identification purposes the Mg, MgZn, and Mg₇Zn₃ main peaks are labelled in the diffractograms..... 126
- Figure 6.7** Normal spectral emissivity curves for heating cycles 1-4.127
- Figure 6.8** Total normal emissivity variation with time for cycles 1-4: a) Cycle 1, Sequence 2.2 and Cycle 4 at 250 °C and b) Sequence 2.1 and Cycle 3 at 330 °C.....131
- Figure 6.9** Normal spectral emissivity dependence with temperature between 225 and 320 °C..... 132
- Figure 6.10** Normal spectral emissivity spectra of Mg-51%Zn before and after 12 hours in open atmosphere at 310 °C.....133
- Figure 6.11** Time dependent normal spectral emissivity measurements of Mg-47%Zn-4%Al at 325 °C.....134
- Figure 6.12** Temperature-dependent normal spectral emissivity measurements of Mg-47%Zn-4%Al between 200 and 325 °C..... 135
- Figure 6.13** Calculated total normal emissivity for Mg-47%Zn-4%Al.135
- Figure 6.14** Normal spectral emissivity spectra of Mg-47%Zn-4%Al before and after 12 hours in open atmosphere at 325 °C.136
- Figure 6.15** Normal spectral emissivity measurements for Zn-3%Mg-4%Al after 0, 5 and 8 hours at 250 °C.137
- Figure 6.16** a) Total Normal Emissivity values of Zn-3%Mg-4%Al for three different cycles; b) cycle 3 is zoomed around the solid-solid phase transition temperature.139
- Figure 6.17** Normal spectral emissivity of Zn-3%Mg-4%Al at six different temperatures.140
- Figure 6.18** Normal spectral emissivity of Zn-3%Mg-4%Al between 3.5 and 5.5 μm at five different temperatures..... 140
- Figure 6.19** Normal spectral emissivity of Zn-3%Mg-4%Al at four different wavelengths.....141
- Figure 6.20** Normal spectral emissivity spectra of Zn-3%Mg-4%Al before oxidizing and after 12 hours in open atmosphere at 300 °C.142

Table Index

Table 2.1 Device temperature, wavelength, angle and pressure measuring ranges.....	24
Table 3.1 Summary of Cu, Ag, Ni and Mg surface roughness: roughness average (R_a), root mean square roughness (R_q), average maximum height (R_z), and maximum height of the profile (R_t).	47
Table 4.1 Physical parameters of the metals that according to Eq. 4.1 must present an anomalous skin effect spectral region at room temperature, τ is the relaxation time, n_e is the carrier density, ω_p is the Plasmon frequency, σ is the dc conductivity, ρ is the dc resistivity, l is the mean free path, and v_F is the Fermi velocity. The rest of parameters show the strength of the anomalous skin effect on the optical properties and those with an asterisk are calculated for $\lambda = \lambda_{max}$	77
Table 6.1 Summary of the three eutectic alloys surface roughness: roughness average (R_a), root mean square roughness (R_q), average maximum height (R_z), and maximum height of the profile (R_t).	121

1 Introduction and objectives

The metallurgical industry has been and still is a key component of the global economy and even more so within the Basque Country industrial framework. In many of the materials used in this area it is vital to know the radiation heat losses that occur in either the fabrication processes or when the fabricated products are being used. For that it is necessary to study the thermo-radiative and optical properties of these materials, being the spectral emissivity measurement the best way to understand this radiation processes.

The work of this thesis was developed by focusing on three concrete objectives. These objectives were based on the fact that the Basque Country University possesses a High Accuracy Infrared Radiometer in Leioa (HAIRL), unique in Spain, which is able to measure the directional spectral emissivity in the mid-infrared area as a function of temperature in a controlled atmosphere. This thesis was almost entirely made using measurement made in this radiometer.

A brief summary of the three objectives is made in the following paragraphs.

The first objective of this thesis, compiled in Chapter 2, consists on the improvement and completion of the work on the analysis of measurement and calibration methods made by Dr. Leire del Campo and Dr. Luis González during their doctorates. A new measurement method

that improves greatly the measurement of emissivity in low emitting materials by avoiding the detection of spurious signals is developed. Besides, the radiometer is adequately calibrated in order to avoid systematic errors. Methods on temperature measurement and total normal emissivity calculation are also developed.

The second objective, which is divided in Chapters 3 and 4, focuses on the spectral emissivity study in metals. The fact that very little about the emissivity at high temperatures in metals has been studied makes this type of research very compelling. Besides, although the electromagnetic theory provides a qualitative description, it is not possible to obtain valid quantitative values since the theory does not take into account effects provoked by the surface roughness or sample impurities among others. In Chapter 3, the spectral and total emissivities of four low-emitting pure metals are studied between 200 and 800 °C in the mid-infrared area. Their spectral and temperature dependence as well as the evolution of the surface state are also studied.

In Chapter 4 the anomalous skin effect in metals is studied. This phenomenon occurs when the conduction electrons mean free path have the same magnitude order as the electric field penetration depth. The influence of this effect on the spectral emissivity is studied. First, a theoretical analysis of the emissivity for twelve high conducting metals is performed. Then, the experimental results of directional emissivity measurements of copper are compared with the values predicted by the theory.

The last objective, encompassed in Chapters 5 and 6, consists on emissivity measurements of materials used for solar thermal energy applications. Chapter 5 focuses on the solar selective stacks used in solar thermal collectors (STCs). For the first time, normal spectral emissivities at working temperature (200 – 600 °C) are measured. Besides, the need of measuring the emissivity at working temperature, as

opposed to extrapolating reflectivity values from room temperature, is demonstrated.

Finally, in Chapter 6, the radiative properties of three solar energy harvesting alloys are studied. Radiative heat losses are important when analyzing the performance of an energy harvesting material. In this chapter the spectral and total emissivity between 200 °C and the melting point are obtained. The alloys performance at an ambient atmosphere is tested around 300 °C to observe possible oxidations. Solid-solid phase transitions are detected in two alloys by emissivity measurements, which show the radiometer precision when observing small emissivity variations.

2 Experimental: calibration and measurement methods

En este capítulo se indican las principales características del radiómetro HAIRL (diseñado y construido en el laboratorio) utilizado para las medidas de emisividad, las cuales son la base experimental fundamental en esta tesis. Además, se describen brevemente los métodos de medida y de calibración del aparato utilizados previamente. Estos métodos han sido analizados y completados para realizar esta memoria. Las modificaciones introducidas permiten hacer más precisa la medida de la emisividad espectral. Esta mejora es muy notable para los materiales bajoemisivos como los estudiados en este trabajo, donde la radiación emitida por la muestra puede llegar a ser del orden de magnitud de las radiaciones espurias que son detectadas también por el radiómetro. Además, se analizan y añaden otras contribuciones. Por ejemplo, un método de medida de temperatura alternativo a la soldadura intrínseca utilizada anteriormente para muestras metálicas y un método para la integración de los espectros de emisividad.

2 Experimental: calibration and measurement methods

2.1 Introduction

Most of the work presented in this dissertation is based on directional spectral emissivity measurements. The measurements are made using the HAIRL radiometer, designed and constructed in the LAMA laboratory of the Universidad del País Vasco. Since the radiometer has been previously commented in depth [1,2] a brief description with the fundamental aspects will only be made. However, a more detailed explanation of new contributions related to the measurement and calibration methods on one side and temperature measurements on the other is given.

Section 2.2 describes the main parts of the experimental device. Section 2.3 talks about the emissivity measurement and calibration methods. Section 2.4 explains the improvements that notably increased the precision of the measurements. Section 2.4.1 explains the improvements on the calibration methods while Section 2.4.2 does it with the measurement ones. Section 2.4.3 describes how the temperature is measured *in situ* while the emissivity measurements are made. Then, in Section 2.5, the total emissivity calculation from emissivity spectra is explained.

2.2 Experimental setup

The HAIRL (High Accuracy Infrared Radiometer, Leioa) radiometer is composed by four main parts, shown in Figure 2.1: a detection system, a blackbody, an optical entrance and a sample chamber [1,2]. This radiometer allows a direct spectral directional emissivity measurement by comparison between the sample and the blackbody radiation as a

function of temperature. Figure 2.1 shows a schematic view of the experimental device, and a picture of the radiometer is shown in Figure 2.2.

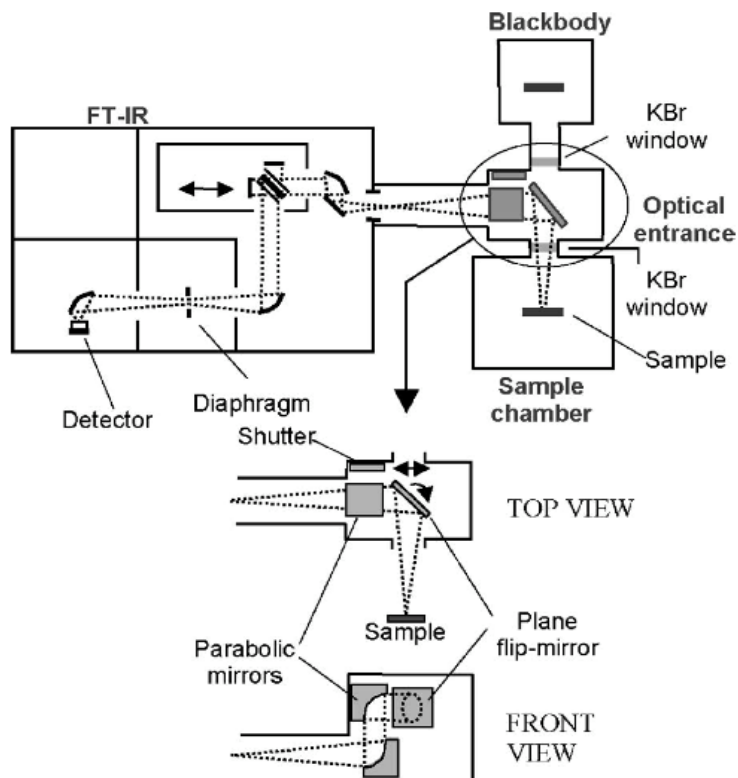


Figure 2.1 Schematic view of the experimental setup.

The detection system is a Fourier Transform Infrared Radiometer (FT-IR) that allows fast signal detection and data processing. There it can be seen that there is a Michelson interferometer and that it also has pyroelectric DLaTGS detector. The wavelength detection range is determined by the detector, the windows of the experimental setup and the beam splitter. In our case the range goes from 1.43 to 25 μm .

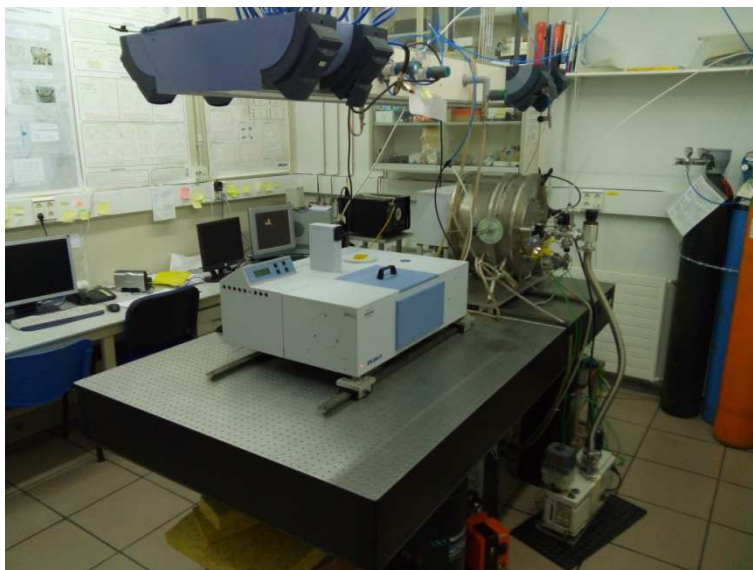


Figure 2.2 Picture of the HAIRL radiometer at UPV in Leioa.

The optical entrance contains two parabolic mirrors that allow changing the radiation plane so it can enter the radiometer parallel to the Michelson interferometer and a rotating plane mirror that allows selecting either the blackbody or the sample radiation. Both the optical entrance and the detection system are connected by a vacuum tube so they can be vacuumed simultaneously. That way, possible absorptions through the optical path are avoided.

A commercial blackbody is used. The oven has a cylindrical graphite cavity with an aperture on its base. The blackbody also has a temperature controller as well as measurement and control thermocouples. In order to avoid water and CO₂ absorptions a purge system has been installed.

A stainless steel cylindrical sample chamber permits either vacuuming or introducing a specific atmosphere (inert, oxidizing or reducing). Inside the chamber a sample holder is placed in the center. The sample holder has a heating system made by a Kanthal® heating wire rolled around an alumina support. It is sustained by a steel axis that allows

changing the emitting angle. Besides, the chamber has a double wall so it can be refrigerated by water. It is also painted in black inside (*Nextel Velvet Coating 811-21* [3]) in order to avoid multiple reflections inside the chamber. This way the background radiation can be diminished considerably.

In Table 2.1 the device measuring ranges are shown:

Table 2.1 Device temperature, wavelength, angle and pressure measuring ranges.

Variable	Measuring Range
Sample Temperature	$>T_{\text{room}} - 1200 \text{ }^{\circ}\text{C}$
Wavelength	1.43 - 25 μm
Angle	0 - 80 $^{\circ}$
Chamber Pressure	$1.5 \cdot 10^3 - 1013 \text{ mbar}$

2.3 Previous measurement and calibration methods

In this section the measurement and calibration methods used previously and developed when the radiometer was built are briefly explained. The emissivity calculation can be done through various methods, and among those the most popular are the direct ones [2,4-7]. Some of these methods, which are usually based on the comparison between the sample and blackbody emission under the same conditions, were studied in a previous paper published by our group [8]. Among those methods, the *blacksur* method is the best suited to use in our laboratory. It does not only take into account the sample radiation, but it also assumes that the surrounding radiation emits as a blackbody at its temperature and then it is reflected on the sample.

Therefore, the exiting sample radiation $L_s^*(\lambda, T_s)$ could be defined as:

$$L_s^*(\lambda, T_s) = \varepsilon_s(\lambda, T_s)L(\lambda, T_s) + [1 - \varepsilon_s(\lambda, T_s)]L(\lambda, T_{sur}), \quad (2.1)$$

where the *s* and *sur* sub indexes refer to the sample and the surrounding, and ε_s is the directional spectral emissivity at temperature T_s . The function $L(\lambda, T)$ refers to directional spectral emission intensities for a blackbody at the sample and surrounding temperatures for Equation 2.1 (T_s and T_{sur}), which are given by the Planck equation:

$$L(\lambda, T) = \frac{2\pi hc^2}{\lambda^5(e^{hc/\lambda k_B T} - 1)}, \quad (2.2)$$

where h is the Planck constant, c is the speed of light and k_B is the Boltzmann constant.

From Equation 2.1 it is deduced that:

$$\varepsilon_s(\lambda, T_s) = \frac{L_s^*(\lambda, T_s) - L(\lambda, T_{sur})}{L(\lambda, T_s) - L(\lambda, T_{sur})}. \quad (2.3)$$

In order to use this equation both the sample and surrounding temperatures and the surrounding radiation must be known. However, the sample signal that the detector measures is $S_s(\lambda, T_s)$, which is not exactly $L_s^*(\lambda, T_s)$. This signal depends on the response function $R(\lambda)$ and the background radiation $S_0(\lambda)$ that is emitted by the radiometer. This signal $S_s(\lambda, T_s)$ can be defined as:

$$S_s(\lambda, T_s) = R(\lambda)L_s^*(\lambda, T_s) + S_0(\lambda). \quad (2.4)$$

This means that the radiometer needs to be calibrated. A proper calibration is fundamental for the measurements to be as precise as possible. In our case the calibration is needed in order to determine the

response function $R(\lambda)$ and the background radiation $S_0(\lambda)$, as seen in Equation 2.4. Therefore, a source whose emissivity is well known should be measured, being a blackbody the ideal candidate. The blackbody signal can be described as:

$$S_{bb}(\lambda, T_{bb}) = R(\lambda)L(\lambda, T_{bb}) + S_0(\lambda), \quad (2.5)$$

where the sub index bb refers to the blackbody.

There are various methods for obtaining both $R(\lambda)$ and $S_0(\lambda)$ [7,9-16]. In our case, the modified two-temperature method is the chosen one [17]. This method consists of two measurements: one high-temperature blackbody measurement and a shutter measurement at room temperature in the blackbody position. The shutter is a metallic plate covered with the *Nextel Velvet Coating 811-21* that has a known emissivity $\varepsilon_{sh} = 0.975$ [18]. This method allows doing a faster calibration by not needing the blackbody to stabilize at two different temperatures [1,8].

Since there are two radiometer sources situated to the left and right of the optical entrance, another factor needs to be taken into account in its calibration. It cannot be assumed that for the same sample the signal detection is identical from the sample chamber side and from the blackbody side. This means that for the signals measured for the blackbody, the shutter and the sample we have the following formulas:

$$\begin{aligned} S_{bb}(\lambda, T_{bb}) &= R_L(\lambda)L(\lambda, T_{bb}) + S_{0L}(\lambda) \\ S_{sh}(\lambda, T_{sh}) &= R_L(\lambda)\varepsilon_{sh}L(\lambda, T_{sh}) + S_{0L}(\lambda) \\ S_S(\lambda, T_S) &= R_R(\lambda)L_S^*(\lambda, T_S) + S_{0R}(\lambda), \end{aligned} \quad (2.6)$$

where the sh , L and R subindexes refer to shutter and the left and right side incoming radiation respectively. Until now it has been considered that both left and right background radiations ($S_{0L}(\lambda)$ & $S_{0R}(\lambda)$) are independent from the incoming side and therefore equal, whereas response varies by a factor named a , which is considered independent of the radiation wavelength:

$$a = \frac{R_R(\lambda)}{R_L(\lambda)} = 1.08, \quad (2.7)$$

By combining Equations 2.3, 2.6 and 2.7 we obtain the emissivity formula:

$$\begin{aligned} \varepsilon_s(\lambda, T_s) = & \frac{1}{a} \frac{S_s(\lambda, T_s) - S_{sh}(\lambda, T_{sh})}{S_{bb}(\lambda, T_{bb}) - S_{sh}(\lambda, T_{sh})} \frac{L(\lambda, T_{bb}) - \varepsilon_{sh}L(\lambda, T_{sh})}{L(\lambda, T_s) - L(\lambda, T_{sur})} + \\ & + \frac{\frac{\varepsilon_{sh}L(\lambda, T_{sh})}{a} - L(\lambda, T_{sur})}{L(\lambda, T_s) - L(\lambda, T_{sur})}. \end{aligned} \quad (2.8)$$

2.4 New contributions on the experimental system

2.4.1 Improvement on the calibration method

The spectral dependence of the a factor and the possible presence of spurious signals unanalyzed until now are analyzed so that the radiometer precision can be incremented. In order to measure the a factor, an emission source placed inside a cylinder is used at both sides of the optical entrance (see Figure 2.3). A k-type thermocouple is used in order to measure the temperature of the emission source. The signal is measured from both the blackbody (Figure 2.3a) and the sample chamber side (Figure 2.3b) from the focal points on both sides several times and at different temperatures when the temperature is stabilized.

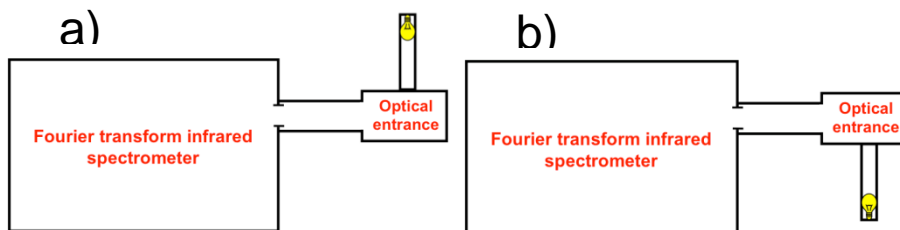


Figure 2.3 Schematic view of the radiometer when the a factor is calibrated. a) Signal measurement from the blackbody side and b) signal measurement from the sample chamber side.

Figure 2.4 shows two signal curves measured from both sides. It can be seen that at the same temperature, the incoming signal from the sample chamber side is indeed stronger than the one from the blackbody. Nevertheless, the quotient between both signals is wavelength dependent as it is observed in Figure 2.5. Various signal curves were used in order to obtain a mean value. As we can see, it significantly varies from the constant value 1.08 used previously.

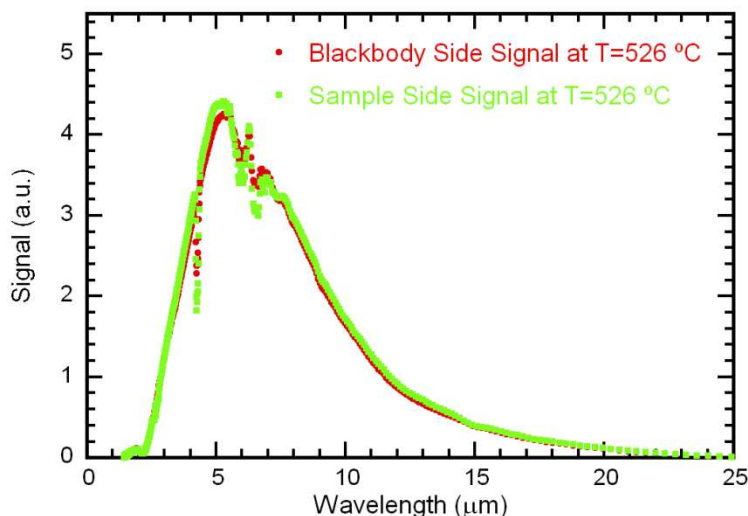


Figure 2.4 Signals at $T = 526$ °C from both blackbody (left) and chamber side (right). The peaks in the spectra are due to CO_2 and H_2O absorptions.

Besides, it will be considered that the background radiation also depends on the a factor:

—

This fact modifies Equation 2.7 and it will be taken into account later when the emissivity formula is reformulated.

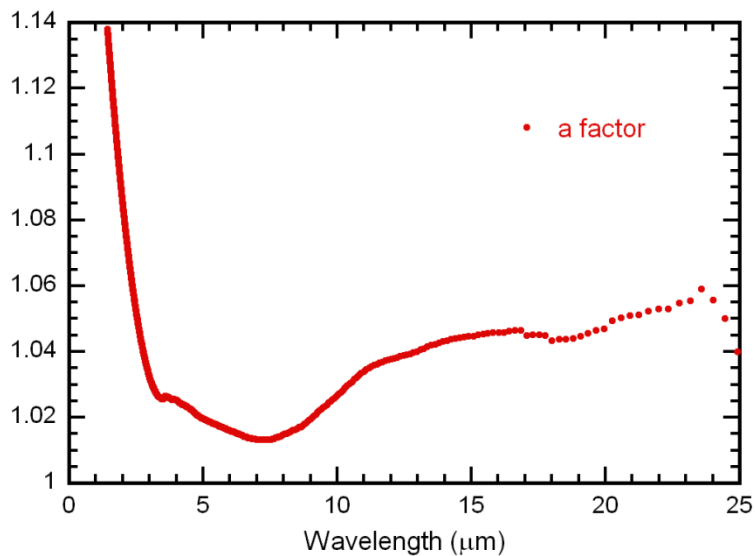


Figure 2.5 spectrum between 1.43 and 25 μm .

2.4.2 Improvement on the measurement method

Besides the wavelength dependence of the a factor, the contribution from two spurious signals is analyzed. In Equation 2.1, the *blacksur* method assumes that the only exiting radiation coming from the chamber outside the sample radiation is the chamber emission reflected by the sample. Nevertheless, when normal spectral emissivity is detected, two extra radiation sources need to be taken into account. The detector emits radiation that follows the inverse optical path of the sample

signal by entering the chamber and then it is reflected on the sample only to go back to the detector. Besides, the sample emission that is reflected on the KBr window, then reflected again on the sample and finally detected in the FTIR needs to be taken into account as well. These two signals are especially relevant when measuring highly reflecting materials such as metals. When calculating the first of these spurious signals it must be remembered that there is an extra signal loss of the detector radiation due to the optical entrance as the signal goes through the optical path twice.

At the same time, when studying materials whose reflection is mostly specular, the second term from the *blacksur* method ($[1 - \varepsilon_s(\lambda, T_s)]L(\lambda, T_{sur})$) should be neglected since the sample will reflect the chamber radiation specularly only to be reabsorbed later somewhere inside the chamber. If the sample is perpendicular to the optical path this radiation cannot be detected due to the specular reflection (Figure 2.6a).

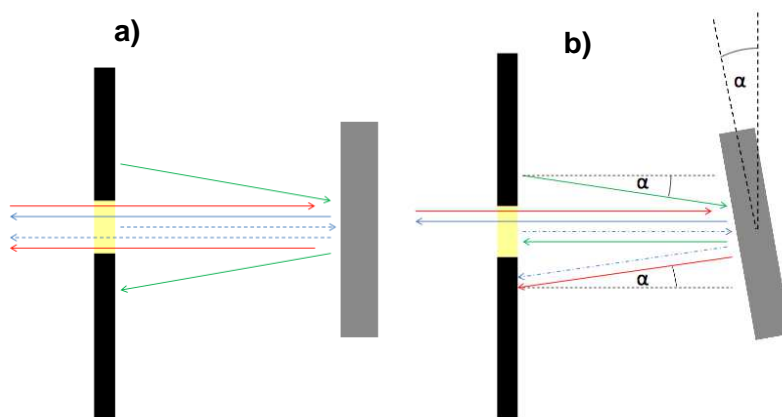


Figure 2.6 Schematic view of a) exiting normal radiation and b) exiting radiation at an angle α . The blue arrows refer to the sample emitted radiation; the continuous arrows being transmitted light and the dashed ones the reflected radiation on the KBr window. The red arrows refer to the detector radiation whereas the green ones indicate the surrounding radiation.

The samples studied in this work are all low emitting materials, and therefore the assumptions made previously are correct for the emissivity calculations shown in this dissertation. If we take into account all the previously described factors the following equation for normal radiation is obtained:

$$L_s^*(\lambda, T_s) = \varepsilon_s(\lambda, T_s)L(\lambda, T_s) + \varepsilon_{det}(\lambda, T_{det})\mathcal{T}_{KBr}F_{opt}[1 - \varepsilon_s(\lambda, T_s)]L(\lambda, T_{det}) + \varepsilon_s(\lambda, T_s)L(\lambda, T_s)\mathcal{R}_{KBr}[1 - \varepsilon_s(\lambda, T_s)], \quad (2.10)$$

where \mathcal{T}_{KBr} and \mathcal{R}_{KBr} are the KBr window transmittance and reflectance respectively and the *det* subindex refers to the detector. F_{opt} is a signal loss factor given by the mirrors, the beam splitter and other devices used in the optics. Both F_{opt} and \mathcal{T}_{KBr} are factors of the response function where $R = \mathcal{T}_{KBr}F_{opt}\mathcal{D}_{det}$, being \mathcal{D}_{det} the DLaTGS detector detectivity. These two factors appear since the detector emitted radiation travels through the optical path twice and therefore they need to be taken into account.

This equation would be very difficult to solve since we do not know the detector temperature and emissivity. However, as we can see in Figure 2.7, the spectral emissivity of metals follows Lambert's cosine law [19], and therefore the emissivity almost does not vary in the 0-20 ° range. In fact, if we take the complex refractive index values from copper at room temperature between 1 and 25 μm [20] we can see that the emissivity value between normal emission angle and a 10° angle varies only 0.01%.

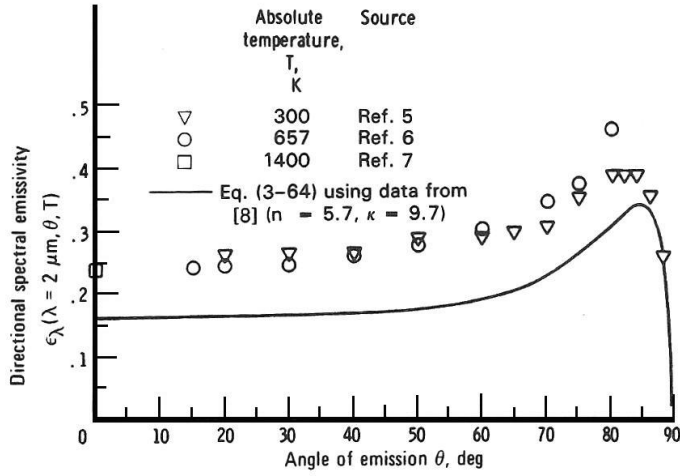


Figure 2.7 Directional spectral emissivity of platinum at wavelength $\lambda = 2 \mu\text{m}$ [19].

This means that the Equation 2.1 of the Blacksour method can in fact be used as long as the sample is inclined to a certain degree. This is because, from a certain angle onwards, the reflected radiation coming from the detector and the KBr window will go onto the chamber walls and at the same time, the radiation emitted by the chamber will be reflected by the sample and then detected (Figure 2.6b). Therefore, we can finally rewrite the emissivity equation:

$$\varepsilon_s(\lambda, T_s) = \frac{\frac{S_s(\lambda, T_s) - a(\lambda)S_{sh}(\lambda, T_{sh})}{a(\lambda)R(\lambda)} + \varepsilon_{sh}L(\lambda, T_{sh}) - L(\lambda, T_{sur})}{L(\lambda, T_s) - L(\lambda, T_{sur})}, \quad (2.11)$$

where $R(\lambda) = R_L(\lambda)$.

The previous formula will only be valid as long as the emission angle is large enough for the detector and the KBr reflected radiation not to be detected and at the same time small enough for the emissivity to be equivalent to the normal emissivity.

Figure 2.8 is displayed in order to experimentally confirm the assumption made until now. It shows, as an example, the measured magnesium emissivity at $11.5 \mu\text{m}$ between -70 and 70° . As we can see the emissivity values strongly decrease down to 6° and stay stable up until around 20° . Except for very small angles, the measurements give values predicted by Lambert's cosine law. The previously described spurious contributions appear nearby the normal incidence angle, as it can be seen in Figure 2.8. Therefore the measurements between 6 and 20° do not have an angular dependence. As a consequence, the measurements made in this work will be done at a 10° angle, although the measurements will be referred as normal spectral emissivity measurements unless it is stated otherwise.

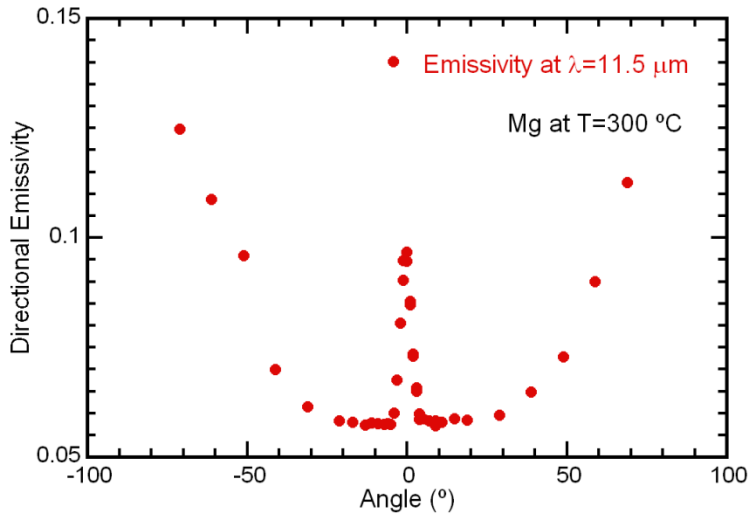


Figure 2.8 Directional spectral emissivity of magnesium measured at wavelength at $T=300^\circ\text{C}$.

In order to see the difference influence of the spurious reflections in the entire mid-infrared spectra, curves of the Mg-47%Zn-4%Al (mass %) alloy at 325°C are plotted in Figure 2.9. The difference between both curves is notable since the signal coming from a low emitting

sample at low temperature is comparable with the spurious detected signal. It can be noticed that the emissivity of both curves tend to the same value at short wavelengths. This happens due to two factors: on one hand the detector radiation emission is almost non-existent below $4 \mu\text{m}$ since it is emitted at a much lower temperature ($50 \text{ }^\circ\text{C}$). On the other, the average height of the surface roughness profile ($1 \mu\text{m}$) of this sample is comparable to short wavelengths of the studied emissivity spectrum and therefore the surface is not as smooth as it is for longer wavelengths. As a consequence, the radiation at shorter wavelengths is not as specularly reflected as it is at longer ones and less radiation reflected by the sample should be detected.

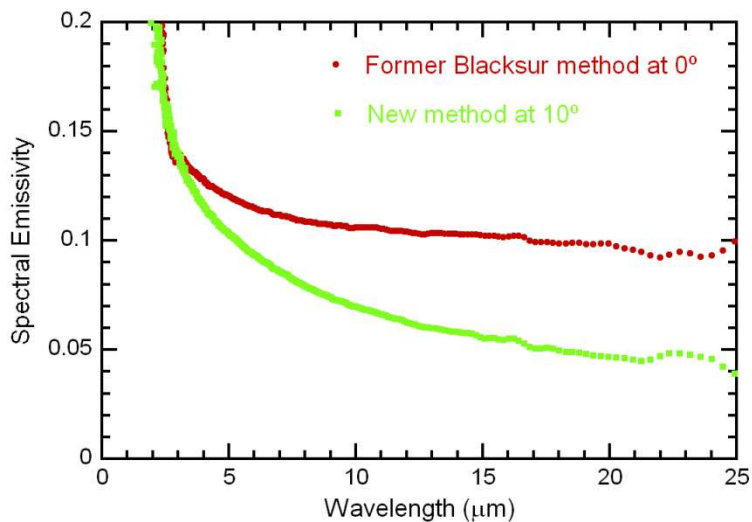


Figure 2.9 Comparison of the calculated emissivity with the previous *blacksor* method at 0° and the new method at a 10° angle inclination.

Finally, the detector emission contribution is quantified since it is the only emission source we consider where we are not able to determine its emissivity and its temperature. For that we use the signal values from the Mg-47%Zn-4%Al alloy from which we calculated the emissivities in Figure 2.9. Those two emissivities are obtained by using

the former *blacksur* method and the new method described in Equation 2.10 for 0° and Equation 2.11 for 10° respectively. By combining both, the following equation is obtained:

$$\frac{L_{\text{det}}}{L_{\text{Planck}}} = \frac{F_{\text{opt}} \epsilon_{\text{det}}}{\epsilon_{\text{obj}}}$$

Figure 2.10 shows the detector contribution for the Mg-47%Zn-4%Al alloy at 325°C whose emissivity was shown previously compared to the Planck function at 52°C and 60°C . The KBr window is considered to have a $R_{\text{KBr}} = 0.083$ [21] and $T_{\text{KBr}} = 0.9$ [22].

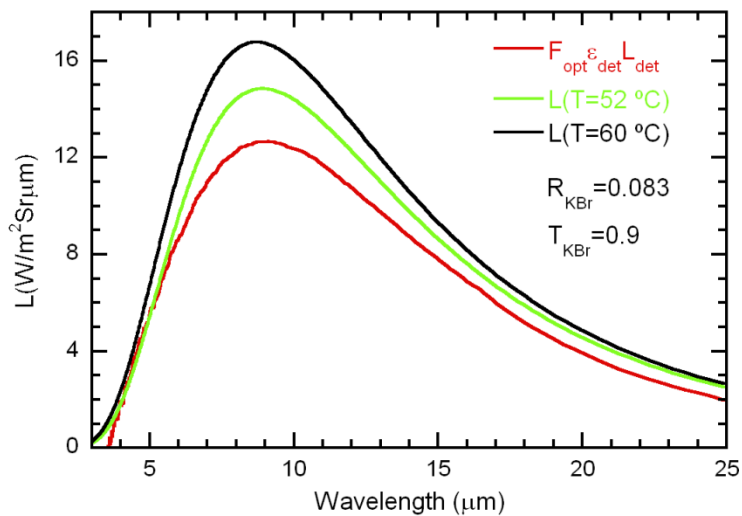


Figure 2.10 Comparison between the Planck curve at $T= 52^\circ\text{C}$, $T= 60^\circ\text{C}$ and the detector contribution.

2.4.3 Temperature measurement

One of the most important factors to consider while measuring the emissivity is the temperature. The main reason for this is that even

slight errors in the temperature measurements can provoke erroneous calculations on the emissivity due to the Planck function (Equation 2.2) strong temperature dependence.

In the HAIRL case, four different temperatures are needed for each emissivity measurement. The blackbody and shutter temperatures are needed to obtain $R(\lambda)$ and $S_0(\lambda)$. Besides, the sample and the surrounding chamber temperatures are necessary, as indicated in Equation 2.10. All the temperatures are measured by means of a thermocouple. K-type thermocouples are used for all the temperature measurements, except for the blackbody ones (R-type).

Among all these measurements the sample temperature measurement is by far the most difficult one. The thermocouples must be placed outside the measured spot (with a 4 mm diameter approx.) so they are not seen by the detector and at the same time stay in a place where the temperature is homogeneous. Previous studies about the temperature homogeneity indicate that the thermocouples placed at 5 mm from the measuring spot centre and in diametrically opposed positions will have the temperature homogeneity ensured [1].

In order to place the thermocouples on the sample three different techniques can be used as it can be seen in Figure 2.11. In the first one, in Figure 2.11a, two thermocouple wires are first welded to each other and then welded onto the sample. This technique has a large drawback: the thermocouple will measure the temperature on the thermocouple welding spot, which depending how well they are welded can be far away from the surface, causing large errors on the temperature measurement. In Figure 2.11b the two wires are welded separately onto the sample surface and as close to each other as possible. This is known as the intrinsic measurement method [23] and it has the advantage that the thermocouple union is made on the surface, improving considerably the temperature measurement.

A third option, shown in Figure 2.11c, was developed during the course of this work. In the case where thermocouples cannot be welded, pairs of holes of the same diameter as the thermocouple wires can be made so they can be introduced across the sample. This way the thermocouple union will also be made on the surface.

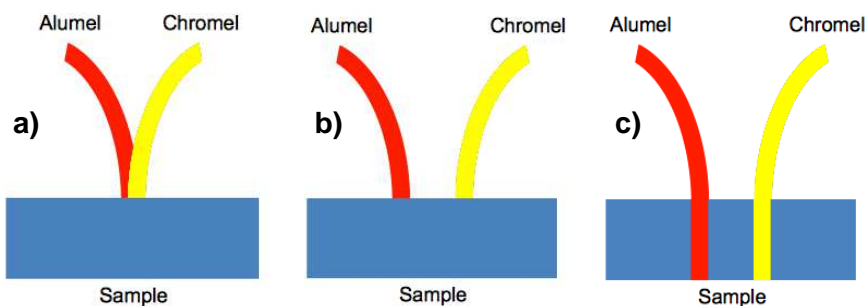


Figure 2.11 Schematic drawings of the three different thermocouple placing methods: a) standard welding (welded together), b) intrinsic welding (welded separately) and c) inserted in holes.

In order to show the thermocouple performance, Figure 2.12 shows the measured temperature evolution with the three methods normalized to the temperature measured by the second method on an ARMCO iron sample. As we can see both the intrinsic method and the hole method present very similar temperature measurements with a maximum temperature variation of a 0.3% while the first method measurements fluctuate much more and can reach variations of over 1%.

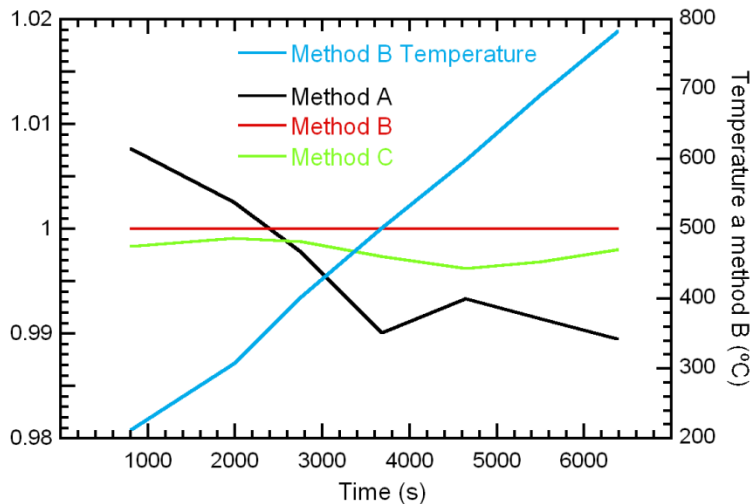


Figure 2.12 Method A (Figure 2.11a), Method B (Figure 2.11b) and Method C (Figure 2.11c) temperature measurements normalized to the Method B temperature values on an ARMCO iron disc.

2.5 Total normal emissivity calculation

When we obtain the spectral emissivity curves it is very useful to obtain the integrated value along the entire spectrum in order to extract extra information from the piece of data obtained that otherwise would be very difficult to interpret.

In order to do that we need to use the following formula:

However, we cannot use this formula straightforwardly since we can only possess information about the emissivity spectra between 1.43 and 25 μm . Fortunately, around 98% (depending on the measured temperature) of the emitted radiation is between those wavelength values.

Besides, it happens that sometimes, especially at very low temperatures, for radiation at very short wavelengths (i.e. $\lambda < 2 \mu\text{m}$) and for very large wavelengths (i.e. $\lambda > 22 \mu\text{m}$), the emissivity values that are obtained are not accurate enough and therefore need to be disregarded.

So when the emissivity is integrated along the electromagnetic spectrum, the gaps where the emissivity is unknown need to be filled. For that we need to take into account that for metallic materials the emissivity monotonously decreases while the wavelength increases. Therefore, two integrals will be calculated: one where the emissivity values on the unknown areas are overestimated and another one where the emissivity values are underestimated. In the overestimated curve, the emissivity values at short wavelengths will be given a maximum value of one, whereas at longer wavelengths, where the emissivity is supposed to decrease, the last valid emissivity value is considered to be constant and therefore it does not decrease in the far-infrared area. Analogously, in the underestimated curve at short wavelengths the emissivity value given is the one of the last wavelength where we obtain a valid emissivity value and at longer wavelengths a value of zero will be given.

This can be observed in Figure 2.13, where both underestimated and overestimated curves are shown with the actual measured emissivity spectrum. Finally, the mean value of both integrals will be calculated in order to have a more accurate value.

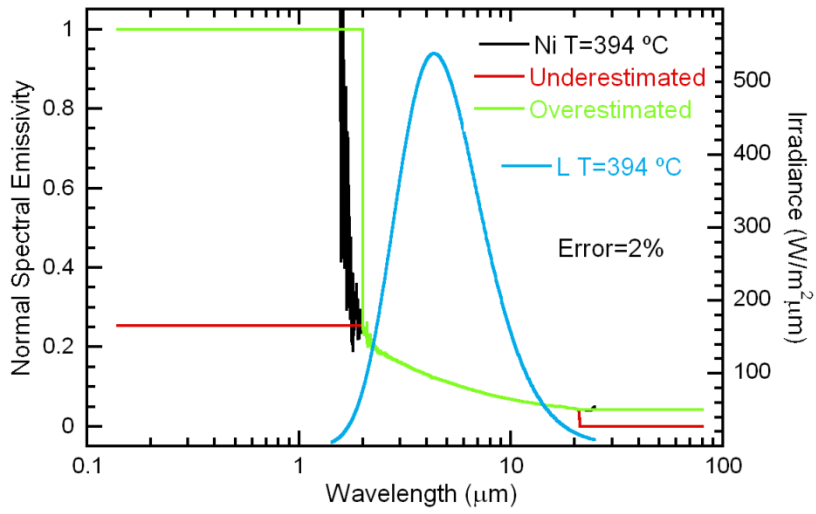


Figure 2.13 The spectral emissivity curve of pure nickel at $T= 394\text{ }^{\circ}\text{C}$ with the overestimated and underestimated curves are plotted. The Planck curve at $T= 394\text{ }^{\circ}\text{C}$ is also plotted.

3 Spectral emissivity of pure metals

La ausencia de estudios en los que aparezcan bien definidas las condiciones experimentales de la emisividad espectral en función de la temperatura de la mayoría de los metales puros ha impulsado el trabajo presentado en este capítulo. Aquí se presentan brevemente las medidas de emisividad del cobre, la plata, el níquel y el magnesio, cuatro metales presentes, tanto en su estado puro como en aleaciones, en diversas aplicaciones industriales. Entre otros aspectos, se estudia la relajación de tensiones superficiales producidas en el mecanizado de las muestras, así como las dependencias con la temperatura y la longitud de onda de la emisividad. Además, se analizan las curvas de emisividad dentro de la aproximación clásica dada por la función de Hagen-Rubens. Esto ha permitido obtener valores de la resistividad eléctrica y compararlos con los encontrados en la bibliografía. Por último, pensando en aplicaciones industriales, se hace un cálculo de la emisividad normal total y se observa su dependencia lineal con la temperatura.

3 Spectral emissivity of pure metals

3.1 Introduction

Pure metals emissivity measurements are of interest for two main reasons. On one hand, it allows demonstrating the radiometer precision even with very low emitting materials. On the other, knowledge of the radiative properties of pure metals is essential for many applications related to the heat transfer in energy, industrial and scientific processes. Direct absolute measurements of the radiative properties are of great importance because of the theoretical relations between these physical quantities and the optical and electrical properties of materials [19,24]. In particular, experimental radiative measurements in metals have great interest for mid and far infrared frequencies as the direct measurement of optical constants on metals in this spectral range offers serious difficulties. Only room temperature experimental values of optical constants can be found [20,25-28]. This explains the discrepancies between the emissivity calculated by using experimental optic constants via the classical electromagnetic equations [19,24] and those experimental values obtained with a radiometer. On the other hand, some discrepancies appear because real materials do not meet the ideal surface conditions assumed by the theory. Their radiative and optical properties are highly influenced by the surface state, and depend on surface roughness, oxidation, surface contamination, impurities, thermal uniformity, etc. This fact explains the differences among experimental emissivity values found in the literature when the measurements are carried out with samples without a good characterization of their surface state or without adequate atmosphere control. At the present time, radiometers with a proper sample holder and a FT-IR spectrometer allow faster and more accurate measurements of the radiative properties as a function of wavelength, temperature and

emission angle in a controlled atmosphere. If one adds the possibility of controlling the surface state, the radiative properties measurements may increase significantly the knowledge of optical and electrical properties of materials.

In this chapter the radiative properties of four pure elements, copper, silver, nickel and magnesium, are widely studied. These metals were chosen since, at this moment, there is only a partial experimental knowledge of their radiative properties in the mid-infrared range. Nevertheless, all these metals except for magnesium are employed in applications in which the knowledge of their radiative properties is very important. Copper is, for example, largely used for electrical wires, heat sinks and heat exchangers. Silver is also used for heat exchangers, but also in low emissivity coatings and many other applications. Nickel is used to provide hardwearing decorative and engineering coatings, and plays an important role in alloys developed for a great number of specific and general purposes. Recently, some of these metals have been studied due to their effectiveness for decreasing the emissivity of coatings and as diffusion barrier layers between low-emissivity films and substrates [29-31]. Anyway, one can find some experimental data in the literature about the optical and electrical properties in the infrared spectral range of both metals. The total hemispherical emissivity of copper was measured at different temperatures [32-35]. Its normal spectral emissivity was studied at its melting point [36-38], above the melting point [39], between room temperature and 750 °C at 1.55 μm and at 400 °C [40]. The total hemispherical emissivity of silver was also studied at different temperatures [32,34,41], and the normal spectral emissivity at its melting point [36,38] and at 150 °C [42], where the total directional emissivity was also studied. In the case of nickel, its total normal emissivity was measured for different surface states [43], whereas its total hemispherical emissivity was obtained in

the 77–737 °C range using calorimetric techniques [44]. The normal spectral emissivity was measured at 400 °C [40] using a radiometer, and a few discrete data were calculated from optical constants [45]. Additional spectral emissivity values were obtained between 1167 and 1332 °C for a high-purity nickel sample [46] and at its melting point with a pulse-heating technique [47]. The radiance temperature of nickel at its melting point [48] and the optical properties of liquid nickel were also measured [49]. However, a systematic study of its directional spectral emissivity as a function of the temperature has not been found. As far as we know, there are no pure magnesium emissivity studies of any kind.

In this work, the copper, silver, nickel and magnesium emissivity dependence on temperature and wavelength is studied in the mid-infrared range using a high accurate radiometer. The results obtained in this study are compared to the few experimental measurements available in the literature for the same temperature range. In addition, using the electromagnetic theory, experimental data are compared to literature data from electrical measurements. Finally, the total normal emissivity will be calculated.

3.2 Sample description

For copper, a high purity (>99.9%) sample of electrolytic copper is used. A film of this metal with a thickness greater than 36 μm was deposited on a 60 mm diameter and 3 mm thick Armco iron disc. In the case of silver and nickel, Goodfellow ® sputtering targets of very high purity (>99.99%) with a 50 mm diameter and 3.2 mm thickness are used. The magnesium sample is a commercial one and has a purity of 99.94%. Its dimensions are 40x40 mm with a 2 mm thickness. Except for the copper sample, where the thermocouples were welded on to

the ARMCO iron, the temperature is measured by placing the thermocouple wires across 0.5 mm holes drilled in the sample.

In order to make sure that the samples are pure enough X-Ray diffraction patterns are obtained. Figure 3.1 plots the four diffractograms of the four different metals.

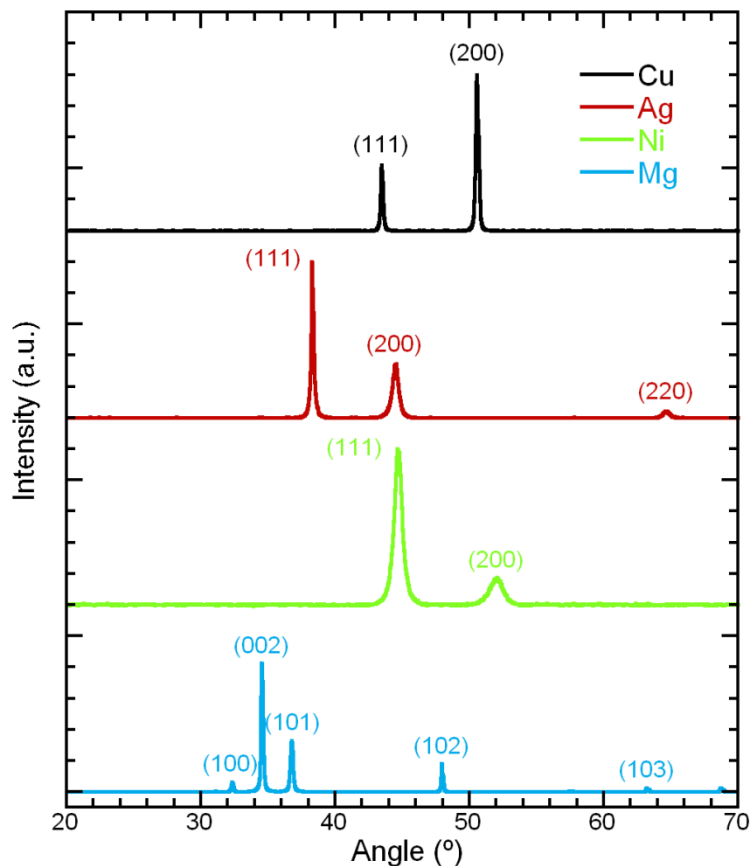


Figure 3.1 X-Ray diffraction patterns of pure Cu, Ag, Ni and Mg.

Finally, the samples roughnesses were measured using a conventional rugosimeter and the obtained values are showed in Table 3.1. It must be noticed that the surface roughness has no significant effect on the infrared emissivity in some coatings [50], but it has noticeable effect in metals in the near infrared [51].

Table 3.1 Summary of the Cu, Ag, Ni and Mg surface roughness: roughness average (R_a), root mean square roughness (R_q), average maximum height (R_z), and maximum height of the profile (R_t).

Sample	R_a (μm)	R_q (μm)	R_z (μm)	R_t (μm)
Cu	1.22	1.43	7.12	8.02
Ag	0.02	0.02	0.11	0.14
Ni	0.01	0.02	0.10	0.11
Mg	0.25	0.33	2.15	2.99

3.3 Copper

The measurements have been made following this experimental procedure. Once a sample is introduced in the sample chamber a moderate vacuum is made inside with a rotary pump. Then, before the sample is heated up to the measurement temperatures, a slightly reducing atmosphere ($\text{N}_2 + 5\% \text{H}_2$) is introduced into the chamber in order to prevent the oxidation of the sample surface. The measurements are carried out during five successive heating thermal cycles between room temperature and 810 °C approximately. For each heating cycle the emissivity is measured at seven temperatures between 250 °C and the maximum temperature with temperature steps of around 100 °C. The temperature must be stabilized before measuring the emissivity. The error analysis has been made in previous works [8,17,52].

Normal spectral emissivity measurements have been carried out between 3 and 21 μm for each cycle. Figure 3.2 shows the spectral emissivity curves at the lowest and highest measured temperatures from the first and fifth cycle.

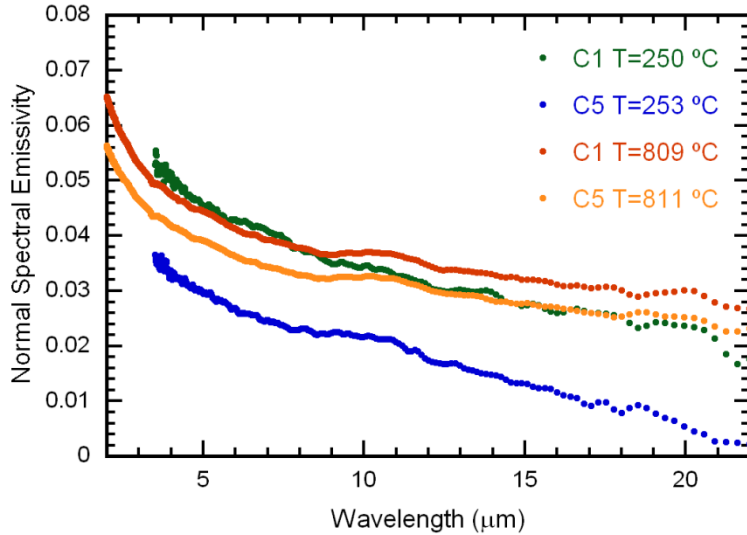


Figure 3.2 Normal spectral emissivity of copper as a function of temperature at two temperatures for two different cycles.

The emissivity decreases with the wavelength, as predicted by the electromagnetic theory [19,24]. On the other side, the experimental results show a significant decrease in the emissivity values between the first and the fifth thermal cycle. A similar behavior was previously seen in other metallic materials such as Armco iron and Ti-6Al-4V alloy [53,54]. This behavior is associated to a surface stress relaxation process. The first heating cycle acts as an annealing process that relieves the surface stresses. This explains why the emissivity during the fifth thermal cycle is lower than during the first one and the difference in the emissivity value between the first and fifth thermal cycles in Fig. 3.2 is larger for the lowest temperature than for the highest. This is due to the measurement method used in this study, in which the temperature is stabilized during 20 min every 100 °C approximately in order to measure the emissivity. Thus, during the first cycle, at around 250 °C, the sample still retains all the surface stress, but, at around 810 °C, it has accumulated a significant stress relaxation produced in the previous temperature steps. Therefore, during the first heating cycle the

relaxation kinetics has already begun before the last temperature step. This feature was extensively analyzed for titanium alloys [54].

In order to have a better comprehension of the relaxation processes between the first and fifth cycle, we can see in Figure 3.3 the emissivity evolution with the cycles at three different wavelengths (5, 10, and 15 μm) for all the measured temperatures.

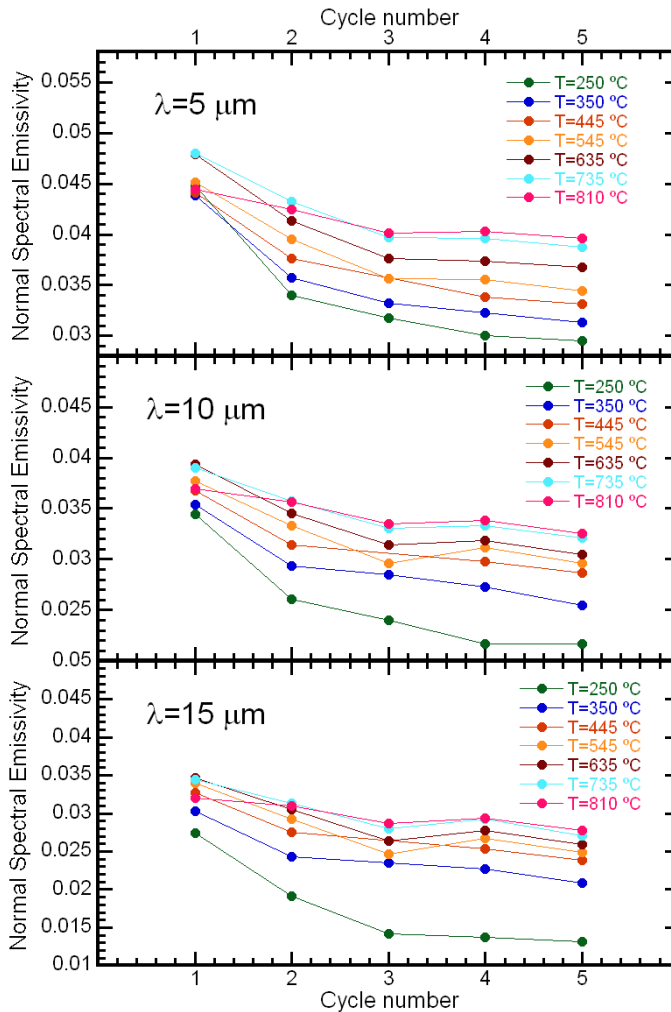


Figure 3.3 Normal emissivity values of copper at 5, 10 and 15 μm for the five cycles at all temperatures.

As we can see in all three wavelengths there is a clear evolution between the first and third cycle where the emissivity decreases. In fact, in this graphs it can be seen how the emissivity increases with temperature, but when looking at the first cycle the emissivity at 810 °C is already lower than the one measured at 545 °C. This is in agreement with what it was stated before, the relaxation processes have already begun during the first cycle. After the third cycle though, we can see that the emissivity has stabilized.

In Figure 3.4 the normal spectral emissivity curves between 3 and 22 μm from the last cycle are plotted. Here, once the sample has been totally relaxed we can see more clearly how the emissivity evolves with the wavelength and the temperature. Here we can see more clearly how the emissivity decreases while the wavelength increases. However, we can see a plateau region between 8 and 12 μm . This matter will be later discussed in Chapter 4. We can also see how the emissivity clearly increases with temperature.

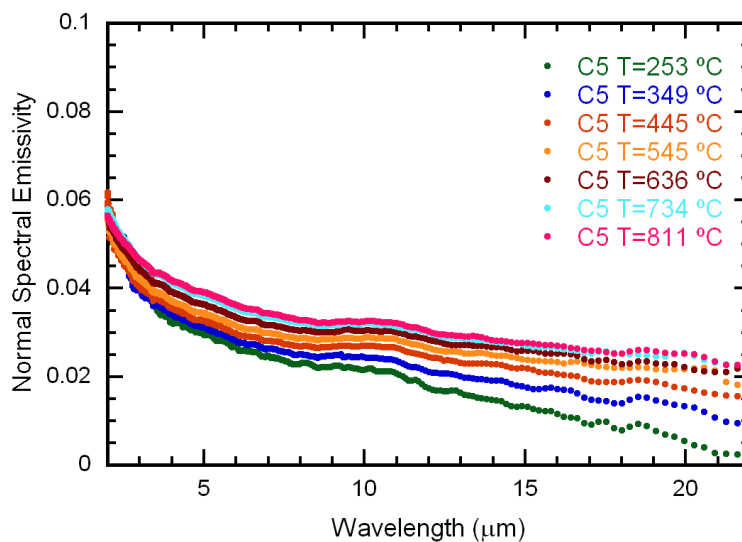


Figure 3.4 Normal spectral emissivity curves of copper from the fifth cycle at seven different temperatures.

In order to see this behavior more clearly, Figure 3.5 shows the emissivity dependence on temperature at three wavelengths. At short wavelengths ($5 \mu\text{m}$) the normal spectral emissivity of copper increases linearly while at longer wavelengths ($15 \mu\text{m}$) it has a parabolic evolution.

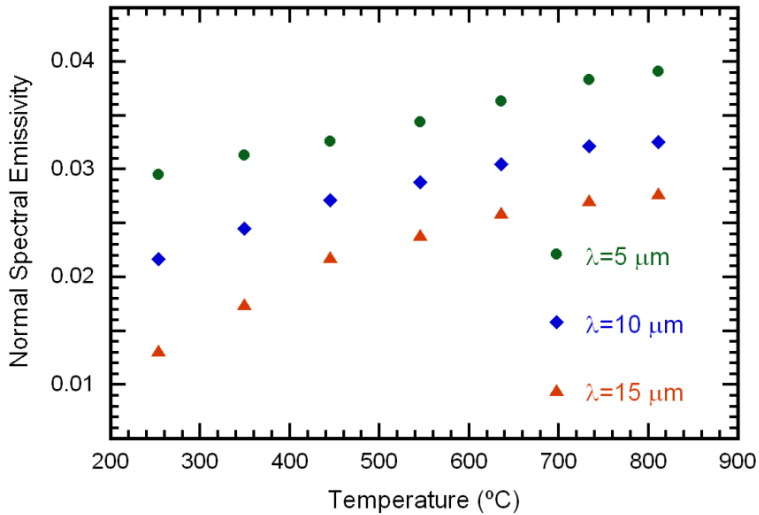


Figure 3.5 Normal spectral emissivity evolution with temperature of copper at 5, 10 and $15 \mu\text{m}$ on the fifth cycle.

Finally, in Figure 3.6, the normal spectral emissivity curves from the fifth cycle at 349 and 445 °C are compared with the curve obtained by Bauer et al. [40] at 400 °C. There is quite a good agreement between the curves even though there are a few discrepancies. This discrepancies at short wavelengths are probably related to the surface state. Even if we do not know anything about the sample Bauer measured, less rough samples tend to have lower emissivities at shorter wavelengths and the copper sample measured in this work was not polished.

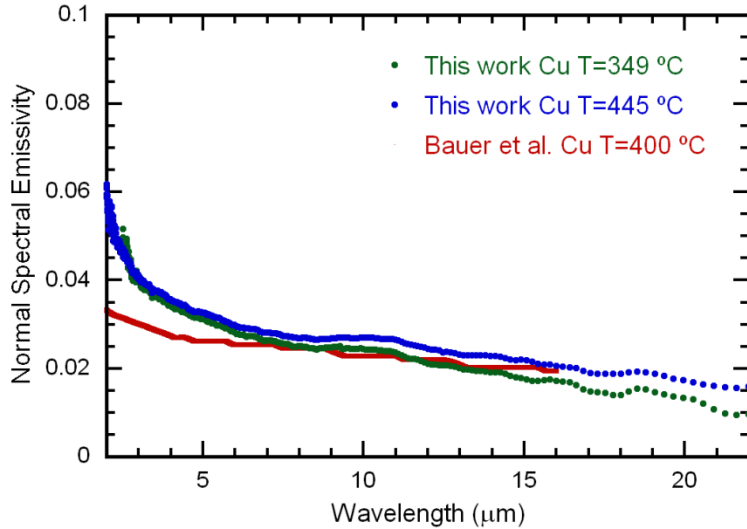


Figure 3.6 Comparison between normal spectral emissivity curves from this work at 349 and 445 °C and from Bauer et al. [40] at 400 °C.

3.4 Silver

For the silver sample, the measurements are performed the same way the copper ones are, with the exception that an argon atmosphere is introduced instead of a reducing one. Three cycles were performed and the emissivity was measured at six temperatures between 300 and 800 °C.

Figure 3.7 shows the normal spectral emissivity curves between 2 and 22 μm from the first and third cycle at two different temperatures. We can see that the emissivity has decreased with the cycling, but this time it seems that the evolution has not been as strong as in copper.

In Figure 3.8 the normal emissivity evolution with the cycling at 5, 10, and 15 μm is plotted at all temperatures. There is little to no evolution at 5 μm, whereas at 10 and 15 μm there is a slight evolution between the first and the second cycle, especially at high temperatures. In any

case, the sample is completely stable by the time the third cycle measurements are done.

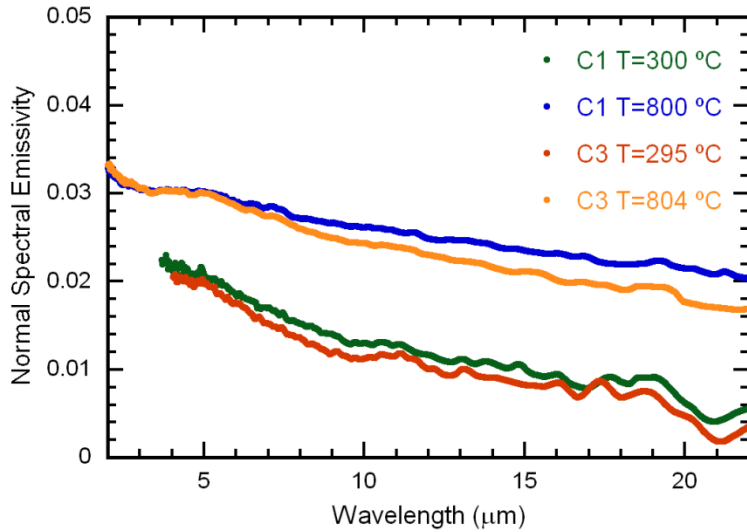


Figure 3.7 Normal spectral emissivity of silver as a function of temperature at two temperatures for two different cycles.

In Figure 3.9 the normal spectral emissivity curves between 2 and 22 μm from the last cycle are plotted. The low emissivity measured in this sample is quite remarkable. In fact, silver is supposed to be the lowest emitting pure metal. This shows how accurate the HAIRL radiometer can be for low emissivities. However, the emissivity at low temperatures such as 295 $^{\circ}\text{C}$ is not easy to obtain at very short and long wavelengths. As a consequence, the obtained emissivity values at 295 $^{\circ}\text{C}$ below 4 μm and at 395 $^{\circ}\text{C}$ below 3.5 μm present too much noise and therefore they are not shown in the graph. We can also see that the emissivity in silver follows a similar behavior to the one presented in copper: the emissivity decreases as the wavelength decreases, while it increases when the temperature rises.

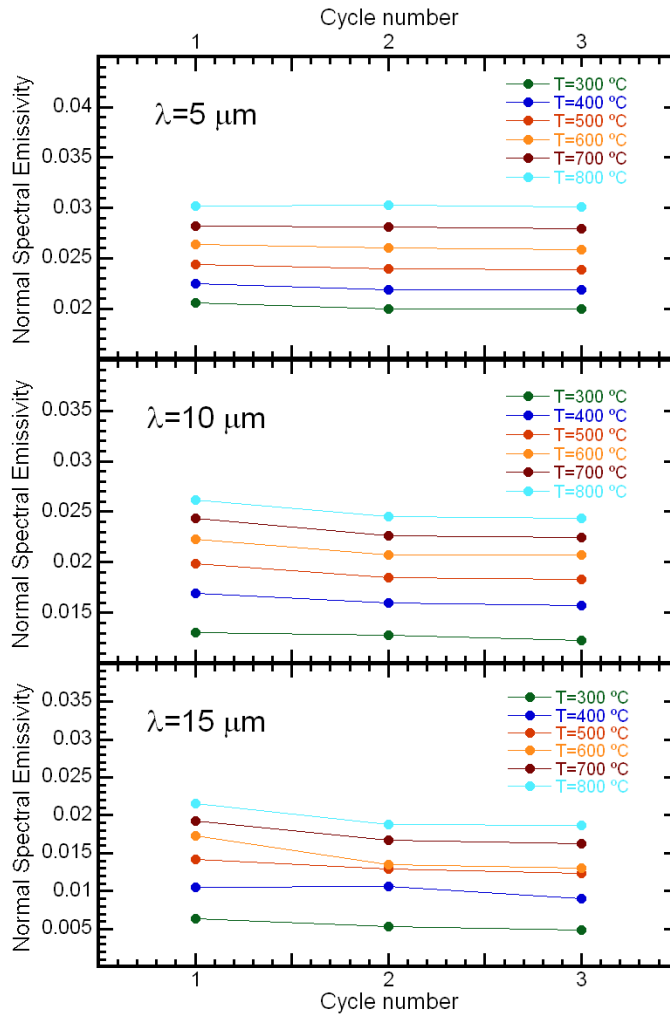


Figure 3.8 Normal emissivity values of silver at 5, 10 and 15 μm for the three cycles at six temperatures.

The temperature evolution can be seen more clearly in Figure 3.10, where the emissivity evolution with temperature is plotted for 5, 10, and 15 μm . Once again, we see a linear evolution of the emissivity at 5 μm , while longer wavelengths (10 and 15 μm) the increase tends to be parabolic.

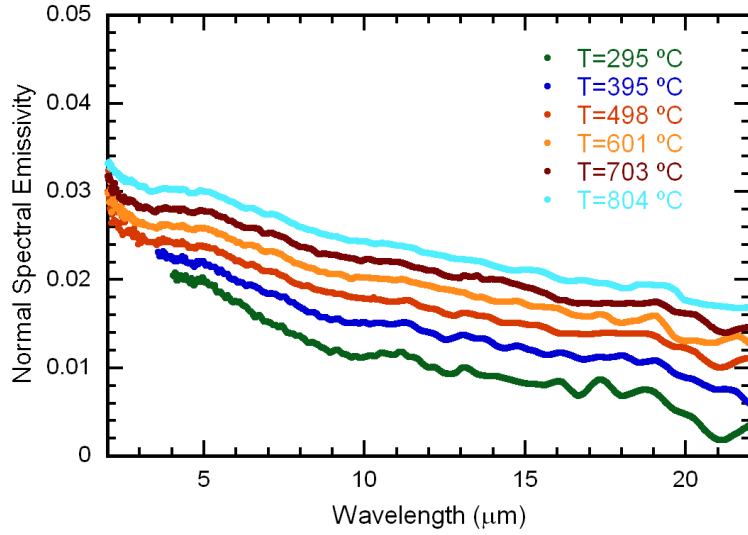


Figure 3.9 Normal spectral emissivity curves of silver from the third cycle at six different temperatures.

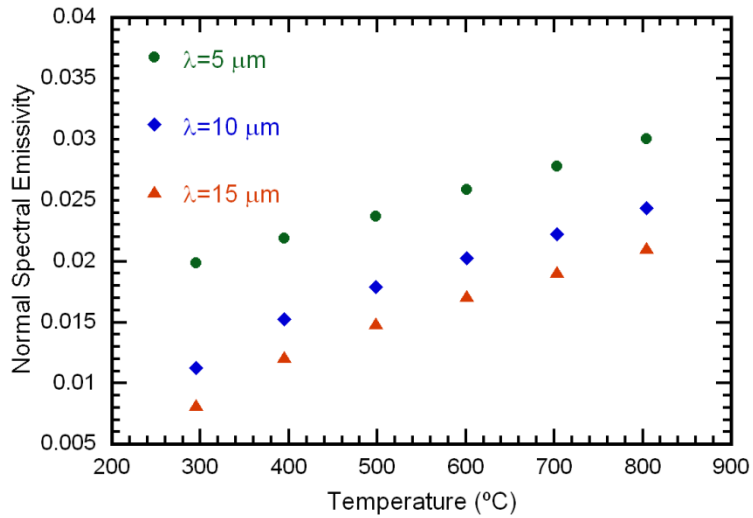


Figure 3.10 Normal spectral emissivity evolution with temperature of silver at 5, 10 and 15 μm on the third cycle.

3.5 Nickel

The nickel measurements are made the same way as the silver ones, where an argon atmosphere is used. Five measurement cycles between 200 and 800 °C with seven measurements in each cycle are made.

Figure 3.11 displays the normal spectral emissivity curves of two temperatures at the first and last cycle between 2 and 22 μm . Once again stress relaxation can be observed, especially at longer wavelengths, where mayor evolution has also been detected in the previous metals of this chapter.

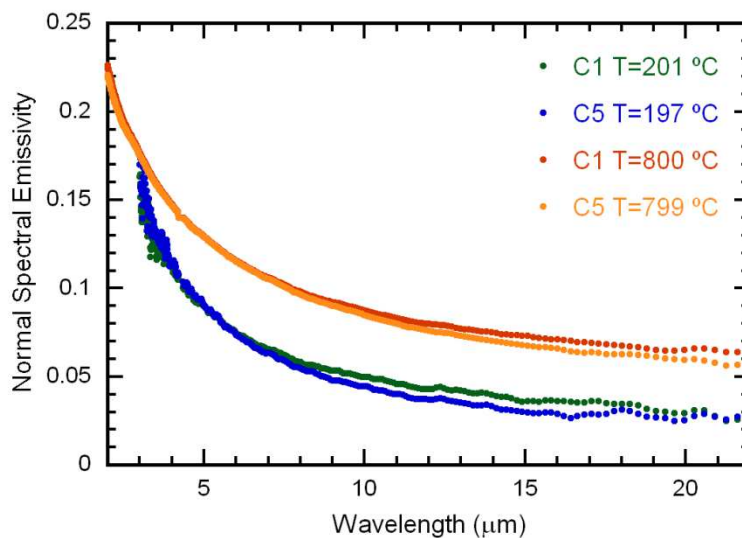


Figure 3.11 Normal spectral emissivity of nickel as a function of wavelength at two temperatures for two different cycles.

Figure 3.12 shows the normal emissivity values at 5, 10 and 15 μm from the first to the fifth cycle at seven different temperatures. At 5 μm there seems to be no appreciable evolution. At 10 and 15 μm though, there seems to be an emissivity increase on the second cycle at low temperatures. This is the main reason why another extra two cycles

are performed compared to the silver. Nevertheless, the emissivity seems to be stable after the third cycle.

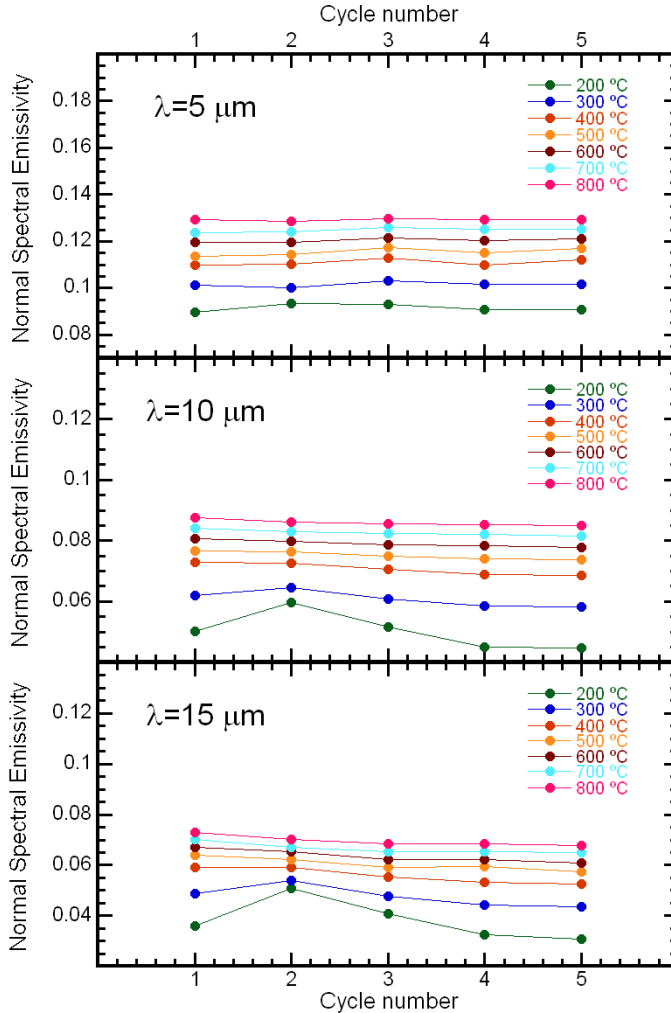


Figure 3.12 Normal emissivity values of nickel at 5, 10 and 15 μm for the five cycles at all temperatures.

Normal spectral emissivity curves between 200 and 800 °C are displayed in Figure 3.13. The curves also show the typical metallic behavior with the emissivity increasing with temperature and decreasing with wavelength. Figure 3.14 shows the evolution with temperature at 5, 10

and 15 μm . Here again, the linear increase at short wavelengths shifts towards a parabolic one at longer ones.

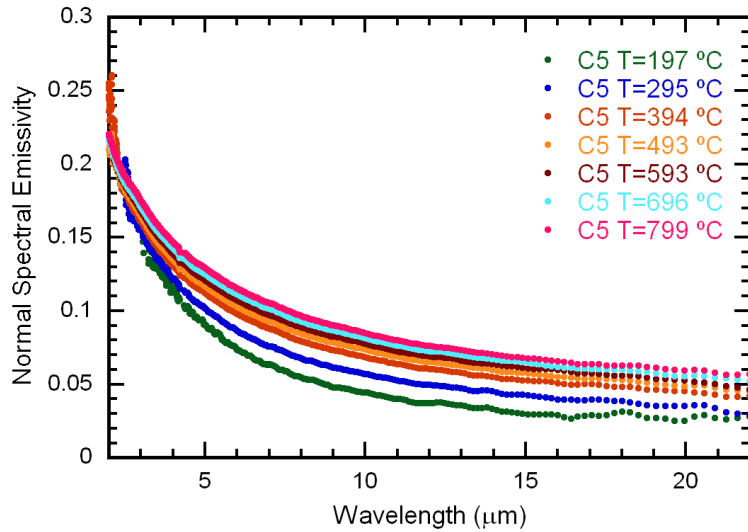


Figure 3.13 Normal spectral emissivity curves of nickel from the fifth cycle at seven different temperatures.

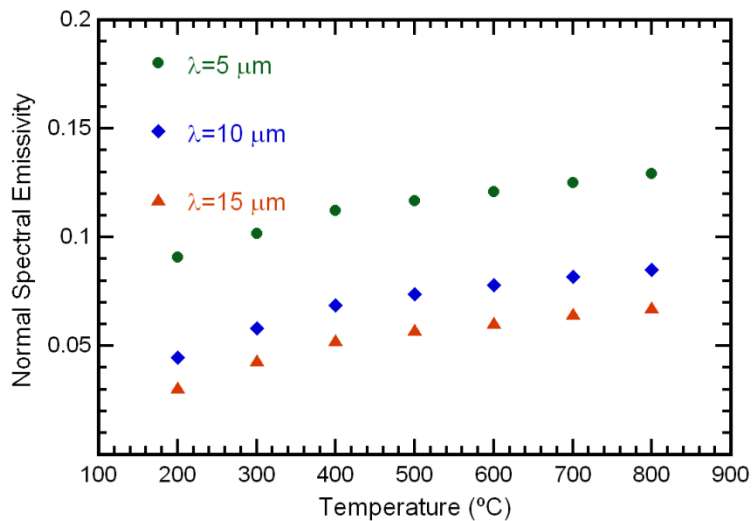


Figure 3.14 Normal spectral emissivity evolution with temperature of nickel at 5, 10 and 15 μm on the fifth cycle.

Finally, the spectral emissivity curves obtained in this work are compared to the ones obtained in previous studies. Curves at 394 and 799 °C from the last cycle are compared to the curves obtained by Bauer et al. at 400 °C [40] and Teodorescu et al. at 1167 °C [46] respectively in Figure 3.15. Bauer's curve and ours at 394 °C have quite a similar behavior up to 5 μm , while at longer wavelengths this work's measurements present a lower value than his. In the case of the curve at 1167 °C, it is compared to our highest measured temperature at 799 °C. At longer wavelengths even if the absolute values differ the behavior is quite similar. At shorter wavelengths the emissivity at 1167 °C rapidly increases. This is probably due to the presence of surface oxidation, since it is known that in the early stages of oxidation the emissivity increases at short wavelengths [18,55]. However, the lack of information about the samples used in both works does not allow making any definite observations when comparing the results.

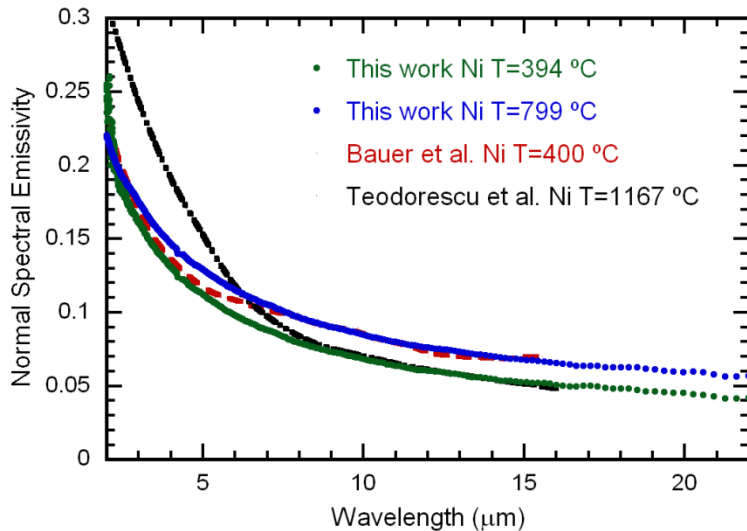


Figure 3.15 Comparison between normal spectral emissivity curves from this work at 394 and 799 °C and from Bauer et al. at 400 °C [40] and Teodorescu et al. at 1167 °C [46] respectively.

3.6 Magnesium

The magnesium sample is also measured under an argon atmosphere inserted after vacuum has been made inside the sample chamber. Magnesium is quite a tricky metal to measure since it rapidly oxidizes at room temperature and therefore it has to be polished right before putting it inside the sample chamber. Besides, measurements were only made between 300 and 450 °C, because it has a spontaneous combustion temperature of 472 °C. Even if there should be almost no oxygen left in the chamber, in case anything happens it has been decided not to heat the magnesium over its critical temperature. A total of five cycles were made and measurements were made every 50 °C approximately.

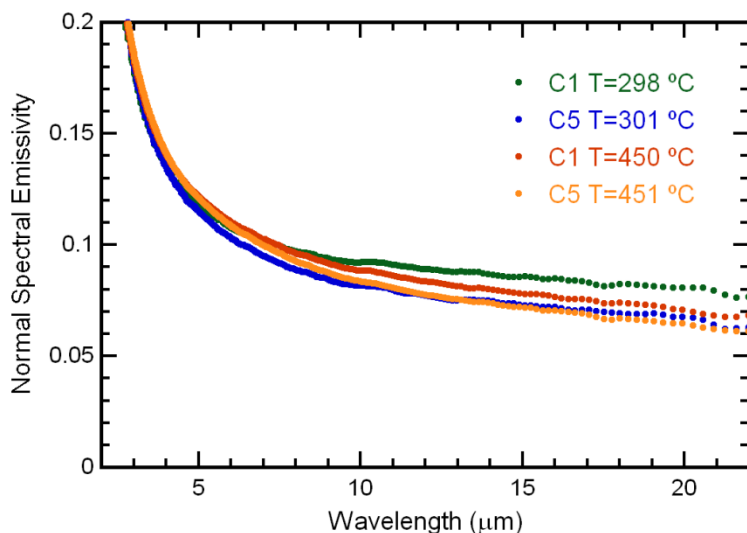


Figure 3.16 Normal spectral emissivity of magnesium as a function of wavelength at two temperatures for two different cycles.

Figure 3.16 shows the normal spectral emissivity curves at two temperatures from the first and last cycle between 2 and 22 μm. The magnesium sample clearly also suffers the stress relaxation. Figure 3.17

shows how the relaxation occurs at 5, 10 and 15 μm during the five cycles. At short wavelengths the emissivity does not evolve due to these relaxations, but as it happened in previous metallic samples this phenomenon can be detected at longer wavelengths such as 10 and 15 μm . Here the emissivity clearly evolves up to the fourth cycle and then stabilizes. The reason why it has taken longer to stabilize compared to the previous metallic samples is probably related to the fact that the sample is only heated up to 450 $^{\circ}\text{C}$ instead of 800 $^{\circ}\text{C}$.

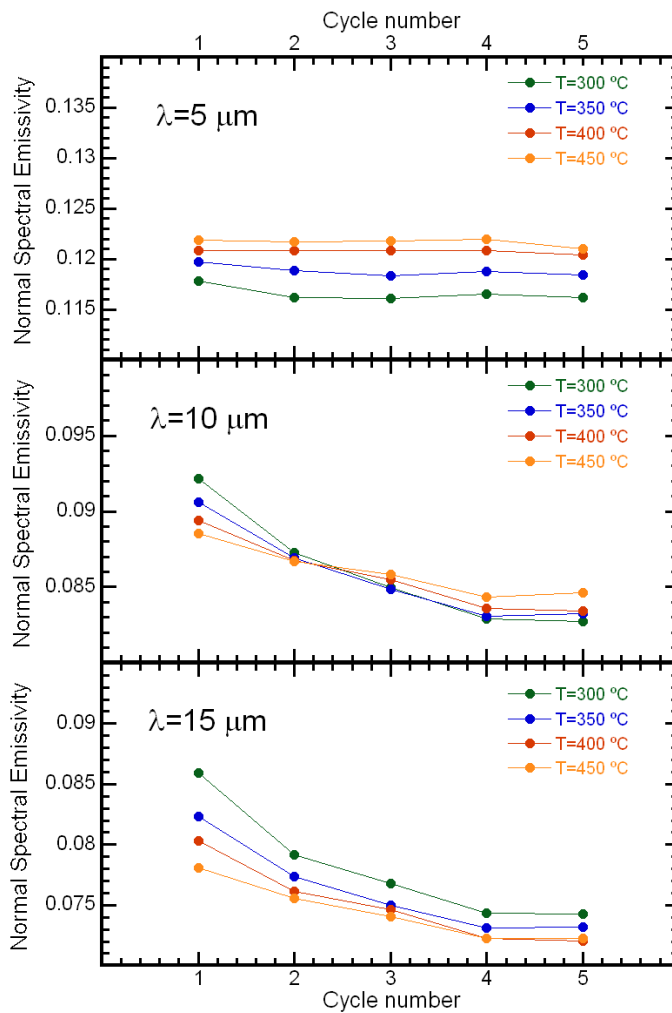


Figure 3.17 Normal emissivity values of magnesium at 5, 10 and 15 μm for the five cycles at all temperatures.

The normal spectral emissivity curves at the four different temperatures from the last cycle are displayed in Figure 3.18. Here a slightly different behavior from the previous metals is observed. Even if at shorter wavelengths the emissivity slightly increases with temperature, from around 11 μm onwards the emissivity becomes almost constant with temperature.

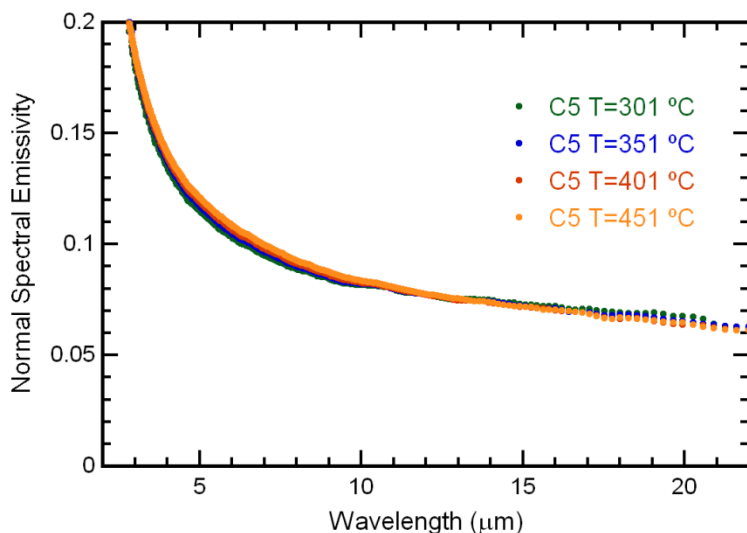


Figure 3.18 Normal spectral emissivity curves of magnesium from the fifth cycle at four different temperatures.

What is more, this can be clearly observed in Figure 3.19, where the temperature dependence between 300 and 450 $^{\circ}\text{C}$ is observed once again at 5, 10 and 15 μm . At 5 μm , a slight increase is observed whereas at 10 and 15 μm the emissivity stays almost constant with temperature.

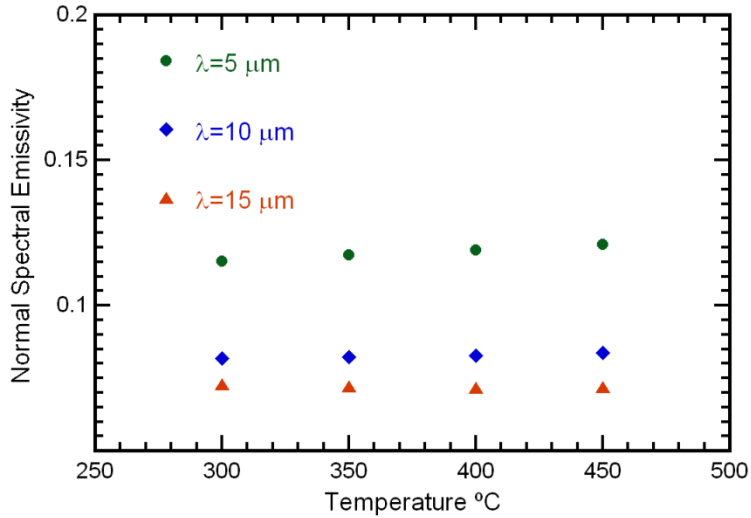


Figure 3.19 Normal spectral emissivity evolution with temperature of magnesium at 5, 10 and 15 μm on the fifth cycle.

3.7 Hagen-Rubens equation

The wave solutions to Maxwell's equations provide means for determining the complex refractive index from the electric and magnetic properties of the materials [19]. For metals where the resistivity is small and for m , the ϵ' and ϵ'' equations can be reduced to the Hagen-Rubens equation [56]:

$$\epsilon'' = \frac{2}{\pi} \frac{\rho}{\lambda^2} \quad (3.10)$$

where λ is the wavelength in microns and ρ is the electrical resistivity in ohm cm. Even if the $\epsilon'' \approx \frac{2}{\pi} \frac{\rho}{\lambda^2}$ approximation is not a very precise one, some useful results can be obtained for certain metals.

Once ϵ' and ϵ'' are known an equation for the normal spectral emissivity can be obtained:

Now we can fit the previously obtained emissivity curves to this equation and compare the electrical resistivity values obtained to the ones found in the literature [57-60]. Figure 3.20 displays the resistivity values obtained from fitting the spectral emissivity curves at different temperatures from the four pure metals (dots) and the electrical resistivity values obtained from the literature (lines). The Hagen-Rubens Equation fits well only with copper. In nickel and silver, despite showing the same behavior, the absolute values of the resistivity are way apart one from each other. Finally, it fits the worst with the magnesium, since not even the same tendency is observed between both sets of data.

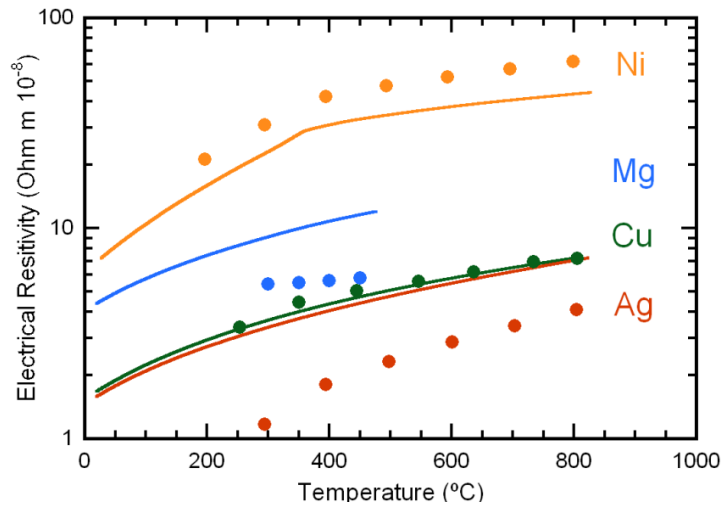


Figure 3.20 Comparison between the electrical resistivity data from the literature (lines) and the values from the Hagen-Rubens fitting (dots).

3.8 Total normal emissivity

The last section from this chapter is dedicated to the total normal emissivity. The total normal emissivity is calculated from the spectral emissivity curves obtained the way it is explained back in Chapter 2. Figure 3.21 shows the total normal emissivity values obtained for copper, silver, nickel and magnesium. In all cases the total normal emissivity increases linearly with temperature. This increase is not only due to increase of the spectral emissivity with temperature, but also because of the shift of the maximum of the Planck function towards shorter wavelengths as temperature increases (Wien's displacement law). Since the emissivity of metals at shorter wavelengths is higher than at larger ones the total normal emissivity will increase even for magnesium, where there is little to no evolution of the normal spectral emissivity curve with temperature. Here we can also see how little the two lowest emitting metals, copper and silver, emit. The four sets of data are fitted to a linear function.

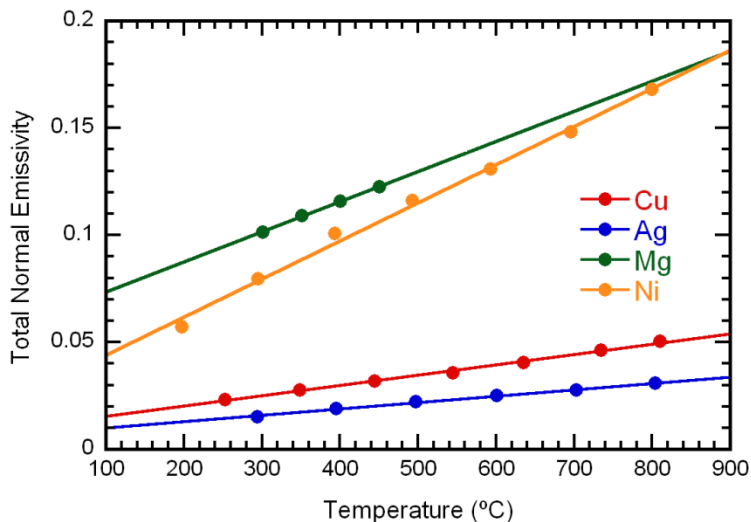


Figure 3.21 Total normal emissivity data from copper, silver, nickel and magnesium. The four sets of data are fitted to a linear function.

3.9 Conclusions

The normal spectral emissivities of four pure metals (Cu, Ag, Ni and Mg) are studied in this chapter. Three different aspects are studied in each one of them: the surface stress relaxation and its effect on the evolution in the emissivity with the cycling; the spectral dependence, where the emissivity in metals decreases as the wavelength increases; and the temperature dependence, where the emissivity increases with temperature. The lack of temperature-dependent measurements makes this work especially valuable. However, emissivity curves of copper and nickel are compared to those ones found in the bibliography. Besides, the Hagen-Rubens equation is used to obtain electrical resistivity values. The results show that only the copper values fit correctly with the previously measured resistivity found in the bibliography. Finally, the spectral emissivity curves are integrated along the spectrum in order to obtain the total normal emissivity values. All four metals have a linear increase with temperature.

4 Optical properties of metals: the anomalous skin effect

En metales con una conductividad eléctrica muy alta, el recorrido libre medio de los electrones de conducción puede ser del orden de la profundidad de penetración del campo eléctrico. En estos casos la aproximación de Drude de campo constante deja de ser válida y surge el efecto skin anómalo. Cuando se resuelven las ecuaciones de transporte con una fuerza debida al campo eléctrico que depende del tiempo, se observa que en el caso de reflexión especular aparece un mínimo en la reflectividad el cual hasta ahora no se ha detectado experimentalmente. Solo existen indicios de su existencia. En este capítulo se hace un análisis teórico del efecto skin anómalo para los doce metales puros con mayor conductividad eléctrica. En el caso del cobre el análisis es más detallado con el fin de obtener el comportamiento de la emisividad con la temperatura y el ángulo de emisión. En la parte experimental se observa que las medidas experimentales de la emisividad espectral del cobre a 250 °C, muestran un máximo del mismo orden y en la misma región que aquél predicho por la teoría del efecto skin anómalo. Este resultado es una evidencia de la presencia de este fenómeno incluso a altas temperaturas donde el efecto es más débil.

4 Optical properties of metals: the anomalous skin effect

4.1 Introduction

The theoretical and experimental study of the optical and electrical properties of metals has drawn a lot of attention since the first years of the 20th century. In fact, at the beginning of this century, the classical theory (Drude) that allowed describing the conducting electrons behavior under the influence of an electric field applied to a metal surface had already been completely developed.

Nevertheless, in 1947, A.B. Pippard indicated that the Drude behavior would be valid only if the electron mean free path l were too small in comparison to the field penetration depth δ [61,62]. When l and δ are of the same magnitude, the static field approximation is no longer valid and the spatial dependence needs to be taken into account. This means that when introducing this dependence on the Boltzmann equation the distribution function will depend on \vec{k} and therefore the equation will become much more complex. As a consequence it can be demonstrated that for a good electrical conducting metal, reflectivity must show a wide minimum in the infrared area.

Until now, experimental evidence that confirms this event has not been found. This is due to the fact that accurate measurements of optical constants in metals in the infrared area are not found or at least are limited in frequency and temperature. In this work, the anomalous skin effect will be analyzed by studying the emissivity, related to the reflectivity by the equation $\varepsilon = 1 - \mathcal{R}$. On one hand, the emissivity maxima for different metals will be studied by using the anomalous skin effect theory. On the other, copper emissivity values will be obtained experi-

mentally and then compared to the previously obtained results using the anomalous skin theory. Previously (in section 4.2), metals that are potential candidates to present the anomalous skin effect are studied and their emissivity curves predicted by the theory are obtained.

4.2 Background

Starting from Pippard's suggestion in 1947 [61,62], Reuter and Sondheimer developed a theory for the anomalous penetration effect for the first time by using the semiclassical theory [63]. Later works would help incorporating this theory to the general theory of optical properties of metals [64-69]. It has also been proved that the quantum treatment of the problem presents the same results as the semiclassical one [70]. The formulae coming up next are mainly based in Reuter and Sondheimer's work [63] whereas the approximations come from Dingle's articles [66-68]. Calculations related to the anomalous skin effect appear in detail in Appendix I.

In most metal optical applications (e.g. metal mirrors), it is necessary to know the response of the electrons to the incident electromagnetic field. Depending on the frequency this response is related to the intraband transitions of the conduction electrons, the interband transitions due to internal photoelectric effect or both of them. Other absorption mechanisms, such as lattice absorption and localized states, should only be considered in specific frequency ranges. For a large portion of the infrared spectrum, the interband transitions are forbidden for the metals analyzed in this paper. In this spectral region, the absorption mechanism is associated to intraband transitions. Assuming that other possible absorption effects such as electron-electron or multiple phonon processes are negligible, the interaction is described by means of the relation between the current density and the electrical field of the metal. This relationship requires solving the relaxation time

approximation Boltzmann equation for the non-equilibrium part of the electron distribution function. This equation contains a diffusion term that can be omitted when the electric field inside the metal can be considered spatially constant. This assumption is valid when the quotient between the electron mean free path l and the penetration depth of the electromagnetic field $\delta(\omega)$ fulfills the following condition:

$$\frac{l}{\delta} \ll (1 + \omega^2 \tau^2)^{\frac{3}{4}}. \quad (4.1)$$

The penetration depth of the electromagnetic field for optical frequencies given by

$$\delta(\omega) = \text{Re} \left[\frac{c(1 + i\omega\tau)^{\frac{1}{2}}}{(2\pi\sigma_0\omega)^{\frac{1}{2}}(1 + i)} \right], \quad (4.2)$$

where σ_0 is the dc conductivity and τ is the relaxation time. In many papers the penetration depth is obtained using a simplified formula $\delta_0^2 = 2c^2/\omega_p\omega\tau$ where $\omega_p^2 = 4n_e e^2\pi/m^*$ is the plasmon frequency of conduction electrons. Other physical parameters used in the theoretical calculus are

$$n_e = \frac{8\pi}{3} \left(\frac{mv_F}{h} \right)^3, \quad \sigma = \frac{n_e e^2 l}{mv_F}, \quad l = v_F \tau, \quad \alpha = \frac{3}{2} \left(\frac{l}{\delta} \right)^2$$

$$\beta = \frac{\alpha}{\omega\tau}, \quad \xi = \frac{i\alpha}{(1 + i\omega\tau)^3} \quad m \approx m^*, \quad (4.3)$$

where n_e is the electron density, v_F is the Fermi velocity, m^* is the electron effective mass, ξ is a parameter that takes into account the relative sizes of the energy loss mechanisms and α and β are coeffi-

cients used in the theory. If Equation 4.1 is satisfied, the interaction between the electromagnetic field and the metal is called normal skin effect. At low and high infrared frequencies ($\omega\tau \ll 1$ and $\gg 1$), the inequality will hold regardless of the value of τ and σ_0 and the experimental results must be in reasonably good agreement with the classical Drude theory [71]. The impedance Z can be obtained using the classical equation:

$$Z_{clas} = \frac{4\pi\omega l}{c^2} \sqrt{\frac{\omega^2 l^2}{c^2} - \frac{4i}{3} \frac{\alpha}{1 + i\omega\tau}}, \quad (4.4)$$

where the emissivity is obtained by

$$\varepsilon = \frac{c}{\pi} \text{Re}[Z]. \quad (4.5)$$

The impedance is related then to the refractive index n and extinction coefficient k through the following formula:

$$\tilde{n} = \frac{4\pi}{c} \frac{1}{Z}, \quad \tilde{n} = n - ik. \quad (4.6)$$

At mid and far-infrared frequencies, Eq. 4.1 may not be satisfied even above room temperature. It is a wide region, with $l \approx \delta$, where the Drude classical theory is not valid, that we will call the anomalous skin effect spectral region. In this case, the dependence of the optical properties with the conduction electrons must take into account the non-local character of the relationship between the field and current density which forces to retain the diffusion term in the Boltzmann equation. Since the first paper about the phenomenological approach of the anomalous skin effect [63], a major effort to complete the theory has

been done. The theoretical approaches [63,66] express the metal optical properties in terms of the surface impedance $Z = R + iX$ (where R is the surface resistance and X is the surface reactance). From the surface impedance, the reflectance and the emissivity as a function of the relaxation time and optical conductivity can be obtained.

In most of the papers, the experimental results are compared with two sorts of semiclassical equations for the theoretical surface impedance: those that take the form of definite integrals solved numerically [63-65] and those where the surface impedance is obtained from series expansions [66-68,72]. Even though we will make use of integral equations a comparison with theoretical predictions of series expansions will be displayed. The full calculations of the definite integrals are shown in Appendix I.

Furthermore, the model assumes that a fraction p ($0 \leq p \leq 1$) of the electrons arriving at the surface are scattered specularly, while the rest are scattered diffusely [73]. The value of this parameter, which is known *a priori*, is between $p = 1$ assuming complete specularity and $p = 0$ assuming complete diffusiveness. From an experimental point of view, this parameter is related to the surface roughness and has been extensively discussed in the literature [74-81]. Using the de Broglie wavelength of electrons as well as the roughness value is possible to find when the surface loses its specular character and therefore when to use theoretical formulas with $p = 0$ instead of $p = 1$. However, in a great number of papers about metals, semimetals and semiconductor $p = 0$ is obtained for both specular and diffuse surfaces [64,65,72-81]. This means that the surface roughness value for which is assigned complete diffusiveness cannot be the same as the obtained one from the diffraction theory. Furthermore, it is easy to see that even with the interpretation of the indicated parameter p , its value expressed in terms of probabilities of scattering is different from that of the kinetic

probability of specular reflection [81]. This analysis shows that $p = 1$ for a metal does not necessarily imply that a metal surface is smooth compared with the de Broglie wavelength [74]. This conclusion, which has an experimental demonstration in this work, indicates that many interpretations have assumed $p = 0$ for a value that is related to $p = 1$ or an intermediate value.

In any case, considering the following experimental results, we will consider the equations for $p = 1$. For the optical region, when using definite integrals the emissivity is given by [63]:

$$\varepsilon(\omega) = \varepsilon_{clas} \sqrt{\frac{2\alpha}{3}} \frac{\omega\tau \text{Re}[I] - \text{Im}[I]}{1 + \omega^2\tau^2\sqrt{-\omega\tau + \sqrt{1 + \omega^2\tau^2}}}, \quad (4.7)$$

where I is a definite integral

$$I = \int_0^\infty \frac{dz}{z^2 + \xi k(z)}, \quad (4.8)$$

where $k(z)$ is a function of z (perpendicular to the metal surface):

$$k(z) = \frac{2}{z} [(1 + z^2) \arctan z - z]. \quad (4.9)$$

On the other hand, the series expansion proposed by Dingle [66] for the optical region is

$$-i \frac{(1 + i\omega\tau)c^2}{4\pi\omega\tau\nu_F} Z = 0.7698(\pi\xi)^{-\frac{1}{3}} + 0.6534(\pi\xi)^{-\frac{2}{3}} + \dots, \quad (4.10)$$

and for the near and mid-infrared region it can also be used

$$-i \frac{(1 + i\omega\tau)c^2}{4\pi\omega\tau v_F} Z = \frac{\sqrt{3}}{2} \xi^{-\frac{1}{2}} + \frac{\sqrt{3}}{15} \xi^{\frac{1}{2}} - \frac{1}{6} \xi + \dots \quad (4.11)$$

For $p = 0$ a definite integral is yet to be obtained. However, Dingle developed a series expansion that can be used

$$-i \frac{(1 + i\omega\tau)c^2}{4\pi\omega\tau v_F} Z = \frac{\sqrt{3}}{2} \xi^{-\frac{1}{2}} + \frac{3}{16} - \frac{83\sqrt{3}}{1920} \xi + \left(\frac{4 \ln 2}{105} + \frac{8723}{322560} \right). \quad (4.12)$$

4.3 Numerical calculations

4.3.1 Numerical integrations and series expansions

Figure 4.1 shows the normal spectral emissivity for the classical theory (Eq. 4.4 and 4.5) and for the anomalous skin effect with $p = 1$ (Eq. 4.7) in copper at three different temperatures (80, 293 and 526 K). It must be noticed that the anomalous skin effect shows, for $p = 1$, a broad peak in the mid and far-infrared region. In the same figure, the two series approximations for $p = 1$ (Eqs. 4.10 & 4.11) and the one for $p = 0$ (Eq. 4.12) are plotted. The three plots confirm the range of validity of the two series for $p = 1$. Thus, Eq. 4.10 is a better approximation for higher temperatures, while Eq. 4.11 works better for lower ones. Two facts should be outlined: on the one hand, the strong dependence of the anomalous skin effect with temperature; on the other, it is better to use the integral equation because the series expansion approach only covers a fraction of the anomalous wavelength range.

Before calculating the definite integrals or the series expansions for specific materials, a selection a metal candidates is made to see which ones present a stronger anomalous behavior. Table 4.1 shows the physical properties related to the anomalous skin effect of twelve metals at room temperature considering that $p = 1$.

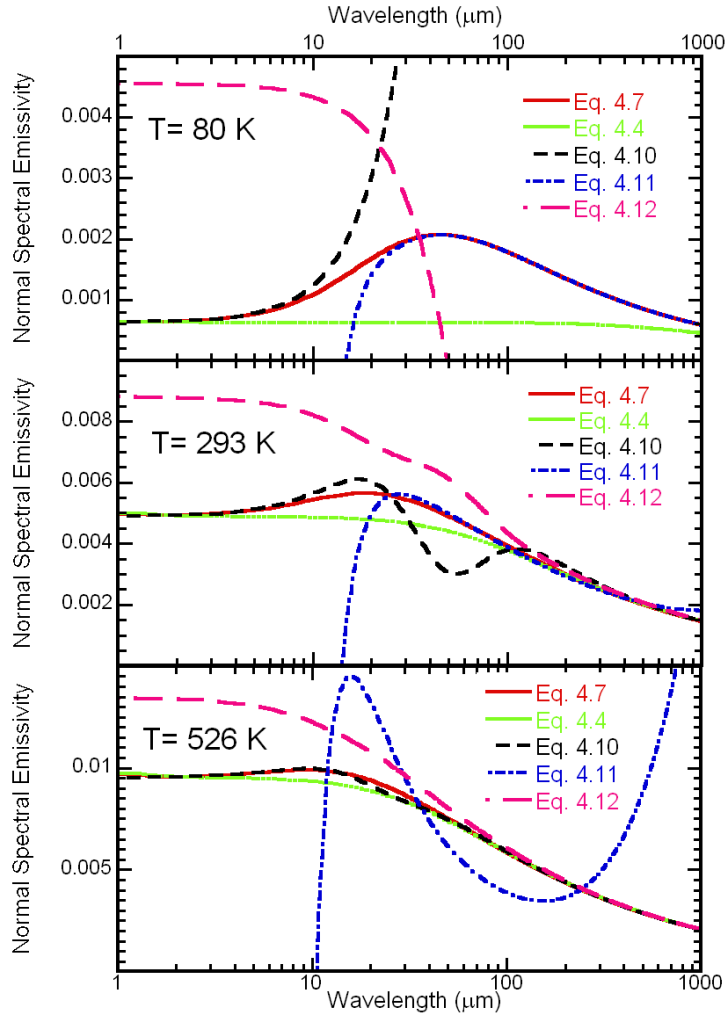


Figure 4.1. Classical emissivity given by Eq. 4.4 (dotted, green), anomalous skin effect emissivity with by Eq. 4.7 (solid, red), Eq. 4.10 (dashed, black), Eq. 4.11 (dotted-dashed, blue) and series expansion for by Eq. 4.12 (long-dashed, pink). a) 80 K, b) 293 K and c) 526 K. The physical parameters used are those for copper from Table 4.1.

The first physical properties represented in Table I are the relaxation time τ , the carrier density n , the plasmon frequency ω_p , the dc conductivity σ_{dc} , the dc resistivity ρ_{dc} , the mean free path ℓ and the Fermi velocity v_F . All these parameters are used one way or the other on the

Reuter and Sondheimer [63] and Dingle [66] formulas. The second set of parameters show the strength of the anomalous skin effect. Literature bulk metal experimental data (n_e , τ , σ , v_F and l) were used to obtain the other physical parameters in Table 4.1 [59,71]. The order in which the metals are listed in Table 4.1 is based on the value of the strength of the anomalous behavior for each metal (β and ξ).

Table 4.1 Physical parameters of the metals that according to Eq. 4.1 must present an anomalous skin effect spectral region at room temperature, τ is the relaxation time, n_e is the carrier density, ω_p is the Plasmon frequency, σ is the dc conductivity, ρ is the dc resistivity, l is the mean free path, and v_F is the Fermi velocity. The rest of parameters show the strength of the anomalous skin effect on the optical properties and those with an asterisk are calculated for $\lambda = \lambda_{max}$.

T_{work}	Ag	Cu	Au	Ca	Al	Rh	Mg	Mo	Ir	W	Zn	Ru
τ (fs)	38.2	25.0	27.1	22.9	7.2	10.9	9.4	10.6	4.8	5.1	4.5	6.4
n (10^{22}cm^{-3})	5.86	8.47	5.90	4.61	18.07	7.26	8.61	6.41	14.12	12.64	13.14	7.27
$\omega_{plasmon}$ (10^{15}Rad/s)	1.37	1.64	1.37	1.21	2.40	1.57	1.66	1.43	2.12	2.01	2.05	1.52
σ (10^{17}esu)	5.67	5.36	4.05	2.67	3.30	2.00	2.05	1.71	1.70	1.64	1.50	1.18
ρ ($10^{-8} \Omega \text{m}$)	1.59	1.68	2.21	3.36	2.82	4.49	4.66	5.23	5.29	5.49	5.95	7.60
l (10^{-6}cm)	5.31	3.93	3.78	2.94	1.46	1.62	1.49	1.52	0.90	0.92	0.82	0.96
V_F (10^5cm/s)	1.39	1.57	1.39	1.28	2.03	1.49	1.58	1.43	1.87	1.80	1.82	1.50
β	4.39	3.47	2.24	1.06	1.02	0.51	0.51	0.39	0.30	0.28	0.23	0.18
λ_{max} (μm)	31.3	21.5	25.5	24.3	7.7	12.6	11.0	12.7	5.8	6.3	5.6	8.2
$\epsilon_{ase}/\epsilon_{cl} \text{ max}$ (%)	21.6	18.3	13.2	7.5	7.2	4.1	4.1	3.3	2.6	2.5	2.1	1.7
$\omega\tau$ *	2.30	2.19	2.00	1.77	1.76	1.63	1.61	1.57	1.55	1.53	1.51	1.48
δ_{clas} (10^{-6}cm) *	2.05	1.75	2.19	2.62	1.33	2.19	2.01	2.37	1.61	1.71	1.69	2.29
γ *	0.83	0.73	0.56	0.34	0.33	0.19	0.20	0.16	0.12	0.12	0.10	0.08
ξ *	0.64	0.55	0.40	0.22	0.22	0.12	0.12	0.10	0.07	0.07	0.06	0.05
λ_{peak} (μm)	27.3	18.3	20.5	17.2	5.4	7.1	6.2	6.3				
ϵ_{max}	0.0046	0.0057	0.0060	0.0076	0.0121	0.0123	0.0130	0.0134				

A few conclusions can be made while looking the table. The better electrical conductor a metal is, the stronger anomalous skin effect is going to have. Silver, copper and gold, being elements of the same column in the periodic table (with a $d^{10} s^1$ electronic configuration), are the best conductors and the ones that present the strongest behavior. Besides, the electrical field penetration depth δ where anomalous skin

effect is larger does not have a particular tendency related to the effect. However, the mean free path l has a linear dependence with dc electrical conductivity and therefore is larger for those metals that present a stronger anomalous skin effect. When looking at the l/δ coefficient it can be seen that while silver and copper present values over 2, materials such as ruthenium and zinc have a mean free path of less than half of the field penetration depth. This is in agreement with the ideas that A. B. Pippard pointed out back in 1947 [61,62].

When looking at the wavelength values where effect is stronger (λ_{max}) compared to the Drude classical theory ($(\mathcal{E}/\varepsilon_{clas})_{max}$) one can see that they do not match with wavelength values where peak is situated at (λ_{peak}). While the anomalous contribution has the form of a wide peak, the classical contribution in metals does in fact decrease monotonously while wavelength increases. In those metals with very little contribution (in all cases under 3% of the classical contribution) such as iridium, tungsten, zinc and ruthenium the effect will be so little that even with $p = 1$ a peak will not be formed. Last, it should be noted that the predicted emissivity values at λ_{peak} (ε_{max}) for metals under ideal conditions (no roughness, no oxidation,...) are really small which shows us how difficult it can be detecting this maxima.

With Equations 4.4 and 4.7 and the parameters from Table 4.1 allow us to obtain the theoretical predictions of the classical and the anomalous skin effect emissivities for different metals. Figure 4.2a shows the emissivities of five different metals at room temperature are shown for comparison. In the anomalous skin effect region, the emissivity of the five metals shows a broad peak in the mid-infrared at room temperature. As we can see in Figure 4.2b and 4.2c and in Table 4.1, the highest values for $(\mathcal{E}/\varepsilon_{clas})_{max}$, λ_{max} and λ_{peak} correspond to silver. In fact, the lower the emissivity is, the better electrical conductor is the metal and therefore the stronger the anomalous skin effect compared to the

Drude contribution is going to be. However, when looking at the absolute anomalous contribution at room temperature in Figure 4.2c, copper is the metal that stands out the most since even if it has a smaller relative contribution, its higher emissivity compared to silver makes up for the difference.

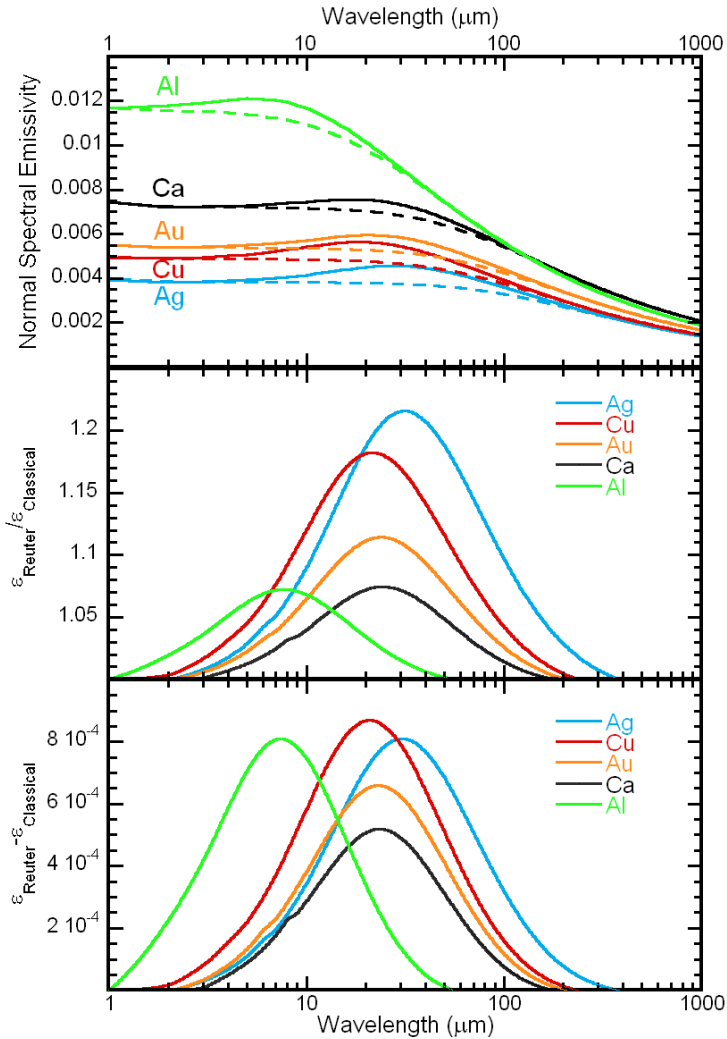


Figure 4.2. a) Predicted classical (Eq. 4.4) and anomalous skin effect emissivities (Eq. 4.7), b) fraction between both anomalous and classical curves and c) anomalous contribution to the emissivity of five metals at room temperature.

4.3.2 Temperature dependence

At low temperature, the emissivity broad peak is shifted towards larger wavelengths, $(\varepsilon/\varepsilon_{clas})_{max}$ grows and the anomalous skin effect spectral range is larger, while at higher temperatures. λ_{peak} is shifted to shorter wavelengths and the relative value of $(\varepsilon/\varepsilon_{clas})_{max}$ as well as the anomalous skin effect range diminishes.

This theoretical prediction is particularized for copper in Figure 4.3. In Figure 4.3a both classical and anomalous curves are plotted at three different temperatures (80, 293 and 526 K). The emissivity increases with temperature, as it is usual in metals. Figure 4.3b shows the value of $(\varepsilon/\varepsilon_{clas})$ at those temperatures. The relative emissivity $(\varepsilon/\varepsilon_{clas})_{max}$ changes from 330% at 80 K to 7% at 526 K in the anomalous skin effect spectral range changes, from $\Delta\lambda \approx 1000 \mu\text{m}$ for 80 K to $\Delta\lambda \approx 50 \mu\text{m}$ for 526 K. Figure 4.3c shows again the anomalous contribution by using the $\varepsilon - \varepsilon_{clas}$ calculation. Here we can see that not only that the proportional contribution of the anomalous skin effect diminishes with temperature, but also its absolute one. In contraposition to the Figure 4.2c curves, in Figure 4.3c the electron density is constant (same metal) and therefore the decrease of the conductivity values will also result on the decrease of the absolute anomalous contribution. In any case, it must be remembered that the emissivity calculated from Equations 4.1 and 4.4 is very sensitive to the relaxation time values, or equally, to the conductivity data. Small changes in the value of these experimental parameters may lead to noticeable differences on λ_{peak} and λ_{max} .

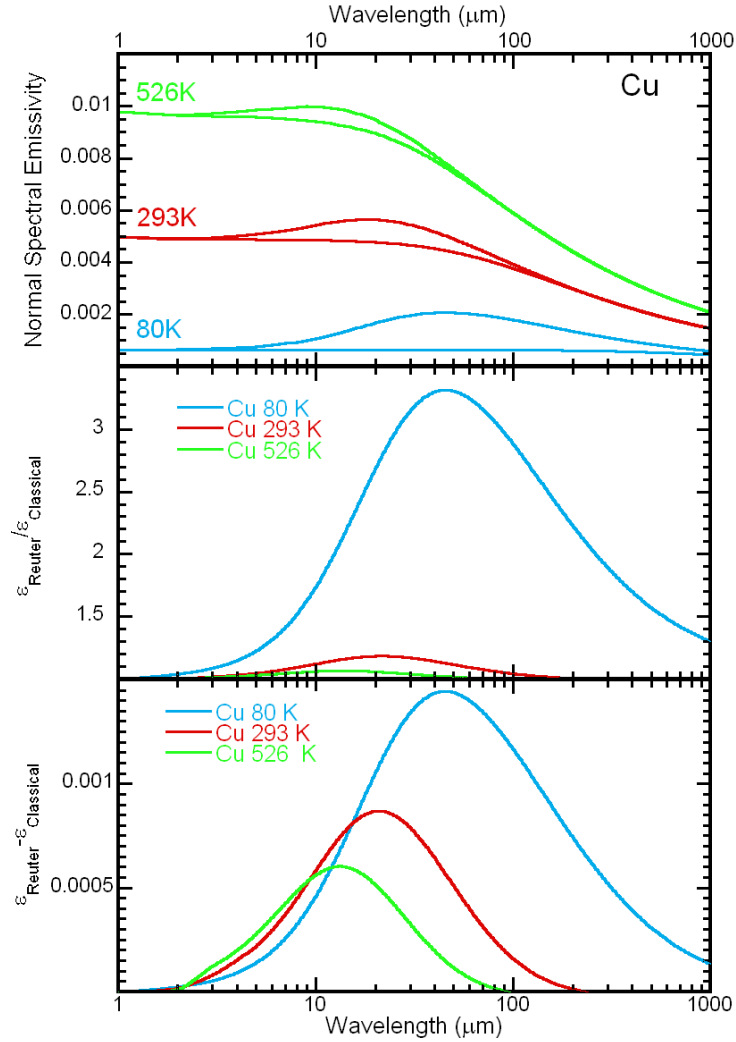


Figure 4.3. a) Predicted classical (Eq. 4.4) and anomalous skin effect emissivities (Eq. 4.7), b) fraction between both anomalous and classical curves and c) anomalous contribution to the emissivity of copper at 80 (blue), 293 (red) and 526 K (green).

4.3.3 Angular dependence

Another aspect to take into account is the angular dependence of the emissivity and the effect that the anomalous skin effect has on it. >If the complex refractive index is obtained through Equation 4.6, the di-

rectional spectral emissivities can be obtained using the classical electromagnetic theory [19]:

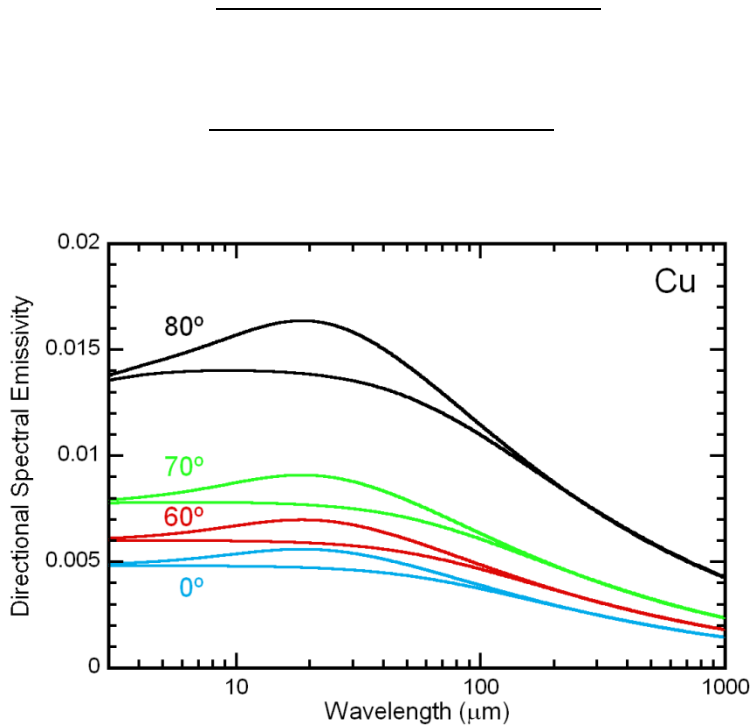


Figure 4.4. Classical and anomalous directional spectral emissivity curves obtained with Equation 4.13 for copper at room temperature for four different emission angles. It can be observed that the $\epsilon_{\text{classical}}$ does not vary.

Figure 4.4 plots the classical and anomalous spectral emissivity curves at 0, 60, 70 and 80 ° between 3 and 120 μm for copper at room temperature. The emissivity increases with the emission angle, but the curve shapes in both classical and anomalous skin effect functions do not change. In fact, as we can see in Figure 4.5, the anomalous curve shows a *lambertian* behavior with the emission angle, which is the behavior predicted on the classical theory [19]. This can be essential on the experimental measurements for two reasons. First, higher emissivi-

ty values will allow detecting more easily possible anomalous peaks; second, looking at the emissivity at various angles we can observe if the experimental values follow a *lambertian* behavior and disregard the anomalous maxima that don't.

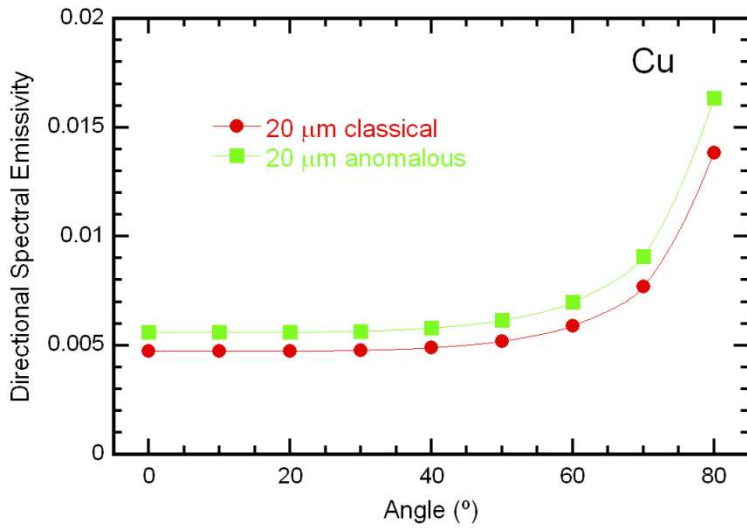


Figure 4.5. Classical and anomalous directional spectral emissivity values for m from 0 to 80 ° for copper at room temperature.

4.4 Experimental results

Copper emissivity measurements between 3 and 22 μm were carried out in the HAIRL radiometer [2]. The measurements were carried out on electrolytic copper films deposited on 60 mm diameter ARMCO iron discs. This sample and the one used in chapter 3 are the same one.

When we look at the curve obtained in the previous chapter for copper at 253 °C (526 K) that is shown again in Figure 4.6 how a broad peak appears between 8 and 14 μm approximately, which is in agreement with predictions made in the anomalous skin effect theory, where the peak reaches its maximum around 10 μm (see Figure 4.3).

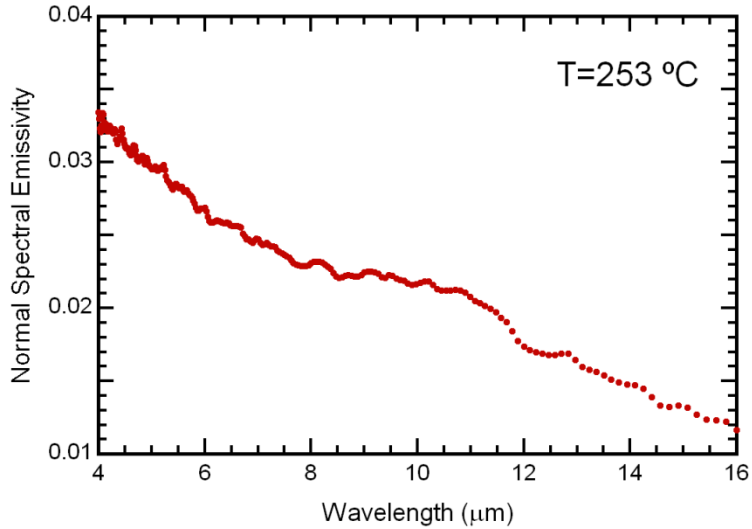


Figure 4.6 Normal spectral emissivity curve of copper at 253 °C (526 K).

Figure 4.7 shows three copper emissivity experimental results as a function of wavelength. Curve (a) corresponds to the curve shown in Figure 4.6. Curve (b) was obtained from literature reflectivity data [82] at room temperature and curve (c), also at room temperature, was obtained using Equation 4.14 with literature optical constant data [20].

where n and k are the real and imaginary part of the complex refractive index.

The curves show evidences of the emissivity broad peak associated to the anomalous skin effect. In the case of curve (a), the broad peak is around 10 μm , as it was stated before. A broad plateau is observed in curve (c) around 16 μm , whereas in curve (b) one can consider that it shows a broad peak between 9 and 29 μm . Since finding the position of a maximum in curve (b) is not easy, curves (a) and (c) will be the ones used for further analysis. Taking into account that ϵ_2 cannot be

obtained experimentally, the experimental ϵ_2 is obtained from $\epsilon_2 = \epsilon_1 \frac{1 - \epsilon_1}{1 + \epsilon_1}$, where ϵ_1 is the experimental curve baseline that replaces ϵ_2 . These baselines cannot be obtained very precisely (in this case a straight line replaces the emissivity from the peak area), and therefore this approach leads to differences between experimental and theoretical values, which also depend on the spectral range of the experimental measurements. As a consequence, it is better to use ϵ_2 , whose values at room temperature and 526 K are in good agreement with the theoretical prediction for those temperatures (17.4 and 9.4 μm , respectively).

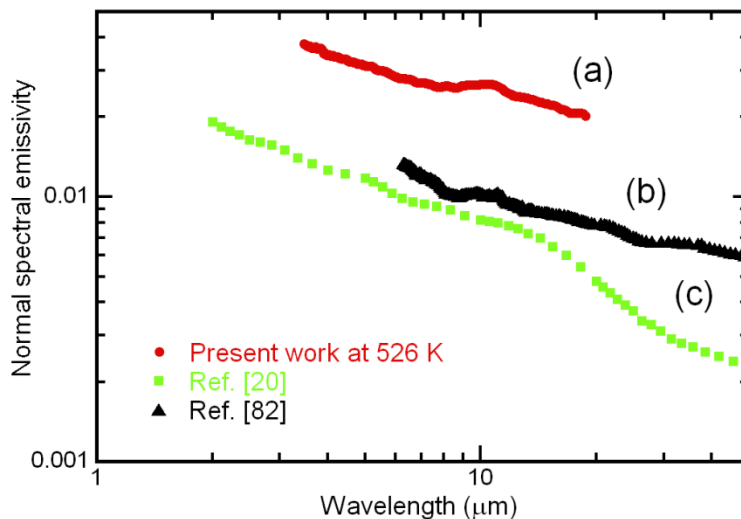


Figure 4.7 Copper normal spectral experimental emissivity ϵ_2 : (a) from radiometric measurements at 526 K; (b) from room temperature reflectivity measurements [82] and (c) from Equation 4.14 using experimental complex refractive index [20].

The broad peak in the three copper emissivity curves in Figure 4.7 together with similar peaks found for aluminum, gold and molybdenum [82-84] are experimental evidence on these metals that suggests an agreement with the prediction with the predictions of the semiclassical

theory of the anomalous skin effect for $p = 1$. As indicated before, the parameter p introduced in the anomalous skin theory has a simple boundary condition which in terms of distribution function is written as $f(v) = pf(-v)$ [64,65], where f is the distribution function for incident and reflected conduction electrons. This boundary condition entails that $p = 1 - W_s$, where W_s is the probability that an electron can be diffusely scattered. The qualitative agreement between Equation 4.7 with experimental results (Fig. 4.7) shows that, according to the boundary condition used in Equation 4.7, W_s should be approximately zero. This probability can be calculated using diffraction theory. Considering electrons as a non-degenerate system, it was found that the surface must be nearly atomically smooth for specular electronic reflection to occur [74]. However, the sample surfaces in Fig. 4.7 have high roughness, particularly those that have been used in the direct normal emissivity measurements. The values obtained should fit better with $p = 0$ but they do it much better with $p = 1$. This result indicates that p is probably not the simple parameter that it is usually assumed to be.

The experimental results in Fig. 4.7 seem to be in agreement with a more general electron gas boundary condition [81] that leads to a new current equation with bulk and surface contributions. In particular, the surface contribution contains two terms associated to the outgoing flux in a particular direction: the specularly reflected electrons and the diffuse ones whose angular distribution depends on the detailed scattering mechanisms at the surface. This means that in degenerate systems an additional weighting factor appears. For this reason, p can be nearly 1, even when the restricted boundary condition gives $1 - W_s = 0$. Thus, the specularity is present in surfaces with larger roughness values than those predicted by the W_s calculus. Therefore, there is a higher maximum roughness value than the one predicted by the dif-

fraction theory. In addition, the roughness does not only affect the functional form of the parameter p but also modifies the absolute value of the emissivity [85]. If the sample has a roughness $r < r_{max}$, the general boundary conditions allows $p = 1$ in the semiclassical theory and the experimental results in Fig. 4.7 must have the same qualitative behavior. However, a quantitative agreement is not possible since the experimental data (absolute value) depends on the roughness value. It is interesting to recall that for a given roughness the reflectivity rises as wavelength increases because the surface is relatively smoother to the incident radiation. This explains not only the differences in the absolute values of emissivity but also the slope differences between the experimental data in the literature and the results obtained with theoretical predictions.

Besides, other considerations must be taken into account. The conventional emissivity concept implies that thermal emission is a surface phenomenon. However, there are evidences to assume that thermal radiation emission is a volumetric process that can often be approximated as a surface process because only a small portion of the volume below the emitting surface contributes significantly to the emitted spectrum. But when we want to observe very small emissivity changes it is compulsory to take into account a small volumetric portion defined as the critical thickness. Therefore, Drude emissivity, emissivity in the anomalous skin effect region, and emissivity due to the surface plasmon could show different effective surface roughness. This concept of volumetric process is in agreement with the idea of a current equation with bulk and surface contributions [81].

Figure 4.8 shows the theoretical and experimental emissivity ratios ($\varepsilon/\varepsilon_{clas}$ and $\varepsilon/\varepsilon_{baseline}$) at 526 K from our work and room temperature from Ordal et al. data [20] respectively. It should be noted that the experimental baseline used in both experimental curves is smaller than

the anomalous region at both temperatures (Figure 4.3) due to the experimental limitations of this method, where the interval is too short in comparison with the anomalous skin effect range. This fact produces important differences between the experimental and the theoretical peak width. The agreement is best at room temperature since the spectral range of these measurements is larger than those at 526 K, and therefore, the experimental baseline is closer to the classical theory prediction. This result is in complete agreement with the influence of roughness on both the theoretical predictions and the quantitative emissivity experimental values. Anyway, more accurate measurements in a broader wavelength spectrum are required in order to see if it is necessary to consider a non-asymptotic approximation [64,65] of the anomalous skin effect theory. This reformulation predicts the same value for the width of the anomalous skin effect region but a peak value lower than the predicted one by equation 4.7.

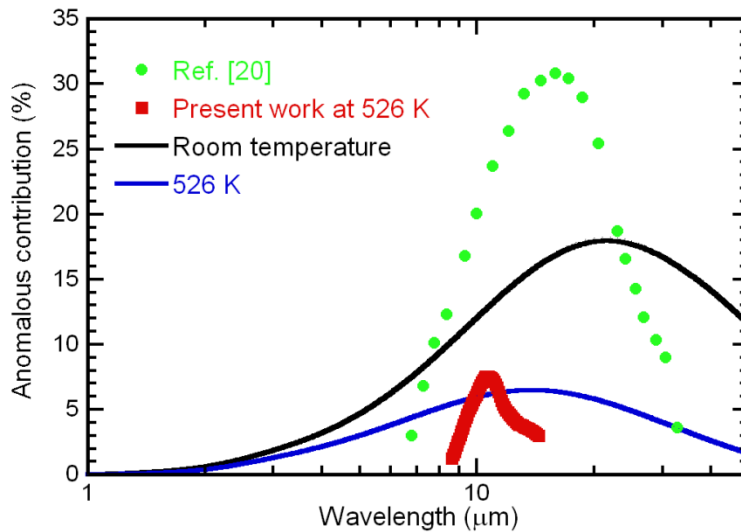


Figure 4.8 Theoretical and experimental emissivity ratios and at 526 K and room temperature [20].

Eventually, the semiclassical theory of the anomalous skin effect predicts that the emissivity position, must be the same for directional and normal measurements (Fig. 4.4) since the theoretical surface impedance predictions showed that the angular dependence is negligible in the anomalous skin effect regime [63,64]. The experimental curves in Figure 4.9 from copper at 523 K show a clear dependence of the broad peak on the incidence angle. This is in agreement with the theoretical curves shown in Figure 4.4, where the broad peak was much larger at 80° than the one at normal incidence. However, the emissivity value rises when the angle increases. This behavior is in agreement with the theoretical prediction if we take into account that, according to the general electromagnetic theory, the emissivity must show an increase when the angle increases [19,24], as it was discussed previously in Chapter 2.

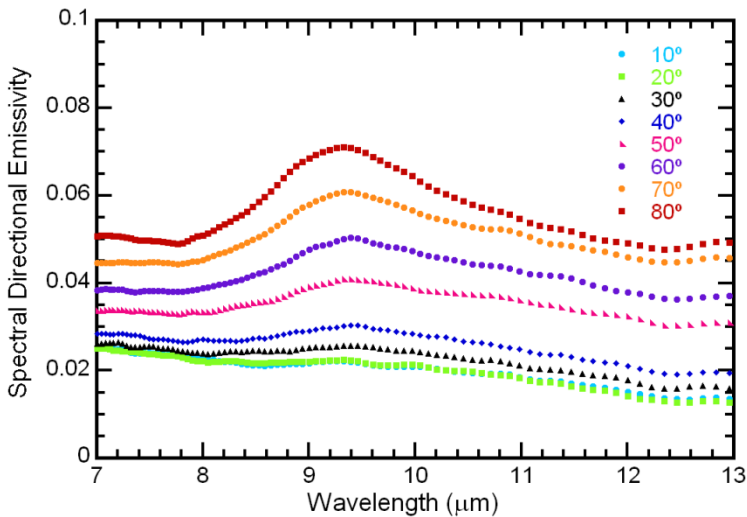


Figure 4.9 Spectral emissivity results on copper at 523 K for eight emission angles. The angular dependence is in agreement with the electromagnetic theory and the asymptotic approach of the anomalous skin effect theory.

Therefore, good qualitative agreement between the experimental and theoretical curves was found. Nevertheless, we find again quantitative differences in the emissivity values. Here they are larger than those we saw for normal incidence because as a result of diffraction effects, the directional properties are significantly influenced by the roughness and the parameter ϵ does not take into account this influence.

In any case, it is interesting to study the emissivity angular dependence for a fixed wavelength. Figure 4.10 provides the experimental and the theoretical copper emissivity for three wavelengths at 523 K. The emissivities are expressed as ϵ_{An} and $\epsilon_{Classical}$. Once again, there is a good qualitative agreement and both are in complete agreement with the predictions of the electromagnetic theory [19,24]. However, the experimental values are not of the same order as the predicted ones. These quantitative differences can be associated with the surface roughness.

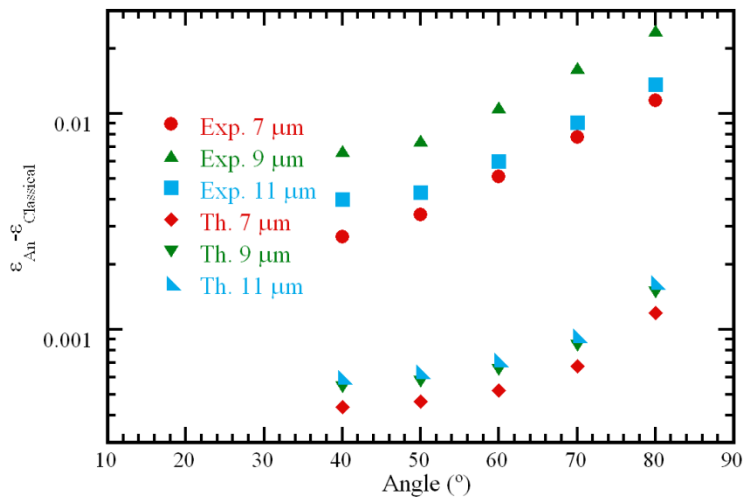


Figure 4.10 Experimental and theoretical copper directional emissivity for three wavelengths at 523 K. The quantitative differences are associated with the surface roughness.

4.5 Conclusions

A complete literature review of the experimental optical constants of twelve metals in the infrared spectral region is presented. According to theoretical predictions these metals have an anomalous skin effect region in the mid and far-infrared at room temperature. Experimental data for Cu, Al, Au, and Mo show signs of a reflectivity broad peak around the wavelength predicted by theory. However, this data does not allow an experimental analysis except for Cu, where the data clearly show the anomalous skin effect for $p = 1$. In this case, experimental emissivity measurements as well as emissivity obtained using optical constants data confirm the predictions of the theory. In particular, the directional emissivity measurements have revealed that the emissivity value increases as well as the broad peak position is independent of the emission angle, being both in complete agreement with the electromagnetic theory. Finally, quantitative comparison between experimental emissivity data with theoretical predictions shows that the specular parameter can be equal to one for roughness values larger than those predicted by the diffraction theory. The present results indicate the need to carry out optical measurements in metals in order to study a wider spectral range, reduce the probable errors, and extend measurements at low temperatures. It also shows that the anomalous skin effect theory needs to be revised and improved since factors such as the roughness are not taken into account.

5 Emissivity of solar selective stacks at working temperature

Uno de los problemas más importantes a los que se enfrenta la industria de la energía termosolar es el desarrollo de recubrimientos selectivos capaces por un lado, de ser capaces de absorber la mayoría de la radiación proveniente del sol, y por otro, de tener la menor cantidad de pérdidas por irradiación infrarroja. Los recubrimientos están formados por un conjunto de capas de espesor nanométrico en donde destacan las de nanocomposites cerámico-metálicos. Hasta el trabajo realizado como parte de esta tesis no se había planteado la necesidad de caracterizar las propiedades ópticas de estos recubrimientos a la temperatura de trabajo. Las propiedades ópticas del recubrimiento a alta temperatura se extrapolaban de los resultados a temperatura ambiente admitiendo que el recubrimiento no presentaba un comportamiento anómalo con la temperatura. En este capítulo se obtienen por primera vez medidas de emisividad infrarroja espectral, así como total, de recubrimientos entre 200 y 600 °C. Además se muestra la necesidad de medir a temperatura de trabajo ya que las extrapolaciones pueden llevar a errores que repercuten *a posteriori* en la eficiencia y como consecuencia en el rendimiento económico de estos recubrimientos.

5 Emissivity of solar selective stacks at working temperature

5.1 Introduction

Solar thermal devices are an alternative to produce heat from the sun for heating systems ($T < 150\text{ }^{\circ}\text{C}$) and also to produce solar thermal electricity ($150\text{ }^{\circ}\text{C} < T < 800\text{ }^{\circ}\text{C}$). In these devices, both the thermal energy storage (TES) and the solar thermal collectors (STC) with different configuration (i.e. flat-plate collector and parabolic concentrated solar collector) have a special relevance. In the case of STCs, the solar absorber surface (SAS) is the most important component. A surface that facilitates the conversion of solar radiation into useful heat should possess two important properties: first, to absorb the incoming solar radiation as much as possible (i.e. high solar absorptivity, α , at the vis-NIR wavelengths) and second, at the same time, to retain the collected heat (high thermal reflectivity, R , or low emissivity, ε , at the NIR-MIR region [86]).

The most common type of absorber is based on materials which are black in the solar radiation range but transparent for the heat, like metal-ceramic nanocomposites (“cermets”). Among all the existing mechanisms, an absorber-reflector tandem consisting of small transition metal particles embedded in a dielectric matrix deposited on a highly infrared reflecting substrate is the most suited method. These thin film coatings offer a high degree of flexibility in order to obtain the desired optical properties to achieve the expected solar selectivity values by changing the thickness, metal volume fraction, and the shape of metal nanoparticles. [87].

Currently, the most commercial SAS are prepared by magnetron sputtering technology, which is a dry, clean and eco-friendly process allow-

ing large area deposition as compared to the electro-chemical methods [88-91]. These SASs are composed of either two or four cermet layers with a graded refractive index [92,93]. The selectivity, defined as the quotient between absorptivity in the vis-NIR region and emissivity in the NIR_MIR region ($s = \alpha/\varepsilon$), can be increased by adding more layers [94] but, in this case, the price increases and durability decreases [95], being the double layer cermets the base for the most successful solar selective coatings for medium-high temperature applications [96-99].

Generally the tandem absorbers are degraded at high operating temperatures due to their unstable microstructure, which cause a decrease in the solar selectivity. One of the essential requirements of solar selective absorbers is their stability when they operate at high temperatures, from approximately 400 to 600 °C. Optical properties of these coatings should not be deteriorated with the temperature rise during the period of use. To accomplish this, new more efficient selective coatings are needed to get both high solar absorptivity ($\alpha > 0.96$) and low thermal emissivity ($\varepsilon < 0.05$) at the working temperature range (400–600 °C). In fact, for high temperature applications, low ε is the key parameter since the thermal radiative losses of the absorbers increases proportionally to T^4 [100].

Figure 5.1 shows the emissivity values obtained from reflectivity curves at room temperature of the two stacks whose emissivity is obtained in this chapter, together with a Planck function for a blackbody at 400 °C and the solar irradiance curve. The green area shows where the spectral emissivity of an ideal collector: high emissivity at short wavelengths and a low one for the longer ones.

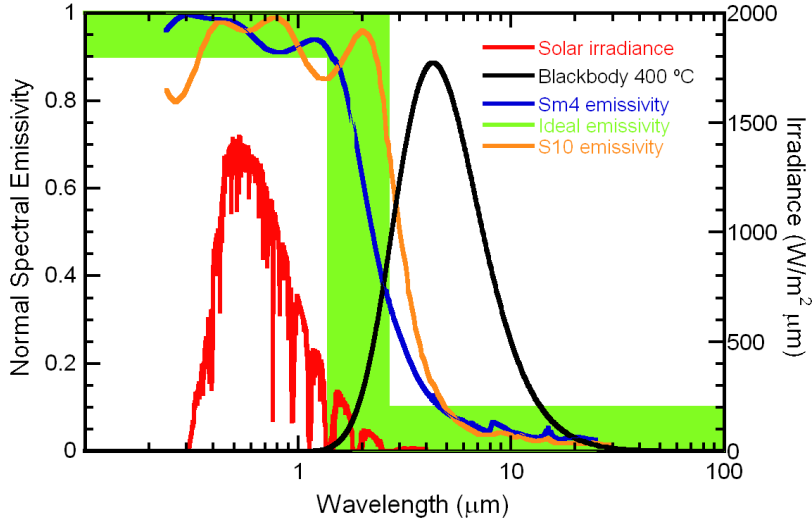


Figure 5.1 Solar irradiance (red) and blackbody radiation at 400 °C (black) together with a SAS emissivity at room temperature of Sm4 (blue) and S10 (orange). The green area shows the emissivity of an ideal collector.

In order to analyze heat losses, a complete knowledge of the radiative properties of the coating structure is essential for their use in high temperature solar collectors. However, a systematic study of direct spectral emissivity as a function of the temperature for a homogeneous cermet two layers has not been performed up until this work. For instance, all the measurements reported in the literature were carried out at room temperature or, at most, at 100 °C. Therefore, the values of emissivity at working temperatures (400–600 °C) are obtained by extrapolation, which can introduce significant errors in the final result. These errors are mainly due to the assumption that the spectral emissivity $\varepsilon_\lambda(\lambda, T)$ of the SAS is constant with temperature. In one of the methods the total emissivity is measured at a fixed temperature, usually at $T < 100$ °C using a commercial emissometer. In the other method, $\varepsilon_t(T)$ is obtained by using the reflectivity spectrum measured at room temperature, $R(\lambda)$, and extrapolating to working temperature T using the following integral:

$$\varepsilon_T(T) = \frac{\int_0^\infty [1 - R(\lambda)]L(\lambda, T)d\lambda}{\int_0^\infty L(\lambda, T)d\lambda}, \quad (5.1)$$

where $L(\lambda, T)$ is the Planck function described in Chapter 2 for the emission of a blackbody and it is the only parameter in Equation 5.1 that is temperature dependent.

Both methods, the one that uses the emissometer and the one that uses the reflectivity, can give $\varepsilon_t(T)$ values that significantly differ from the real sample emissivity at working temperature because the coating spectral emissivity (and therefore the reflectivity) has usually a temperature dependence in the range of wavelengths where radiative transfer occurs. In addition, as it can be observed in other materials [54] the coating can even show an atypical temperature spectral emissivity behavior. Therefore, Equation 5.1 should be replaced by Equation 2.13, explained in Section 2.4 of this dissertation, where the actual spectral emissivity values replace $1 - R(\lambda)$. This fact is crucial since the difference between the values obtained between Equations 5.1 and 2.13 produces an equivalent difference in radiative heat losses. As a consequence, these differences may have a significant economic impact on the final cost of the electricity produced in a thermo-solar plant.

This chapter is focused on two main features: first, on measuring the spectral emissivity of two different types of solar selective absorbers and its substrate between 200 and 600 °C; and second, on demonstrating from an experimental point of view that the analysis of the efficiency of a solar selective coating at its working temperature requires the calculation of $\varepsilon_t(T)$ from the emissivity spectrum measured at that temperature.

5.2 Sample fabrication

The ceramic-metal nanocomposites (cermets) were obtained at the Thin Films Laboratory at the ICMM CSIC institute. 20x20x2 mm plates of stainless steel AISI SS321 were used as substrates for the coatings. The substrate roughness was measured with the Mitutoyo ® rugosimeter and the obtained values were: an average roughness $R_a=0.13 \mu\text{m}$, a root mean square roughness $R_q=0.17 \mu\text{m}$, an average maximum height $R_z=0.87 \mu\text{m}$ and a maximum height of the profile $R_t=2.14 \mu\text{m}$.

Two different stacks are studied in this work. The first one (Sm4) is made of silicon oxide based cermets. The selective solar coating was prepared by sequential sputtering deposition on steel substrate, air-annealed during two hours to develop a thermally grown oxide barrier layer. The base pressure was around 10^{-6} mbar. High purity silver was sputtered with an RF power of 25 W with Ar gas at 5×10^{-3} mbar with a deposition rate of 10 nm min^{-1} . Pure molybdenum and silicon targets were sputtered with DC (1 W) and RF (100 W) respectively. While Mo was sputtered in an Ar gas at a 1.7 nm min^{-1} , the silicon target was sputtered with a 10%O₂/Ar atmosphere at 7 nm min^{-1} rate. The selective solar coating, prepared using these growing conditions, is schematically represented in Figure 5.2. The deposited stack is formed by four layers: (i) a 250 nm thick silver layer acting as IR-mirror, (ii) a 85 nm thick layer of high metal volume fraction (HMVF) cermet composed by Mo and SiO₂ with a 50% filling factor, (iii) a 85 nm thick layer with low metal volume fraction (LMVF) cermet composed by Mo and SiO₂ with a 20% filling factor and, on top, (iv) a 53 nm thick antireflective layer of SiO₂ [31].

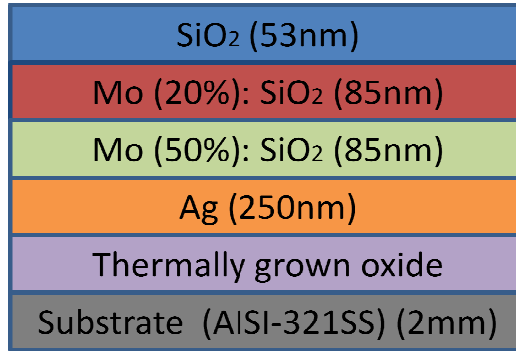


Figure 5.2 Schematic representation of the solar selective coating based in silicon oxide (Sm4).

The second stack is based on silicon nitride (S10) instead of silicon oxide. The same substrate was used and the thermally grown oxide was obtained the same way. Once again, the base pressure was placed around 10^{-6} mbar. A silver layer was deposited by DC sputtering with an Ar atmosphere at 9×10^{-3} mbar at 15 W with a deposition rate of 5 nm min^{-1} . After the silver deposition, the silver layer surface was passivated at the chamber by flowing oxygen, achieving a pressure of 5×10^{-2} mbar during 5 min. Mo-Si₃N₄ cermets were prepared by simultaneous cosputtering of Si and Mo targets using N₂ as the reactive gas at 7×10^{-3} mbar. RF and DC sputtering were performed for Si and Mo respectively. The metal volume fraction was modified by tuning the power supplied to each target. Parameters for a cermet with a 37% filling factor (used for the HMVF layer) are 100 W for both Si and Mo targets to get a 7.1 nm min^{-1} deposition rate. To obtain a 20% filling factor (LMVF layer), the Mo parameter was lowered to 17 W in order to get a 2.7 nm min^{-1} rate instead. The Si₃N₄ antireflecting layer was prepared by RF sputtering of Si with N₂ at 7×10^{-3} mbar and at 100W (deposition rate of 1.7 nm min^{-1}). The schematic representation of the stack is shown in Figure 5.3. The stack is once again formed by four layers: (i) a 175 nm thick silver layer acting as IR-mirror, (ii) a 50 nm thick lay-

er of high metal volume fraction (HMVF) cermet composed by Mo and Si_3N_4 with a 37% filling factor, (iii) a 60 nm thick layer with low metal volume fraction (LMVF) cermet composed by Mo and Si_3N_4 with a 20% filling factor and, on top, (iv) a 80 nm thick antireflective layer of Si_3N_4 [101].

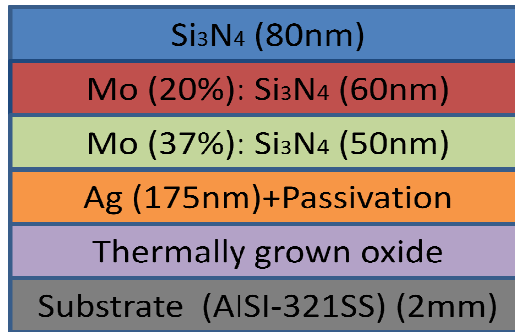


Figure 5.3 Schematic representation of the solar selective coating based in silicon nitride (S10).

5.3 Thermo-radiative properties of solar selective stacks

5.3.1 AISI 321 stainless steel substrate

The normal spectral emissivity measurements were carried out on the steel substrate for five consecutive cycles in a slightly reducing atmosphere (5% H_2 and 95% N_2). Figure 5.4 displays the spectral emissivity curves at two temperatures from the first and the last cycles, where a slight emissivity decrease happens due to the release of surface tensions.

Figure 5.5 shows the emissivity evolution with the cycling at 5, 10 and 15 μm around three different temperatures. As we can see in all three wavelengths there is very little evolution and the variations detected in the last performed cycles are within the error margin.

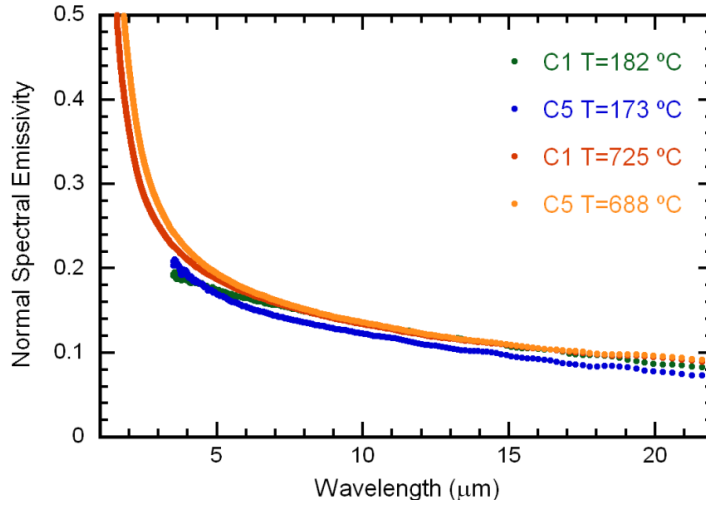


Figure 5.4 Normal spectral emissivity of AISI 321 stainless for a substrate around 180 and 700 °C on the first and fifth cycle.

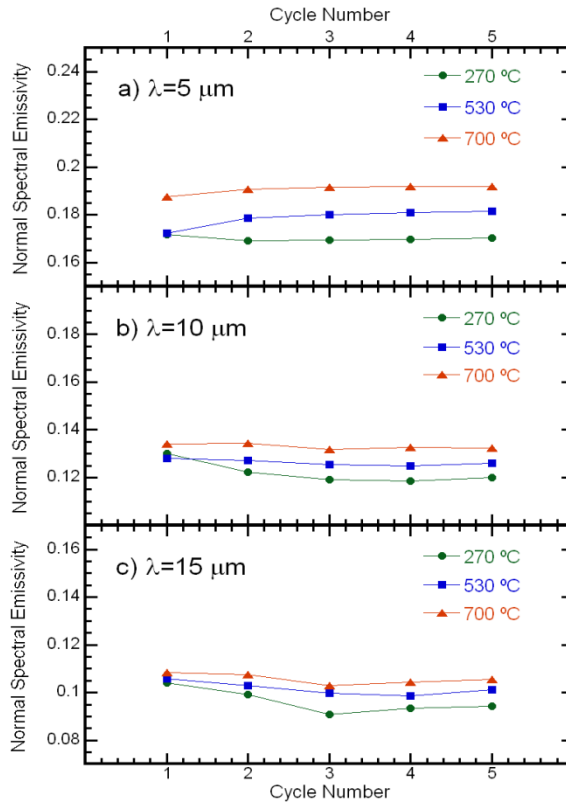


Figure 5.5 Emissivity evolution with cycling at 5, 10 and 15 μm for three different temperatures.

Figure 5.6 shows the normal spectral emissivity for seven different temperatures between 173 and 688 °C during the fifth heating cycle. According to the electromagnetic theory, the emissivity decreases as wavelength increases for metals [19,24]. However, it can be observed that the emissivity behavior undergoes a change between 2 and 3 μm . This is the X point for the stainless steel sample. Above the X point the emissivity increases with temperature, whereas for lower wavelengths the behavior is inversed. Figure 5.7 shows the temperature dependence at four wavelengths. At 2.4 μm , where the X point is located, we can see how the emissivity is temperature independent; whereas at 5, 10 and 15 μm it linearly increases with temperature. Emissivity values at wavelengths below the X point have not been given since data at wavelengths below 2 μm is too noisy (especially at lower temperatures) to be analyzed properly.

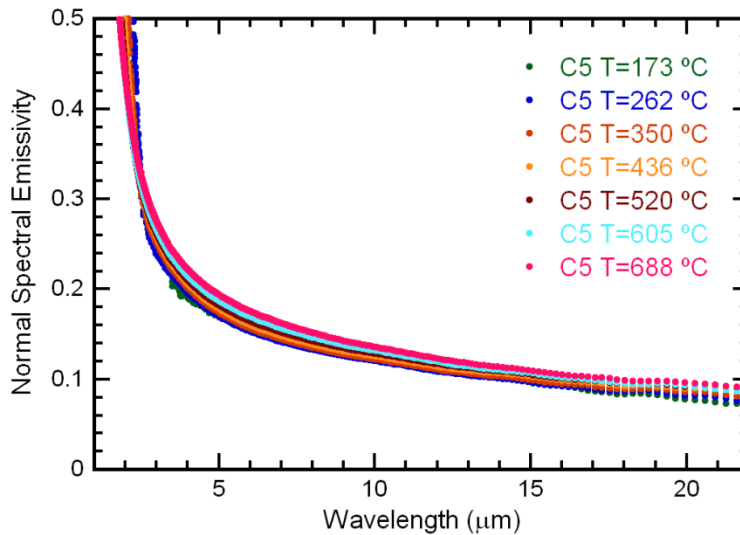


Figure 5.6 Normal spectral emissivity at seven different temperatures for AISI 321 SS.

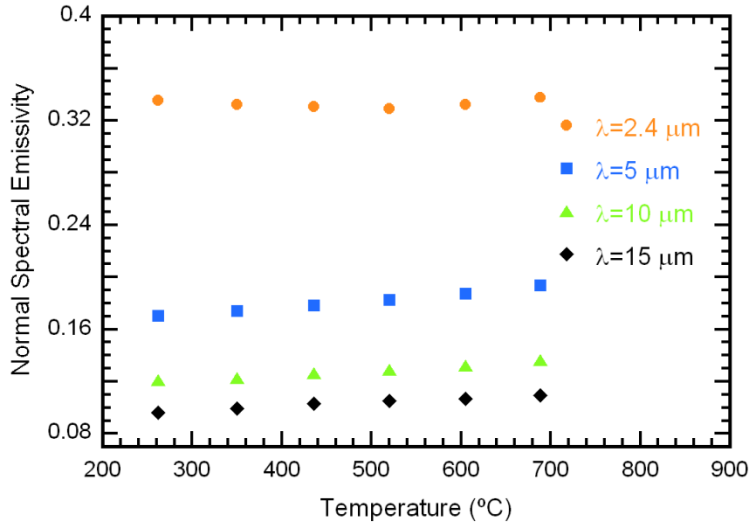


Figure 5.7 Emissivity evolution with temperature at 2.4 5, 10 and 15 μm .

Since the first layer of the selective coating is thermally oxidized steel, an in situ thermal oxidation of the substrate was carried in order to study the variation of the steel emissivity with the oxide thickness. Figure 5.8 shows the normal spectral emissivity during the oxidation process for the substrate at 600 °C with oxidation times up to 22 hours. As expected, the emissivity increases with the oxidation time as it usually happens with metallic materials [18,54,55]. In addition, the first interferential maximum can be observed for $t > 10$ h. Maxima and minima appear when the film is semitransparent in the observed wavelength range. The maxima are located at $\lambda = 2t\sqrt{n^2 - \sin^2 \theta}$ and the minima at $\lambda = t\sqrt{n^2 - \sin^2 \theta}$, where n is the oxide refractive index, t is the film thickness and m is the maximum or minimum order [18,55].

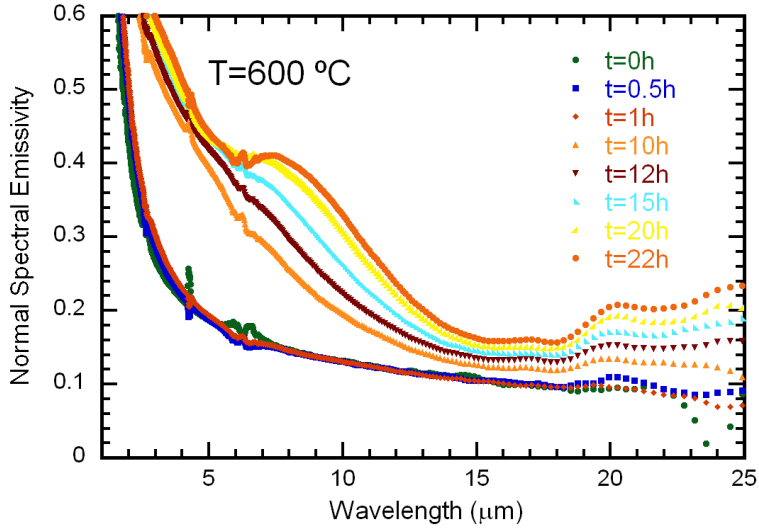


Figure 5.8 Normal spectral emissivity of the substrate for various times during the oxidation process in air at $T=600\text{ }^{\circ}\text{C}$.

5.3.2 Sm_4SiO_2 -based stack

The emissivity measurements of the coating are carried out between 200 and $600\text{ }^{\circ}\text{C}$ and under a moderate vacuum (3×10^{-3} mbar), according to the working conditions in the solar collectors. Four cycles are performed on which emissivity is measured every $30\text{ }^{\circ}\text{C}$ when the temperature is stabilized. Each measurement step takes around 20 minutes and the heating rate was of $10\text{ }^{\circ}\text{C min}^{-1}$, which is the operative heating rate in a solar collector.

Figure 5.9 shows the emissivity values as a function of the heating cycle for two temperatures (325 and $600\text{ }^{\circ}\text{C}$) and four wavelengths (5 , 10 , 15 and $20\text{ }\mu\text{m}$). It can be stated that the emissivity does not evolve during the four heating cycles since it is observed that the emissivity variations between the first and fourth cycle are lower than the experimental uncertainty.

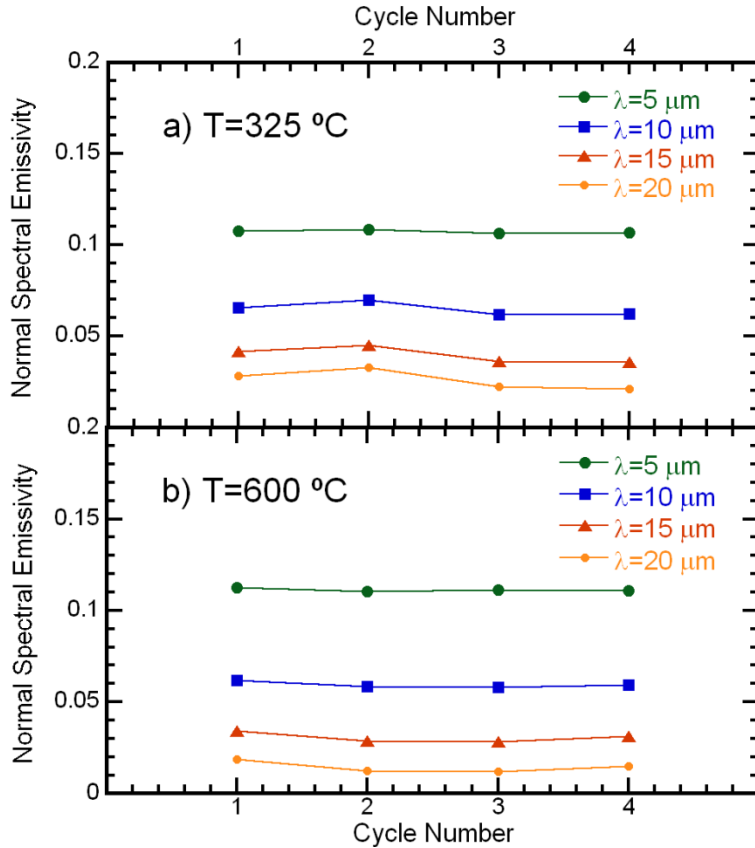


Figure 5.9 Sm4 stack emissivity as a function of the heating cycle at 5, 10, 15 and 20 μm for a) $T=325 \text{ }^\circ\text{C}$ and b) $T=600 \text{ }^\circ\text{C}$.

Figure 5.10 represents the normal spectral emissivity at five temperatures between 236 and 600 $^\circ\text{C}$ during the fourth heating cycle. These emissivity spectra show the behavior of a metal in the mid-infrared range due to the presence of the silver film. If Figure 5.6 and 5.10 are compared it is easily seen that the stack has significantly lowered the emissivity between 3 and 25 μm , where most of the heat between 400 and 600 $^\circ\text{C}$ is dissipated. Below 3 μm there is a drastic emissivity increase, equivalent to the one seen on the reflectivity curve at room temperature in Figure 5.1. This drastic change is done in order to be able to absorb as much solar radiation as possible.

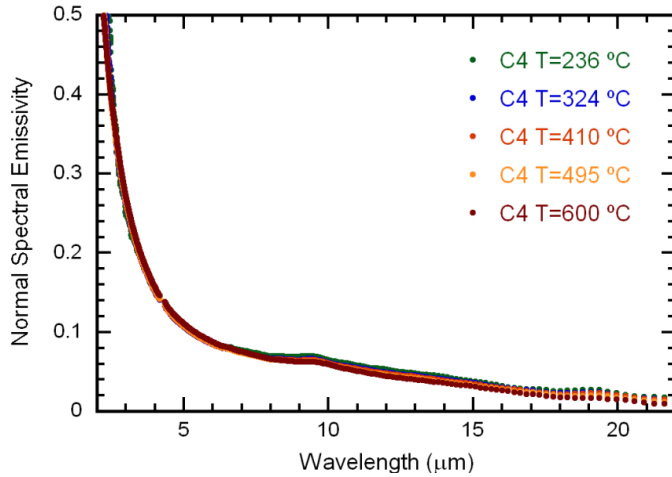


Figure 5.10 Normal spectral emissivity of the Sm4 stack for five different temperatures in the fourth heating cycle.

Figure 5.11 displays the emissivity as a function of temperature for five wavelengths. The emissivity shows an almost negligible decrease at longer wavelengths, stays constant at $5 \mu\text{m}$ and slightly increases at $3 \mu\text{m}$. This type of behavior where the emissivity is almost constant with temperature is good for calculating the total emissivity from reflectivity measurements at room temperature, as we shall see in Section 5.6.

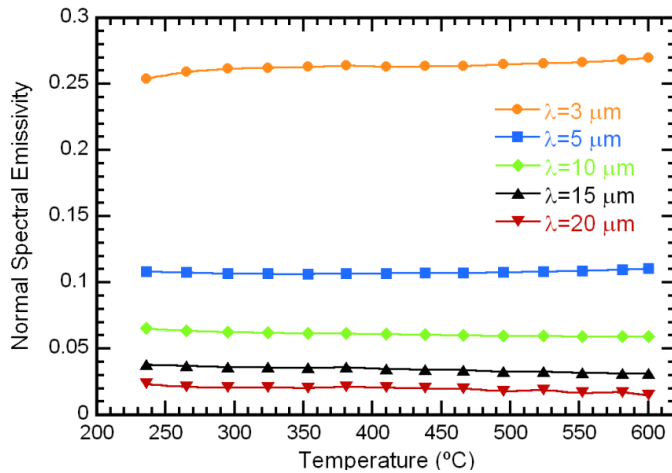


Figure 5.11 Normal emissivity of the Sm4 stack as a function of temperature at the fourth heating cycle for five different wavelengths.

5.3.3 S10 Si₃N₄-based stack

The emissivity of the S10 stack was measured between 200 and 600 °C under the same conditions as the Sm4 stack. Figure 5.12 displays the emissivity values as a function of the heating cycle for two temperatures and four wavelengths. The emissivity presents a clear evolution from the first to the second cycle, but stays constant from the third to the fifth heating cycle.

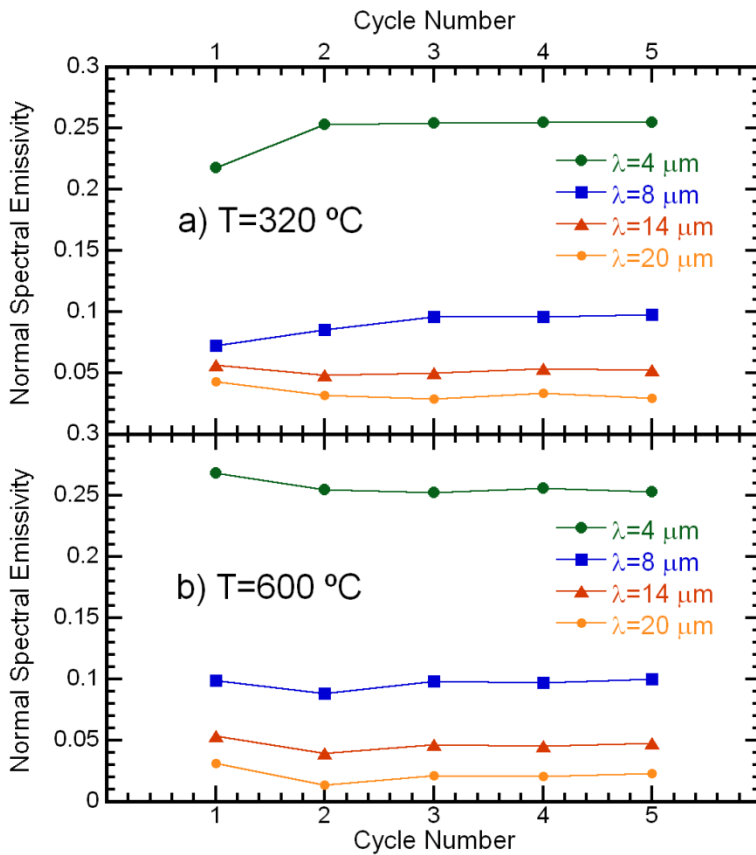


Figure 5.12 S10 stack emissivity as a function of the heating cycle at 4, 8, 14 and 20 μm for a) T=330 °C and b) T=600 °C.

Figure 5.13 shows the normal spectral emissivity at five different temperatures from 226 to 602 °C. Once again a metallic behavior, where the emissivity decreases when the wavelength increases, is observed. This time however, the emissivity values are not as low as the Sm4, especially at shorter wavelengths, where the emissivity strong increase starts happening before 3 μm . This fact is a clear indicative that the selectivity of this coating is not a good one for a solar selective absorber.

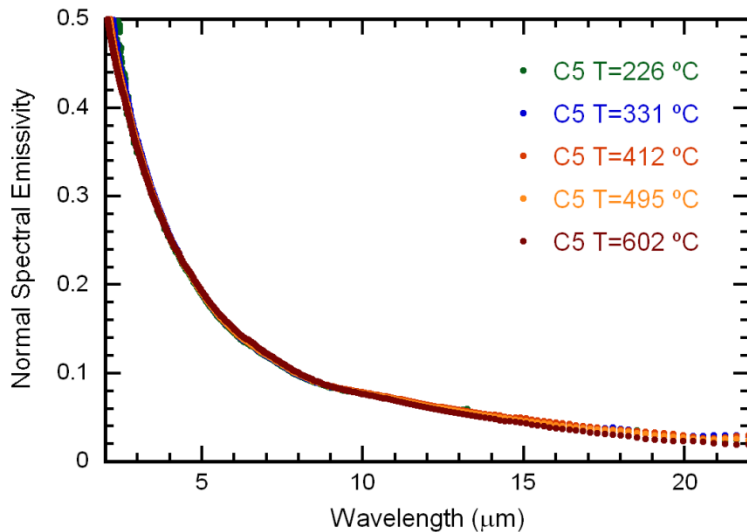


Figure 5.13 Normal spectral emissivity of the S10 stack for five different temperatures in the fifth heating cycle.

Finally, Figure 5.14 represents the emissivity evolution with temperature at four different wavelengths. This time there is a significant difference with the Sm4 stack behavior. While at longer wavelengths such as 5, 9 and 13 μm the emissivity is practically constant, at 2 μm there is a very strong decrease of the emissivity value (around a 30% decrease).

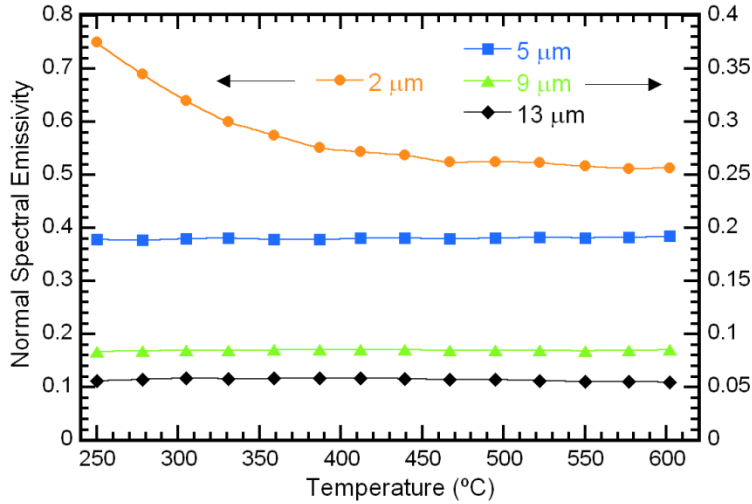


Figure 5.14 Normal emissivity of the S10 stack as a function of temperature at the fifth heating cycle for four different wavelengths.

5.4 Data comparison and total normal emissivity calculation

In Figure 5.15, the spectral emissivity curves from the final cycles of the AISI 321 stainless steel, the Sm4 stack and the S10 stack are compared. Both stacks show a much lower emissivity at long wavelengths. The S10 shows a much poorer performance though in the 3-10 μm range, which is in fact the most important range since the Planck function maximum between 400 and 600 $^{\circ}\text{C}$ is around 3.5-5 μm . In fact, the S10 emissivity at 5 μm is even higher than the one of the substrate. Therefore, it is concluded that the S10 stack is not a suitable one for industrial applications. The Sm4 stack however has at $>10 \mu\text{m}$ and changes from a low emitting material to a high absorbing one between 2 and 3 μm , which is near the ideal wavelength. This makes it a more suitable candidate even if it is far away from the ideal conditions.

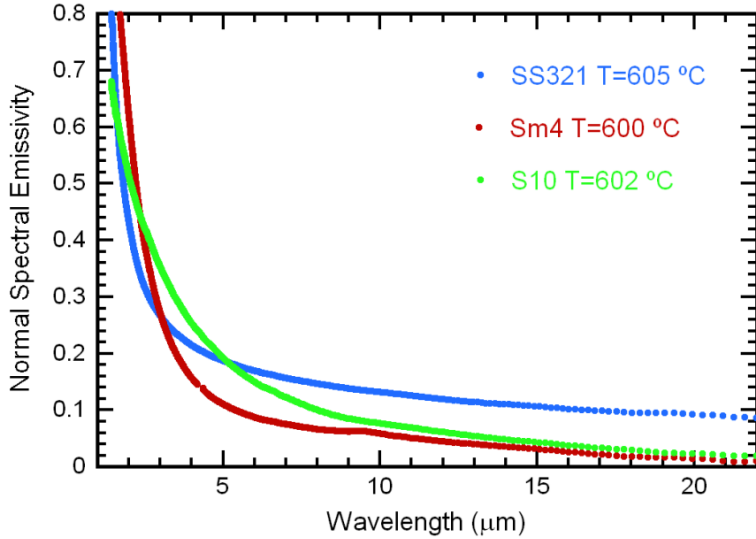


Figure 5.15 Normal spectral emissivity of the SS321 substrate and the Sm4 and S10 stacks.

Finally, an analysis of both main methods total normal emissivity is done. Figure 5.16 shows the total normal emissivity calculus through both methods for both stacks while being compared to the substrate total normal emissivity. As it can be seen in Figure 5.16a the extrapolation method (Equation 5.1) obtains very close results compared to the direct emissivity measurements one (Equation 2.13). This is due to the very weak dependence of the normal spectral emissivity with temperature. The total normal emissivity increases with temperature though. This is because the Planck function evolves with temperature and the weight of the emissivity values at different temperatures varies.

Nevertheless, we can see in Figure 5.16b that the extrapolation method is far from showing the same behavior as the direct one. This is probably due to the stronger dependence of the spectral emissivity with temperature. A conclusion can be made then: it is necessary to measure the spectral emissivity at working temperature in order to make a good calculation of the heat losses in solar thermal collector.

The extrapolation method is only valid when the spectral emissivity is not temperature dependent.

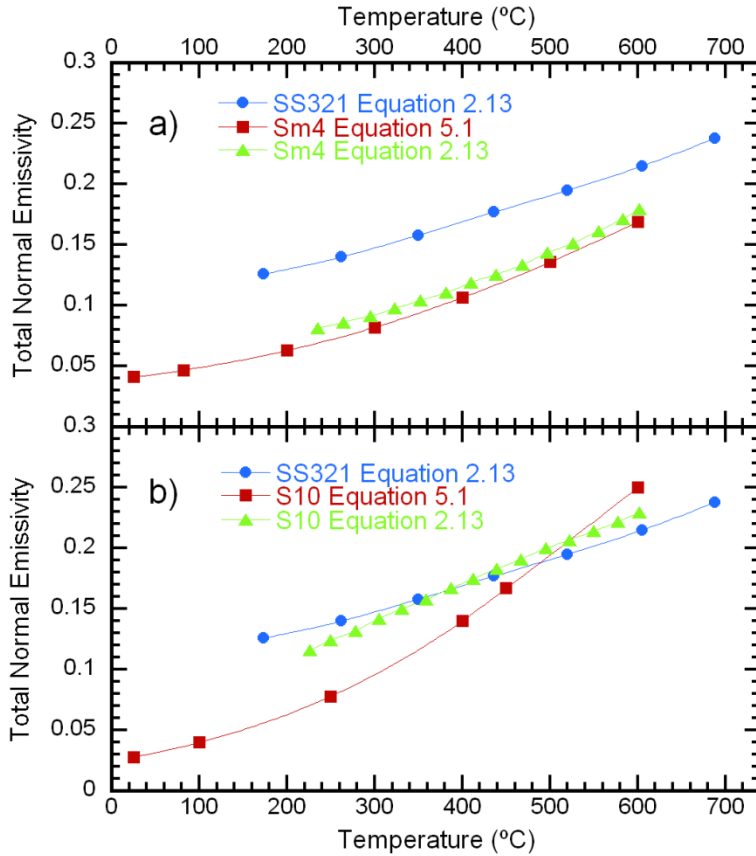


Figure 5.16 Total normal emissivity values calculated with Equations 5.1 and 2.13 for a) Sm4 and b) S10.

5.5 Conclusions

In this chapter it is presented, for the first time, a complete radiometric characterization of two solar selective absorber surfaces by using measurements of spectral emissivity at the whole working temperature range (200 – 600 °C). The total emissivity values obtained from spectral emissivity measurements are compared with those obtained from reflectivity data. This allows knowing the actual behavior of coated

stainless steel system at the operation temperatures for concentrated solar power (CSP) applications. In fact, it is the only way to comprehend the coating performance at high temperatures and its dependence with wavelength. When comparing the total emissivity value calculus of the emissivity measurements and the extrapolation from the reflectivity data at working temperature, it can be seen that both values will only agree when the spectral emissivity does not depend on temperature within the wavelength range in which the radiative transfer is made. When these differences between the two values appear, they introduce significant discrepancies in the calculation of radiative thermal losses and therefore influence significantly in the calculation of the economic profitability of solar power plants. Therefore, the interest of measuring the temperature dependence of the spectral emissivity is fully justified. In addition, it is essential, for solar selective coatings applications, to assess the emissivity changes with heating cycles and heating rate, which can only be proven with spectral measurements at different temperatures.

6 Emissivity of solar thermal energy harvesting PCM Mg-Zn-Al based alloys

Este capítulo pone la mirada en el otro gran problema que presenta la energía termosolar: el almacenamiento térmico. Hoy día el almacenamiento térmico se hace con sales inorgánicas las cuales a pesar de que su precio aún no es alto, almacenan energía haciendo uso del calor sensible. Este hecho presenta, entre otros, dos problemas: grandes dimensiones de complejos sistemas de almacenamiento y un rendimiento pobre. Desde hace años se están estudiando materiales con cambio de fase (PCMs) que el almacenamiento de energía por calor latente. En este capítulo se estudian, con medidas de emisividad, el comportamiento de tres aleaciones eutécticas pertenecientes al sistema Mg-Zn-Al. Estas aleaciones poseen una buena conductividad térmica y alta densidad energética. Se ha medido la emisividad espectral y total infrarroja entre 200 °C y la temperatura de fusión. Este estudio forma parte de un marco en donde es necesario conocer las pérdidas por radiación de los materiales utilizados para almacenamiento térmico. Además, se ha puesto en evidencia la sensibilidad de las medidas de emisividad en las transiciones de fase sólido-sólido resultado que demuestra la alta sensibilidad del radiómetro utilizado.

6 Emissivity of solar thermal energy harvesting PCM Mg-Zn-Al based alloys

6.1 Introduction

In this chapter, the normal spectral emissivity of three alloys from the Mg-Zn-Al system that are candidates for successful thermal energy storage (TES) is studied. These three alloys, Mg-51%Zn, Mg-47Zn-4%Al and Zn-3%Mg-4%Al (mass %), are eutectic compositions that in some previous studies showed promising results [102-104]. They all possess reasonable cost, availability, high latent heat, high heating conductivity and an adequate melting temperature, among others [102-108]. The principal structural and thermophysical properties of these eutectic alloys (melting point, specific heat, heating conductivity, latent heat, etc.) can be found in the literature [102-107, 109,110]. On the other hand, we know that in energy harvesting modeling, heat exchange by radiation needs to be considered. Therefore, the detailed knowledge of all the parameters related to the radiative heat transfer, and among them the thermal emissivity, becomes very important.

Until now the current storage technology in both industrial heat recovery and concentrated solar power (CSP) plants has been based on sensible heat storage using binary or ternary mixtures of simple inorganic salts [111,112]. It is well known that an alternative to sensible storage is the use of phase change materials (PCM) [113-116]. Different potential candidates for PCM with a solid-liquid phase transition have been proposed and in some cases studied in the literature; among them, inorganic salts, paraffins, hydrated salts and fatty acids [113,114,117-121]. Compared to all these materials, the eutectic alloys studied in this chapter, in addition to its high energy density, its constant heat supply and its recovery temperature, have the further ad-

vantage of a high thermal conductivity. This allows a considerable simplification of sophisticated heat exchangers currently used in TES systems [113,122].

Despite these advantages, the various applications of phase change materials are still under investigation [102-104,123-125]. Besides, these storage materials must guarantee a reproducible behavior during a great number of heating cycles because the solar thermal power generation must present a service life of around twenty years. Therefore, the stability of the all the thermophysical properties becomes a crucial requirement. Another requirement, not essential but very competitive, is the absence of oxidation since it avoids using a protective atmosphere.

This chapter has three main objectives related to the possible use of the alloys as part of a TES system: the first one is the measurement of the radiative properties between 200 °C and the melting temperature; then, the stability analysis of the thermophysical parameters; and finally, the study of oxidation in an open air atmosphere. In addition, the experimental results have allowed us checking the sensitivity of these radiative measurements in detecting structural phase transitions in two alloys.

In Section 6.2, the three different samples are described. In Section 6.3, emissivity measurements of the Mg-51%Zn alloy as a function of the heating cycle, wavelength and surface oxidation are shown. Total emissivity measurements as a function of temperature are also applied in order to study sequences of structural phase transitions as well as to analyze the possible metastable phases. Section 6.4 and 6.5 show the same features but for the Mg-47%Zn-4%Al and Zn-3%Mg-4%Al respectively.

6.2. Sample description

The samples were synthesized at the CIC energiGUNE by Risueño et al. [102,104]. Figure 6.1 displays the binary Mg-Zn diagram where the eutectic Mg-51%Zn can be found, while Figure 6.2 is the ternary Mg-Zn-Al diagram. The “E” points in the Mg-Zn-Al diagram refer to the eutectic points. Three of them can be found. However, only two of them (E3 for Mg-%47Zn-4%Al and E2 for Zn-3%Mg-4%Al) are studied here.

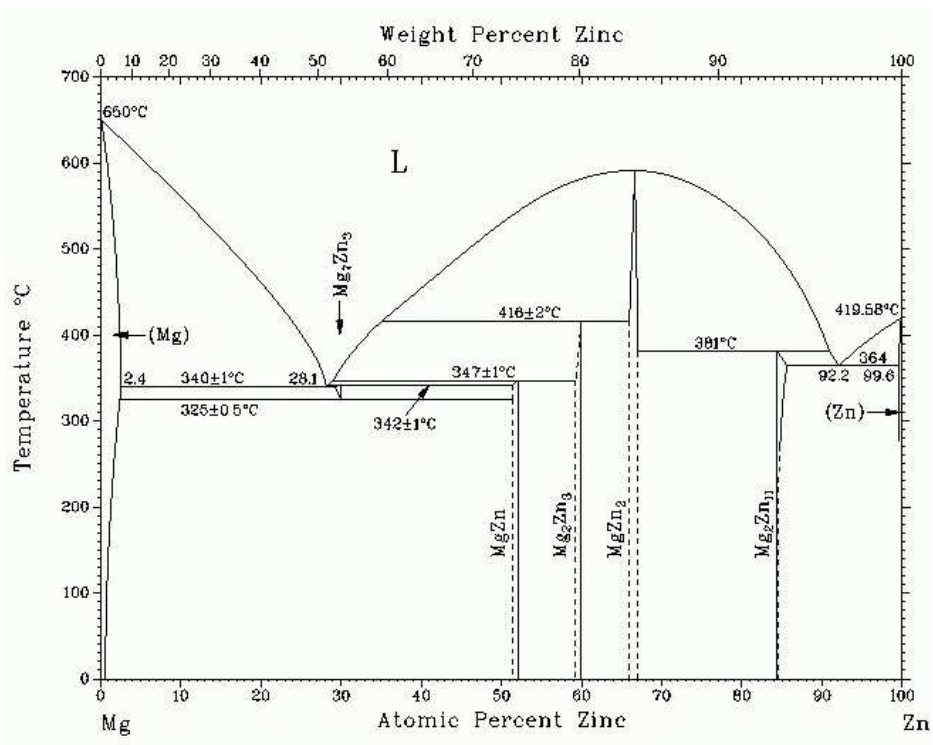


Figure 6.1 Mg-Zn binary phase diagram.

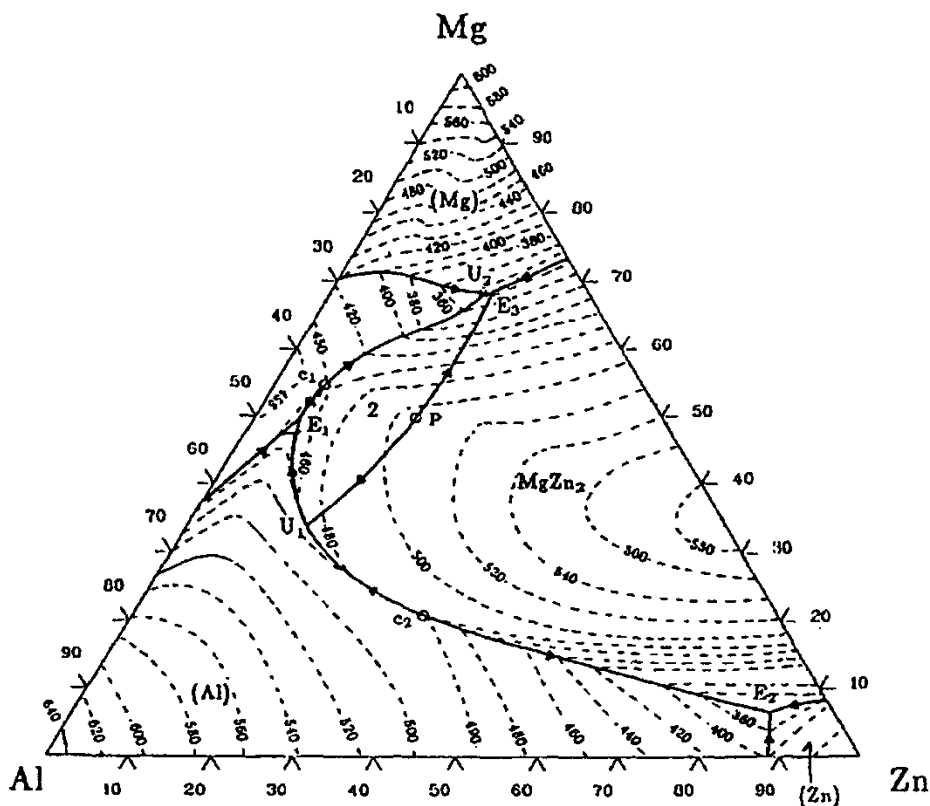


Figure 6.2 Mg-Zn-Al ternary phase diagram.

The three eutectic alloys were synthesized from Mg, Zn and Al ingots with a purity of 99.94, 99.995 and 99.7 % (mass %), respectively. The stoichiometric proportions of the primary metals in the respective alloys were used to prepare pre-alloys with a weight of 60 g of each one. The pre-alloys, previously placed in alumina crucibles, were hermetically closed inside stainless steel reactors under inert argon atmosphere in order to avoid the oxygen presence during the alloying process. The reactors were placed in an electrical muffle furnace and were maintained at 723 K for 10 hours for the ternary alloys, while the Mg-51%Zn alloy was maintained at 923 K for 12 hours. During the melting process, in order to guarantee the homogeneity of the alloys, an external mechanical movement was applied each 30 minutes. After cooling

down at 10 K/min rate, the alloy samples were turned around and the synthesis process was repeated three times. The homogeneity of the prepared materials was confirmed by inductively coupled plasma (ICP - Ultima 2 Horiba) spectrometry [102,104].

The sample roughnesses were also measured with the rugosimeter before placing them inside the chamber. All three sample surfaces were grinded under the same conditions. The roughness parameters are shown in Table 6.1:

Table 6.1 Summary of the three eutectic alloy surface roughnesses: roughness average (R_a), root mean square roughness (R_q), average maximum height (R_z), and maximum height of the profile (R_t).

Sample	R_a (μm)	R_q (μm)	R_z (μm)	R_t (μm)
Mg-51%Zn	0.17	0.21	1.23	1.63
Mg-%47Zn-4%Al	0.11	0.14	0.65	0.93
Zn-3%Mg-4%Al	0.08	0.12	0.94	1.15

Besides, a complete structural and thermal characterization was performed at the CIC energiGUNE, where X-ray powder diffraction (XRPD), scanning electron microscopy (SEM), energy dispersive X-ray spectrometry (EDX) and differential scanning calorimetry (DSC) techniques were used [102,104]. Figure 6.3 shows the DSC measurements and Figure 6.4 the X-ray diffractograms for Mg-51%Zn, Mg-%47Zn-4%Al and Zn-3%Mg-4%Al respectively. Besides the melting points, the DSC shows that both the Mg-51%Zn and the Zn-3%Mg-4%Al alloys present a solid-solid phase transition around 330 and 275 °C respectively when heating up the sample.

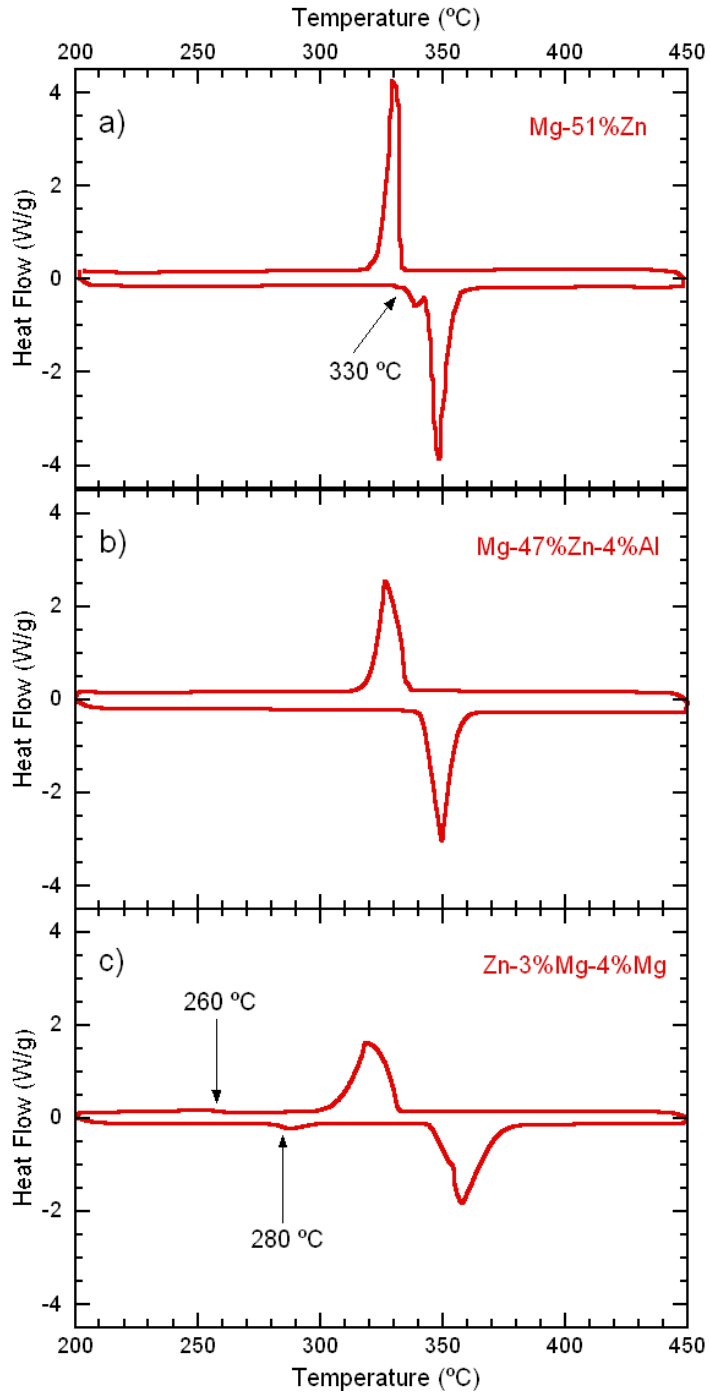


Figure 6.3 Differential Scanning Calorimetry (DSC) measurements for the three eutectic alloys. The Mg-51%Zn and Zn-3%Mg-4%Al alloys show a solid-solid transition around 330 and 275 °C respectively.

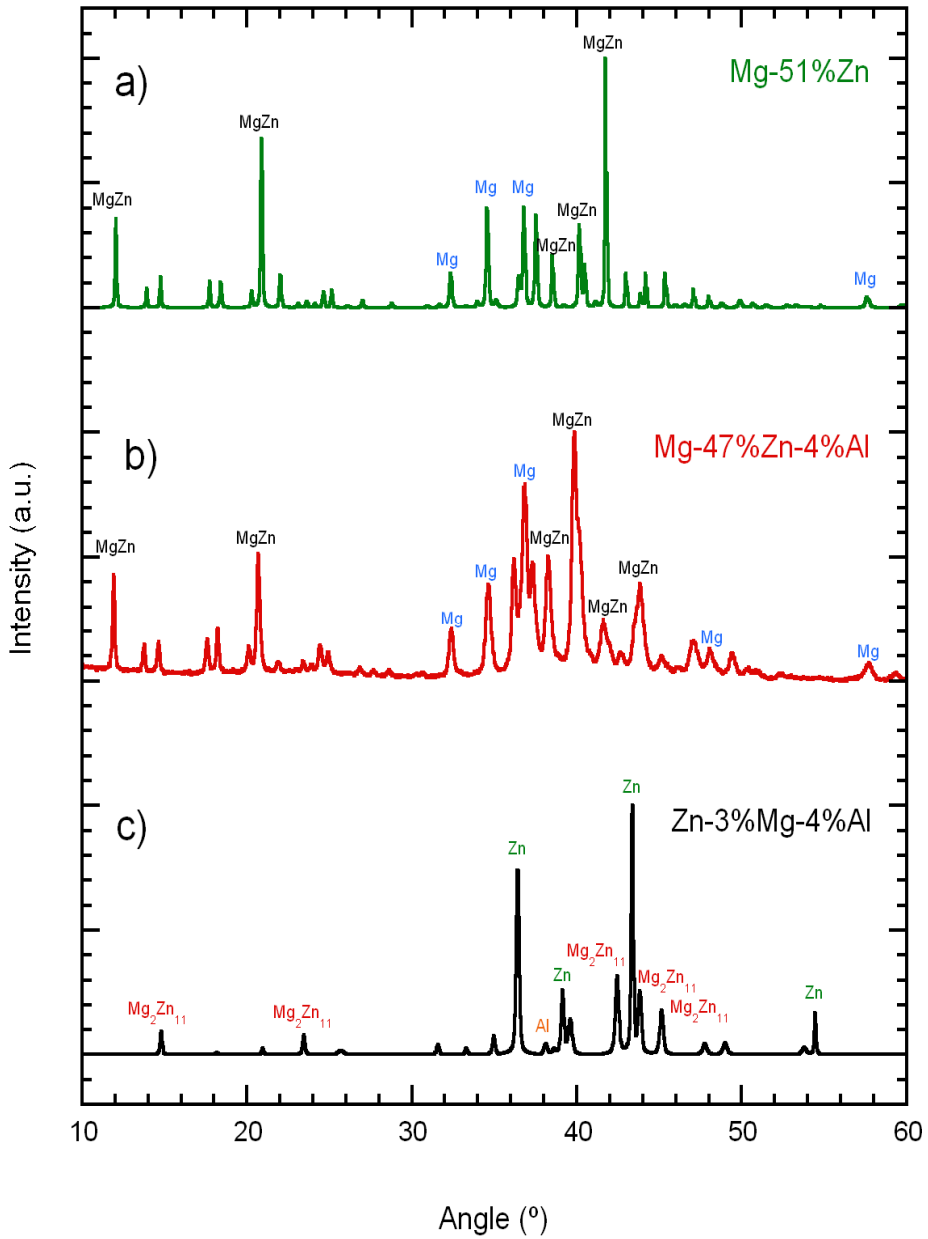


Figure 6.4 X-Ray diffractograms for a) Mg-51%Zn, b) Mg-47%Zn-4%Al and c) Zn-3%Mg-4%Al.

6.3 Mg-51%Zn

In order to analyze the sequence of phase transitions that appear in the phase diagram of the Mg-51%Zn alloy, two types of radiometric measurements along the five heating cycles, shown in Figure 6.5, were performed. First, time-dependent spectral emissivity measurements (Cycles 1-4) at a constant temperature (250 and 330 °C) were done in order to analyze the eutectoid reaction reviewed before. Then, spectral emissivity temperature dependence measurements between 225 and 320 °C (only for Cycle 5) were performed. The red dots in Figure 6.5 show the temperature and time for each radiometric measurement of each heating cycling. X-ray diffraction patterns for phase identification were made at the end of each heating cycle at room temperature (green dots in Figure 6.5). This characterization was made as there is a relationship between the behavior of the emissivity and the phases present in each heating cycle.

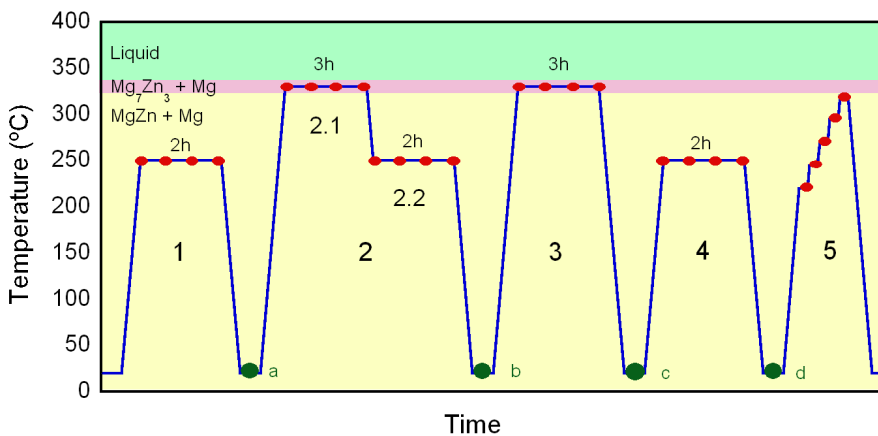


Figure 6.5 Schematic representations of the five heating cycles where the emissivity measurements are carried out. In each cycle, except in Cycle 5, the sample was slowly heated to the measurement temperature (red dots). This temperature is kept constant for the time indicated. In Cycle 5 measurements at various temperatures between 225 and 320 °C are made.

In Figure 6.6, the X-ray diffraction patterns corresponding to the green dots (a-d) displayed between cycles in Figure 6.5, are shown. Spectra of Figures 6.6a, 6.6b and 6.6d correspond to the sample cooled down to room temperature from 250 °C, below the solid-solid phase transition temperature (around 325 °C). The three diffractograms show the peaks associated to the MgZn and Mg phases, the same ones appearing in the X-ray diffraction pattern of the alloy sample before heating cycling. On the other hand, the diffraction pattern displayed on Figure 6.6c is obtained after cooling down freely from 330 °C. In this spectrum a mixture of Mg₇Zn₃, MgZn and Mg phases is observed. These results are in agreement with structural data found in the literature [102] as well as with the phase diagram in Figure 6.1.

In Figure 6.7, the normal spectral emissivity experimental curves obtained from the first four heating cycles are shown. The times indicated for each curve correspond, at constant temperature, to the time elapsed since the beginning of the heating cycle. Figure 6.7a shows, for the heating Cycle 1, the spectral emissivity curves at 250 °C. The sample is kept under isothermal conditions for two hours. It can be seen that emissivity remains constant over time. This behavior is in agreement with the structural results of Figure 6.6 and the phase diagram of the alloy. Throughout the cycle the sample contains Mg and MgZn phases without the presence of metastable phases.

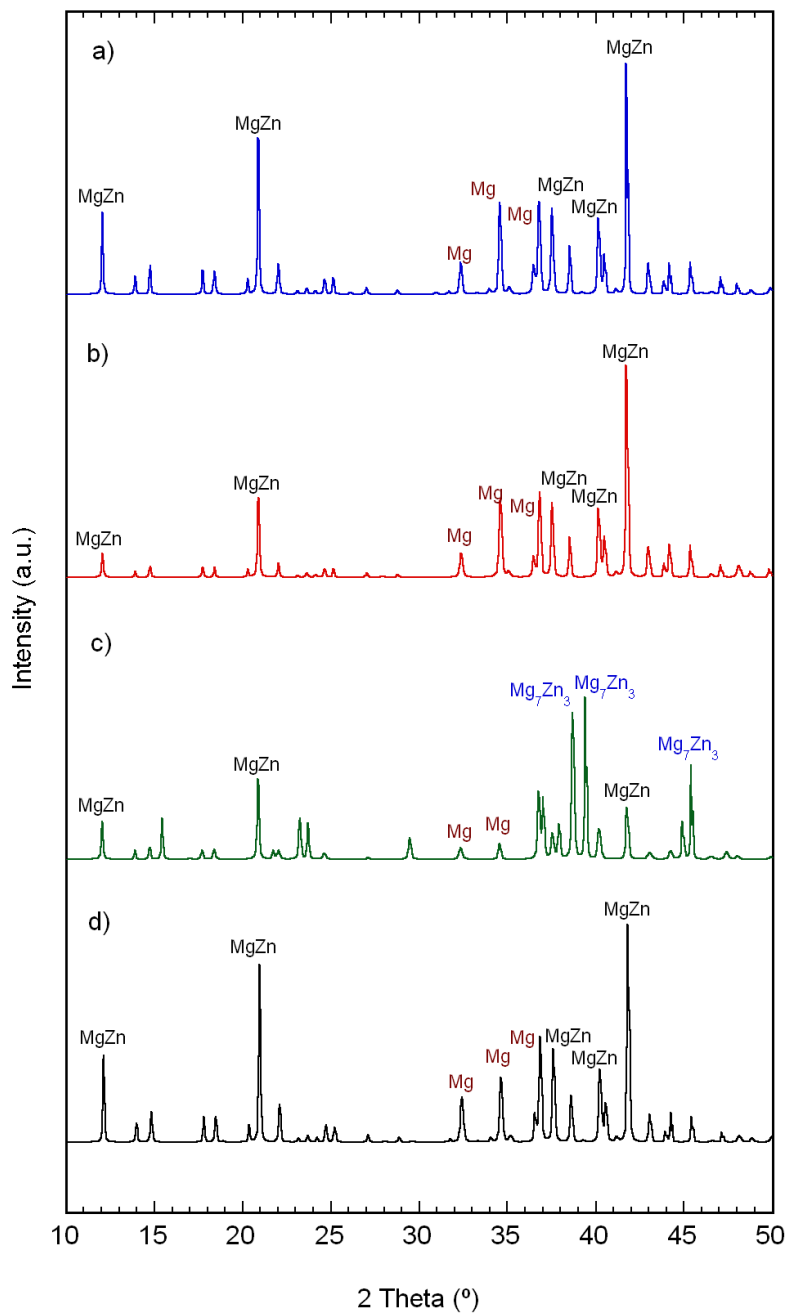


Figure 6.6 X-Ray diffractograms after the each heating cycle. Each diffractogram (a-d) is indicated in where it was performed in Figure 6.5 (green dots). For identification purposes the Mg, MgZn, and Mg₇Zn₃ main peaks are labeled in the diffractograms.

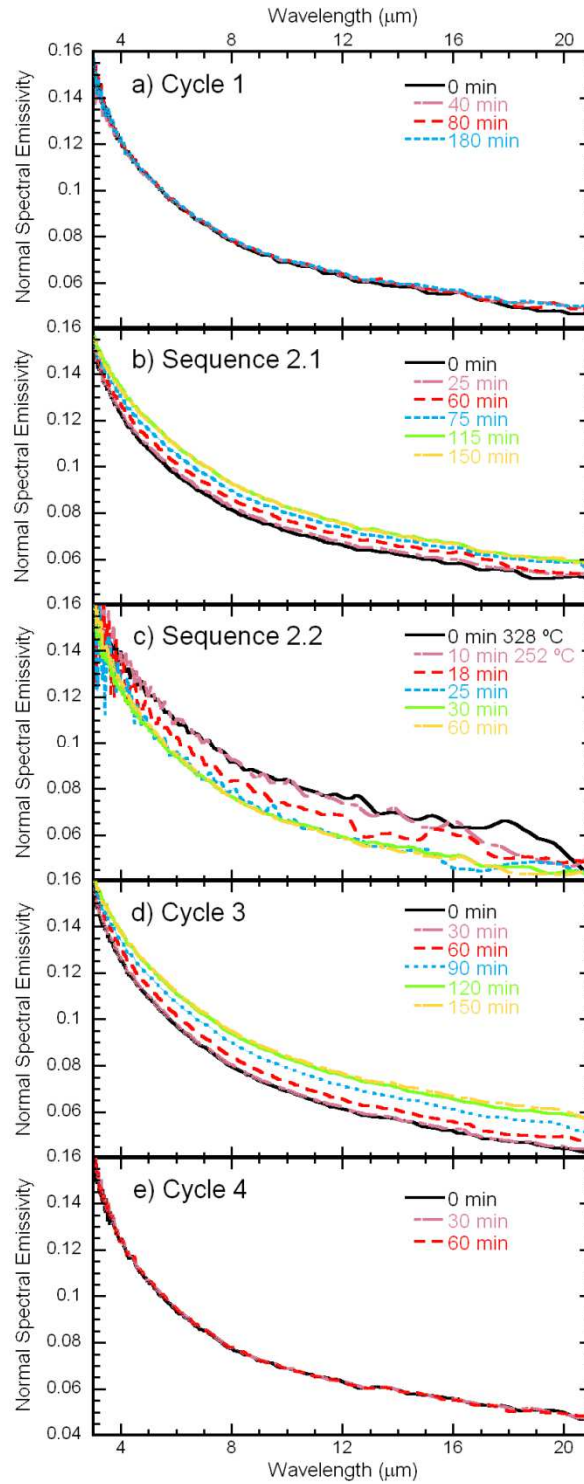


Figure 6.7 Normal spectral emissivity curves for heating Cycles 1-4.

After maintaining the sample for some more time to 250 °C without observing appreciable changes in emissivity, it was cooled down to room temperature and then heated up to 330 °C (Cycle 2). This temperature is above the eutectoid temperature (325 °C) but below the melting one (341 °C). In this cycle spectral emissivity measurements were made at two temperatures. They are called Sequence 2.1 and 2.2 in Figure 6.5. Figure 6.7b displays the spectral emissivity curves from Sequence 2.1 at 330 °C. Here it can be seen that the spectral emissivity values increase for two hours for all wavelengths and afterwards no significant evolution occurs. No growth is observed in the early stages (20 min.). Then it increases for the rest of the two hours and then it stops evolving. These changes in the emissivity values agree with the phase diagram where the $\text{Mg} + \text{MgZn} \rightarrow \text{Mg} + \text{Mg}_7\text{Zn}_3$ transformation occurs at this temperature. Therefore, emissivity becomes constant when the transformation is complete. After 3 hours the sample was cooled down to 250 °C (Sequence 2.2). The spectral emissivity curves of this sequence are shown in Figure 6.7c. The dashed curves in the plot display dynamic emissivity measurements done while the sample is cooling down between 330 and 250 °C. The dashed curves show considerable noise because, in order to obtain several emissivity curves in a short period of time, recording is carried out with a single scan. It is interesting to compare with the noise of other experimental curves in this chapter, which were obtained from 100 scans each. After the temperature stabilized at 250 °C, normal 100-scan measurements were performed. Here it was observed that the emissivity decreases during 20 minutes. When the emissivity becomes stable with time it means that the inverse phase transition is completed. This result confirms the metastable nature of the Mg_7Zn_3 phase [102-104,126], in agreement with the X-ray diffractogram in Figure 6.6b and the phase diagram in Figure 6.1.

In order to confirm the previous analysis, spectral emissivity measurements were made on a new heating cycle at 330 °C (Cycle 3). Figure 6.7d shows the emissivity plot at 330 °C in this cycle. In these conditions, the phases are the same ones as the ones measured in Figure 6.7b and the emissivity results show the same behavior. After two hours the phase transition is completed and the emissivity becomes constant with time. In this cycle, instead of lowering the temperature to 250 °C and staying there for two hours, the sample was cooled down freely to room temperature. In this case, the X-ray diffractograms show the existence of the metastable phase Mg_7Zn_3 at room temperature (Figure 6.6c). This result is in agreement with the fact that the quenching of metastable phases is favored by the fast cooling rates.

In Cycle 4, the sample was heated again to 250 °C. In this case the time-dependent spectral emissivity curves (Figure 6.7e) are in complete agreement with the heating Cycle 1 (Figure 6.7a). This result shows that during heating from room temperature to 250 °C the transformation of the metastable phase is performed. Therefore, the emissivity values must be those of a sample containing the stable MgZn +Mg phases.

In energy storage calculus and simulations is necessary to use total normal emissivity. The value of this physical quantity for each of the heating cycles from Figure 6.5 has been calculated using the Equation 2.14. Figure 6.8a shows the total normal emissivity plots corresponding to the MgZn + Mg phases at 250 °C obtained from Cycle 1, Sequence 2.2 and Cycle 4. In the same figure the solid line shows the variation of temperature with time during the measurement Sequence 2.2. On the other hand, Figure 6.8b displays the total normal emissivity values for the MgZn + Mg \rightarrow Mg_7Zn_3 + Mg phase transition at 330 °C on the Sequence 2.1 and the Cycle 3.

In Figure 6.8a, the values of total normal emissivity are the same for the heating Cycles 1 and 4. Both emissivities slightly increase during the initial minutes and remain constant for the rest of the time. The total normal emissivity of Sequence 2.2 shows a clear decrease over time until it reaches the same value as the one obtained for 250 °C (heating Cycles 1 and 4). From that moment no significant variations are observed. The decrease is performed in three steps. In the first 5 minutes, the sample is cooled down freely between 330 °C and 250 °C. During this step, emissivity dynamic measurements show a decrease of total normal emissivity that is associated with the temperature decrease. In the second step (5 minutes) the temperature reaches 250 °C slowly and experimental measurements indicate that the emissivity remains almost constant. In the third step, however, the decrease of the total normal emissivity is associated to the $\text{Mg}_7\text{Zn}_3 + \text{Mg} \rightarrow \text{MgZn} + \text{Mg}$ phase transition, which occurs for 20 minutes at a constant temperature of 250 °C. On the last phase, when the sample contains only the MgZn + Mg phases, the total normal emissivity remains constant. The differences between experimental values obtained through the three cycles are within the experimental error.

In Figure 6.8b the total normal emissivity curves for Sequence 2.1 and Cycle 3 are plotted. Both curves are similar and show three steps. The $\text{Mg} + \text{MgZn} \rightarrow \text{Mg} + \text{Mg}_7\text{Zn}_3$ phase transition occurs along the second step over two hours with the sample at 330 °C. During this time the total normal emissivity shows a nearly parabolic increase with time. Again it must be remembered that the differences between the two curves are within the experimental error.

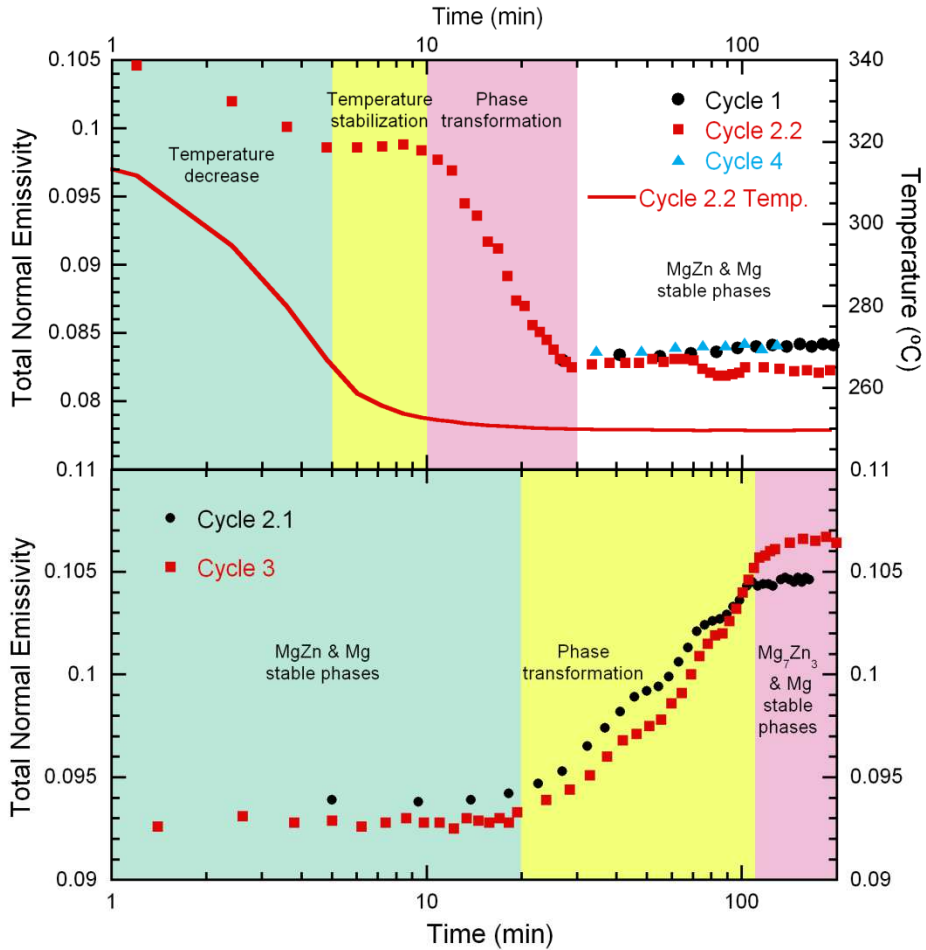


Figure 6.8 Total normal emissivity variation with time for cycles 1-4: a) Cycle 1, Sequence 2.2 and Cycle 4 at 250 °C and b) Sequence 2.1 and Cycle 3 at 330 °C.

Figure 6.9 shows curves for normal spectral emissivity at five temperatures between 225 and 320 °C for Cycle 5. All the measurements are carried once the temperature is stabilized. The emissivity shows a slight increase with temperature, which is the normal behavior among alloys and metals [53,54] and is in agreement with the prediction of electromagnetic theory [19].

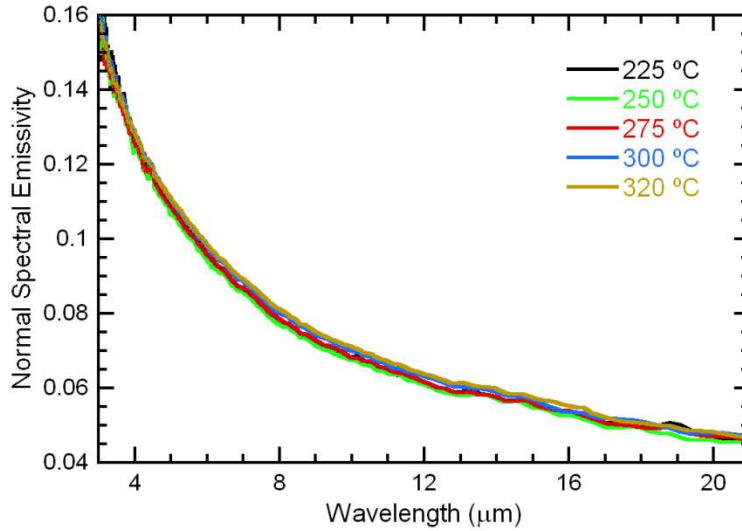


Figure 6.9 Normal spectral emissivity dependence with temperature between 225 and 320 °C.

Another important factor to consider in the TES applications of a given material is its resistance to oxidation. It is therefore interesting to know the process of oxidation of this Mg-51%Zn alloy. The experimental equipment used in this work is capable of obtaining information about this process. Thus, when growing an oxide layer, a record of the emissivity versus time shows typical wave behavior with displaced maximum for each wavelength [18,55]. In this work the alloy is heated in an inert atmosphere. Once the temperature is stable the sample chamber is opened and the emissivity is measured in open atmosphere for 12 hours. None of the recorded emissivity curves show waves associated with the growth of an oxide layer [18,55]. This means that the emissivity does not show significant changes during the measurement time. An example of this behavior is shown in Figure 6.10 for a measuring time of 12 hours at 310 °C. It should be stated that the air absorption peaks have not been eliminated in the green curve in this figure.

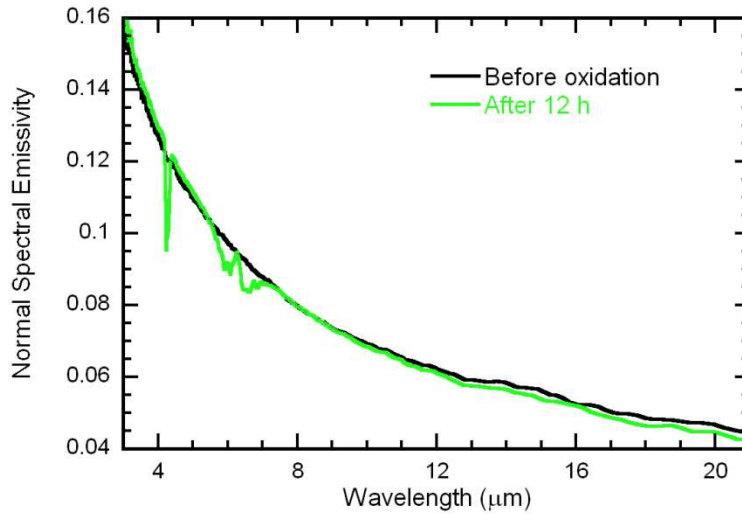


Figure 6.10 Normal spectral emissivity spectra of Mg-51%Zn before and after 12 hours in open atmosphere at 310 °C.

6.4 Mg-47%Zn-4%Al

Due to the lack of solid-solid transitions, the emissivity study of the Mg-47%Zn-4%Al alloy is much simpler than the one for the Mg-51%Zn alloy. The emissivity measurements made will be only temperature dependent ones between 200 and 325 °C since the melting temperature is also around 340 °C. Measurements are performed under an argon gas atmosphere in order to prevent the sample from oxidizing.

Before measuring the emissivity between 200 and 325 °C the sample is heated up to 325 °C, near the melting temperature, and the emissivity is measured for 6 hours at constant temperature in order to see if any evolution is observed. Figure 6.11 shows no significant evolution whatsoever in the entire measuring span. Therefore we can assume that during temperature-dependent emissivity measurements no emissivity variations due to stress relaxations will occur.

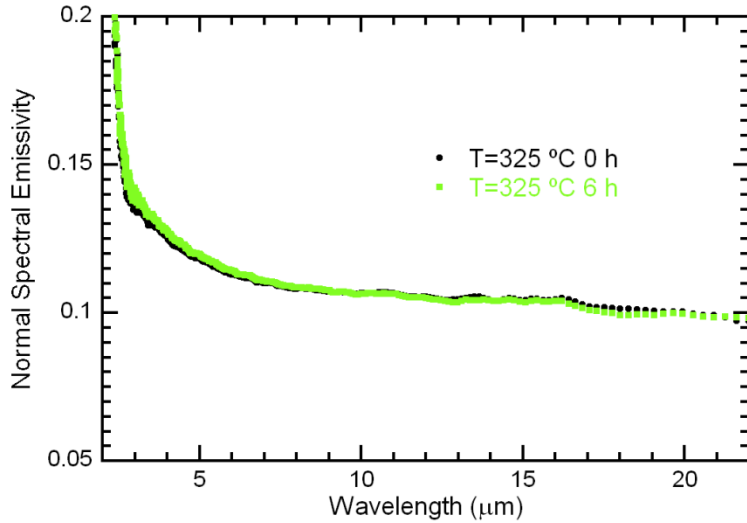


Figure 6.11 Time dependent normal spectral emissivity measurements of Mg-47%Zn-4%Al at 325 °C.

Figure 6.12 displays the spectral emissivity curves at five different temperatures between 200 and 325 °C. The emissivity slightly increases with temperature, especially at higher wavelengths, as it is usual in metallic compounds. The total normal emissivity is also shown in Figure 6.13, where a clear linear dependence with temperature is observed.

Finally, the sample is heated up to 300 °C and afterwards the chamber is opened in order to see whether the sample oxidizes or not. Figure 6.14 shows the normal spectral emissivity curves before the chamber was opened and after 12 hours. Even though there is a very slight increase of the emissivity at larger wavelengths, the results show no apparent oxidation since no significant changes are observed.

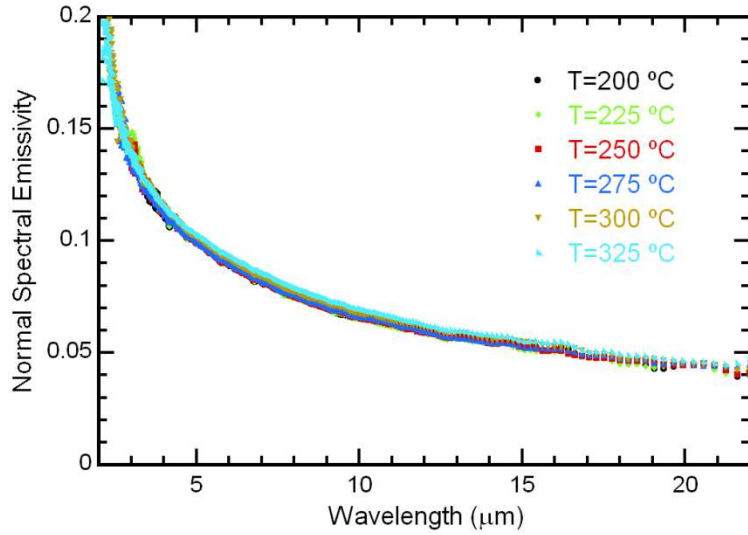


Figure 6.12 Temperature-dependent normal spectral emissivity measurements of Mg-47%Zn-4%Al between 200 and 325 $^{\circ}\text{C}$.

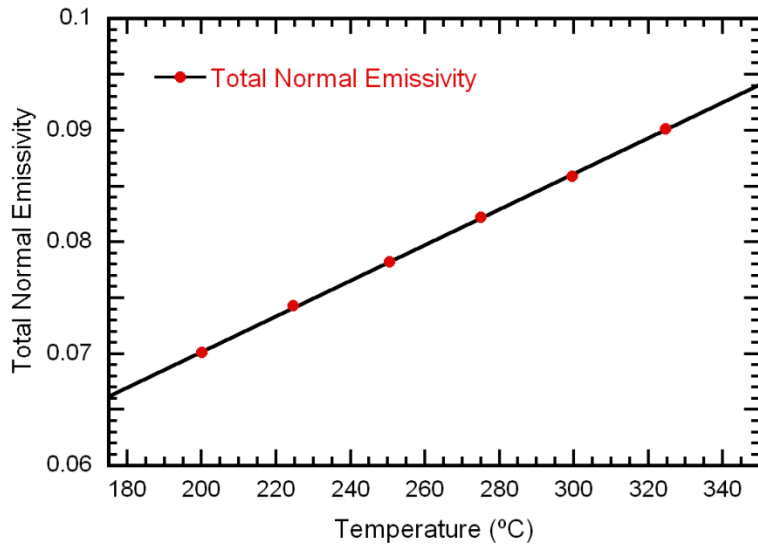


Figure 6.13 Calculated total normal emissivity for Mg-47%Zn-4%Al.

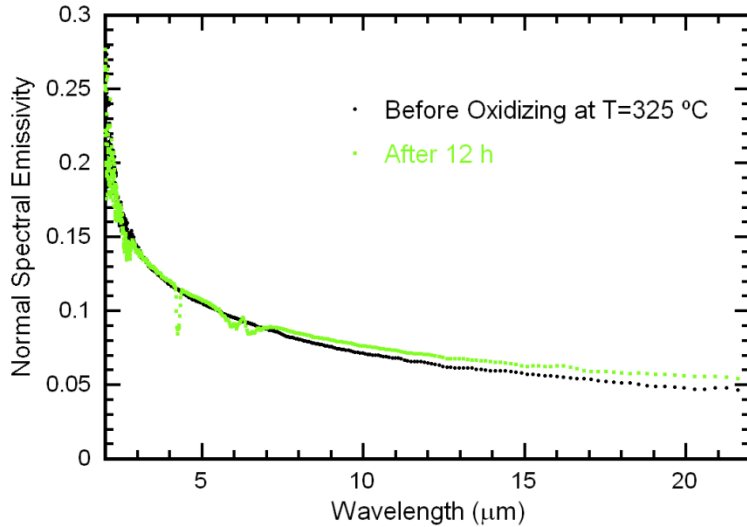


Figure 6.14 Normal spectral emissivity spectra of Mg-47%Zn-4%Al before and after 12 hours in open atmosphere at 325 °C.

6.5 Zn-3%Mg-4%Al

The Zn-3%Mg-4%Al alloy also has a solid-solid phase transition. However, this time this transition occurs over sixty Celsius degrees below the melting point. This fact allows studying the phase transition from a different approach from the one used for the Mg-51%Zn alloy that shows more clearly the phase transitions through hysteresis cycles in the emitted radiation.

Before studying the phase transition the sample is maintained at 250 °C during 8 hours in order to observe if any emissivity variations due to stress relaxations occur. Figure 6.15 shows the normal spectral emissivity at the beginning and after 5 and 8 hours. It can be seen that the emissivity slightly decreases from the first measurement to the one made after 5 hours. After 5 hours the emissivity stops evolving and therefore we can conclude that the sample shouldn't have any stress left from the sample machining.

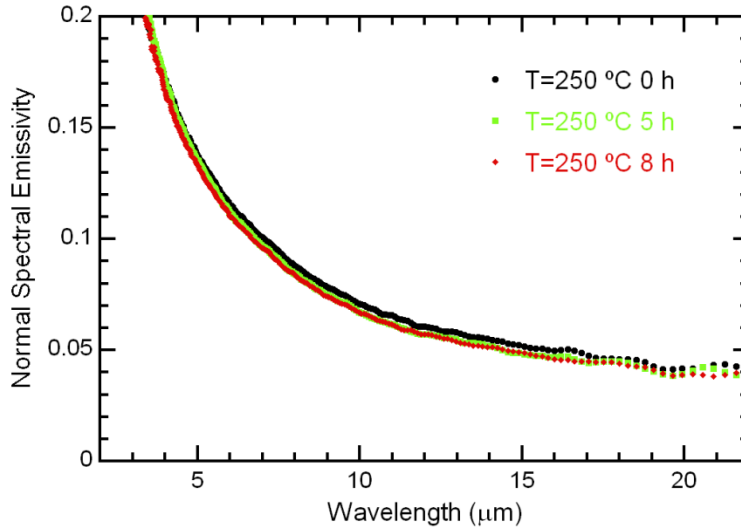


Figure 6.15 Normal spectral emissivity measurements for Zn-3%Mg-4%Al after 0, 5 and 8 hours at 250 °C.

After that three measurement cycles are performed. All the measurements are made when the temperature is stabilized. Cycle 1 measurements are made in heating steps of 10 °C every 14 minutes. The cycle lasts 4 hours in total. Cycle 2 has measurements of both when the sample is being heated up and when it is cooled down. This time 5 °C temperature steps are introduced every 10 minutes. The complete cycle lasts 10 hours this time. The last one, Cycle 3, is similar to Cycle 2 but this time temperature steps of 1 °C every 5 minutes are introduced around the solid-solid phase transition temperature and the 5 °C steps are introduced every 10 minutes when heating up and every 15 minutes when cooling down (this is done since it takes more time for the sample to stabilize when cooling down than when heating up). This cycle is therefore longer (15 hours).

Figure 6.16 shows the total normal emissivity values obtained from the integration of the spectral emissivity curves. Cycle 1 total normal emissivity values (black) show a slight slope decrease around the phase

transition temperature (281 °C). Cycle 2 values (red) show this behavior more clearly both when the sample is heated up (around 280 °C) and when is cooled down (around 260 °C). However the cycle is done too quickly. This is seen on the large discrepancies of the total normal emissivity calculated when the sample is heated up and when it is cooled down. This is probably due to the fact that the sample temperature is not completely stabilized, especially when it is being cooled down. As a consequence a slower cycle is made afterwards. Values from Cycle 3 show a very clear hysteresis cycle between 260 and 285 °C approximately. This is in agreement with the DSC data showed in Figure 6.3, where this phase transition was previously observed.

Once we clearly observe the phase transition we will be able to interpret better the spectral emissivity curves that have been obtained previously. Figure 6.17 shows the normal spectral emissivity curves at six different temperatures. Although the emissivity at longer wavelengths seems to behave the way metals usually do (emissivity increases with temperature), at shorter wavelengths the emissivity seems to decrease above the solid-solid transition temperature. This can be better seen in Figure 6.18, where the emissivity is plotted between 3.5 and 5.5 μm . The emissivity notably decreases from 277 °C (green) right before the beginning of the transition to 282 °C (red), when the transition is occurring. At 292 °C (blue), when the transition has already finished the emissivity is even lower than at 282 °C. Afterwards the emissivity increases as metals usually do (brown triangles at 319 °C).

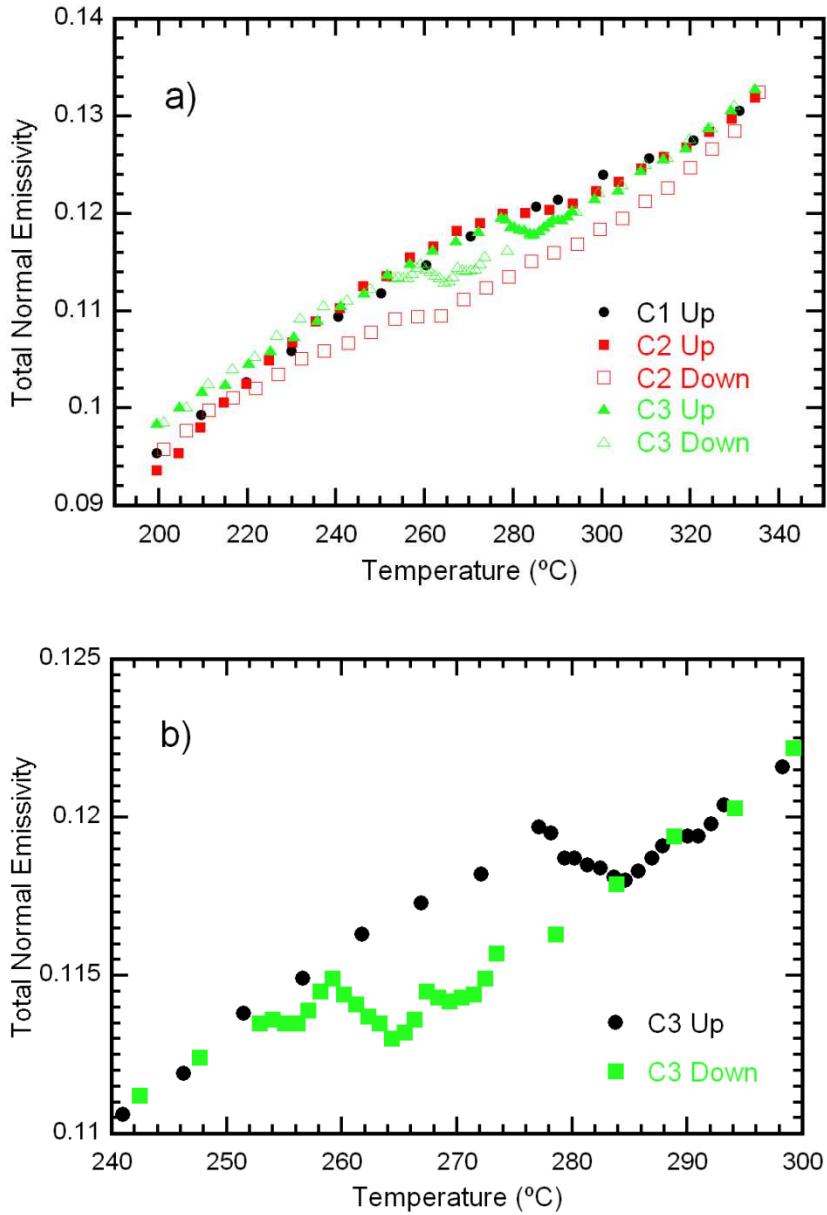


Figure 6.16 a) Total Normal Emissivity values of Zn-3%Mg-4%Al for three different cycles; b) cycle 3 is zoomed around the solid-solid phase transition temperature.

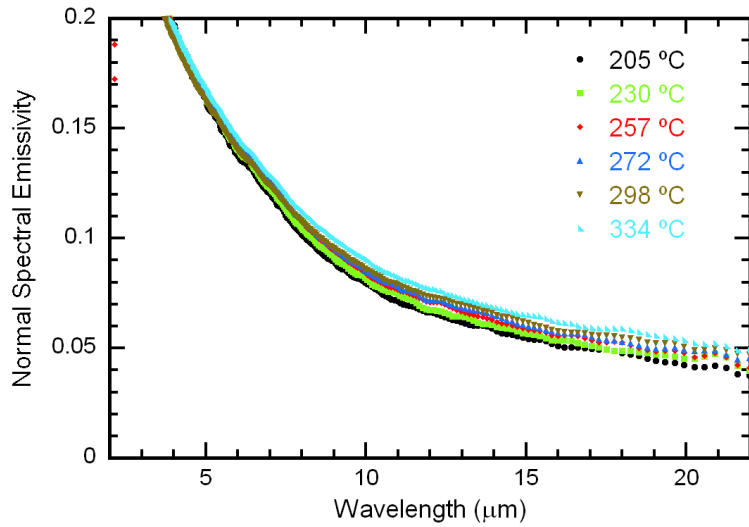


Figure 6.17 Normal spectral emissivity of Zn-3%Mg-4%Al at six different temperatures.

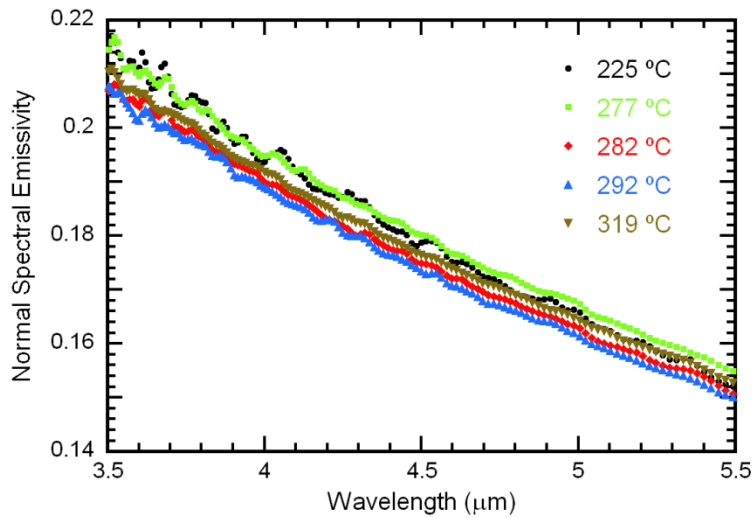


Figure 6.18 Normal spectral emissivity of Zn-3%Mg-4%Al between 3.5 and 5.5 μm at five different temperatures.

Furthermore, if we observe the evolution of the emissivity at certain wavelengths the effect can be seen more clearly. Figure 6.19 shows this evolution with temperature at four different wavelengths. The hysteresis can be easily observed at shorter wavelengths ($7\ \mu\text{m}$). It fades as the wavelength increases until it can no longer be detected by the emissivity measurements at wavelengths such as $15\ \mu\text{m}$.

Finally the sample is also left at an open air atmosphere in order to study a possible oxidation by the evolution of spectral emissivity. However, Figure 6.20 shows that the emissivity does not present neither an emissivity increase at shorter wavelengths nor the presence of interferential maxima and minima usually seen in oxidizing samples [18,55]. Therefore we can conclude that no appreciable oxidation is observed in the mid-infrared area.

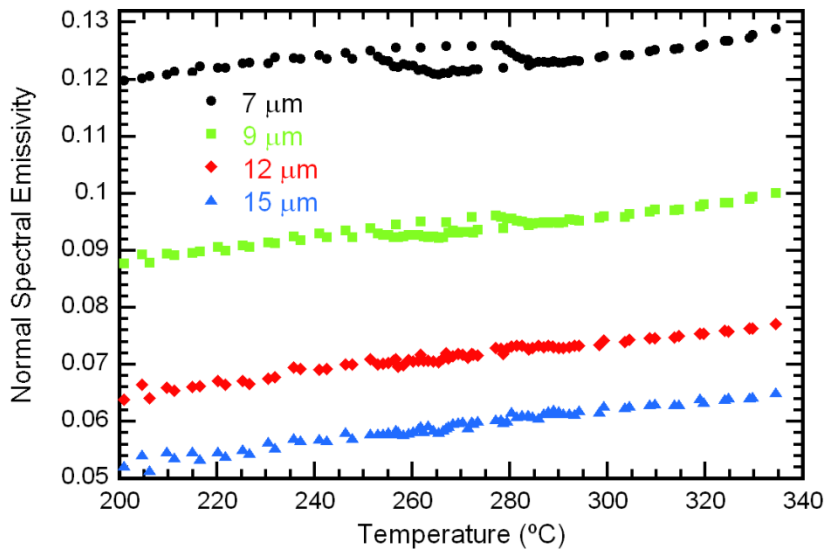


Figure 6.19 Normal spectral emissivity of Zn-3%Mg-4%Al at four different wavelengths.

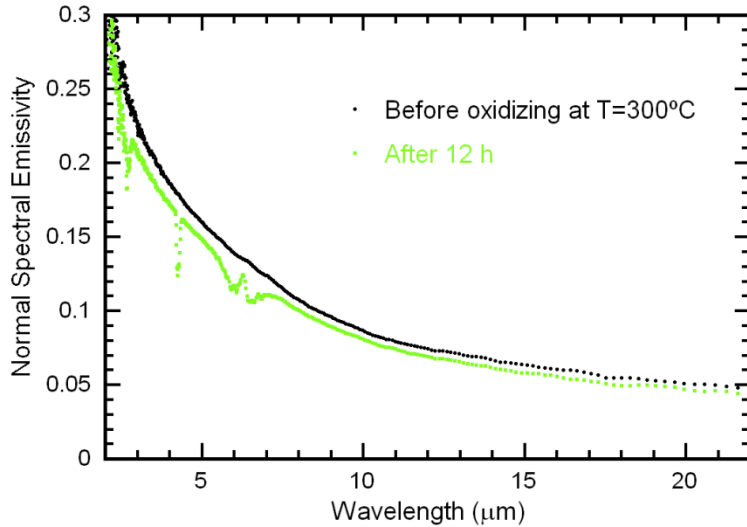


Figure 6.20 Normal spectral emissivity spectra of Zn-3%Mg-4%Al before oxidizing and after 12 hours in open atmosphere at 300 °C.

6.6 Conclusions

The spectral and total normal emissivities of three phase change material alloys, candidates for thermal energy storage, are obtained at their solid states. The emissivity temperature dependence is studied between 200 °C and their melting points. For that, spectral emissivity measurements are performed and the total emissivity is calculated from them. When studying the temperature dependence of the Mg-51%Zn and the Zn-3%Mg-4%Al alloys, solid-solid phase transitions are observed. This shows the radiometer precision and capability when measuring very slight emissivity changes. Besides, all three samples are left for 12 hours at an open air atmosphere to observe possible oxidations. No significant changes in the emissivity related to oxidations are observed, which is a good sign from an economic and logistic standpoint.

Appendix I

In order to obtain the different optical properties we start from a metallic surface where an electromagnetic field is applied. Due to the conduction electron collisions with the net and the field a stationary state whose distribution is given by the Boltzmann equation appears:

$$\frac{\partial f}{\partial t} - \frac{e}{\hbar} \left(\vec{E} + \frac{1}{c} \vec{v} \times \vec{H} \right) \nabla_{\vec{k}} f + \vec{v} \nabla_{\vec{r}} f = -\frac{f - f_0}{\tau}, \quad (A1)$$

where e is the electron charge and τ is the conduction electrons relaxation time. The metallic surface is within the XY plane and the positive side of the Z axis goes inside the metal. The fields are described by:

$$\vec{E} = \vec{E}(z)e^{i\omega t}; \quad \vec{H} = \vec{H}(z)e^{i\omega t}. \quad (A2)$$

Then, the Maxwell equations can be written in the following way:

$$\begin{aligned} -\frac{d\vec{H}}{dz} &= \frac{i\omega}{c} \vec{E} + \frac{4\pi}{c} \vec{J} \\ \frac{d\vec{E}}{dz} &= -\frac{i\omega}{c} \vec{H}. \end{aligned} \quad (A3)$$

Combining them we obtain:

$$\frac{d^2 \vec{E}}{dz^2} + \frac{\omega^2}{c^2} \vec{E} = \frac{4\pi i\omega}{c} \vec{J}. \quad (A4)$$

An extra equation is needed if we want the field and current density relations. This equation can be obtained from the Boltzmann equation. The free electron model is used, where the energy is:

$$\epsilon = \frac{\hbar^2 |\vec{k}|^2}{2m^*} = \frac{\hbar^2 |\vec{k}|^2}{2m}, \quad (A5)$$

where electron effective mass is considered to be equal to its actual mass.

Afterwards, a first order approximation is made on the distribution function.

$$f = f_0 + f_1(\vec{v}, z), \quad (A6)$$

where f_0 is the Fermi-Dirac distribution function:

$$f_0 = f_{F-D} = \frac{1}{e^{\frac{(\epsilon - \mu)}{k_B T}} + 1}, \quad (A7)$$

and f_1 is a function to be determined. If we substitute this distribution function in the Boltzmann equation we have that

$$\frac{\partial(f_0 - f_1)}{\partial t} - \frac{e}{m} \left(\vec{E} + \frac{1}{c} \vec{v} \times \vec{H} \right) \nabla_{\vec{v}}(f_0 + f_1) + \vec{v} \nabla_{\vec{r}}(f_0 - f_1) = -\frac{f_1}{\tau} \quad (A8)$$

It has to be taken into account that:

$$\hbar \vec{k} = 2\pi m \vec{v}. \quad (A9)$$

The equation is simplified since we are in a stationary state. If we also disregard the terms with \vec{H} , $\nabla_{\vec{r}} f_0 = 0$, and $\frac{\partial f_1}{\partial t} = i\omega f_1$, we obtain that:

$$\frac{eE(z)}{mv_z} \frac{\partial f_0}{\partial v_x} = \frac{\partial f_1}{\partial z} + \frac{1+i\omega\tau}{\tau v_z} f_1. \quad (A10)$$

In the classic model the f_1 partial derivative is neglected, the equation solution is easily reached and the current density formula is obtained:

$$f_1 = \frac{e\tau}{m(1+i\omega\tau)} \frac{\partial f_0}{\partial v_x} E(z) \quad (A11)$$

$$\vec{j} = e \int v^2 f_1 d\vec{p} = \frac{e^2 \tau E(z)}{1+i\omega\tau} \int v^2 \frac{\partial f_0}{\partial v_x} \vec{v} = \frac{ne^2 \tau}{m} \frac{E(z)}{1+i\omega\tau} = \frac{\sigma E(z)}{1+i\omega\tau}. \quad (A12)$$

When we want to know the limits of the classical treatment the integrals need to be done taking into account that:

$$E(z) = E_0 e^{-\frac{(1+i)z}{\delta\sqrt{1+i\omega\tau}}}, \quad \delta = \frac{c}{\sqrt{2\pi\omega\sigma}}, \quad (A13)$$

where δ is the field penetration depth at low frequencies ($\omega\tau \ll 1$). When solving the partial derivative of the arbitrary function we get:

$$\begin{aligned} \frac{\partial f_1}{\partial z} &= \frac{e\tau}{m(1+i\omega\tau)} \frac{\partial f_0}{\partial v_x} E_0 e^{-i\frac{(1+i)z}{\delta\sqrt{1+i\omega\tau}}} \left\{ \frac{-(1+i)}{\delta\sqrt{1+i\omega\tau}} \right\} \\ \frac{\partial f_1}{\partial z} &= f_1 \left\{ \frac{-(1+i)}{\delta\sqrt{1+i\omega\tau}} \right\}, \end{aligned} \quad (A14)$$

and therefore its absolute value is:

$$\left| \frac{\partial f_1}{\partial z} \right| \sim \frac{f_1}{\delta(1+\omega^2\tau^2)^{\frac{1}{4}}}. \quad (A15)$$

The equation A10 other term's modulus is:

$$\left| \frac{1 + i\omega\tau}{\tau v_z} f_1 \right| \sim f_1 \frac{(1 + \omega^2\tau^2)^{\frac{1}{2}}}{l}, \quad (A16)$$

where $l = \tau|\vec{v}|$ is the mean free path. We can put both expressions all together and we have that:

$$\frac{l}{\delta} \ll (1 + \omega^2\tau^2)^{\frac{3}{4}}. \quad (A17)$$

At very low frequencies ($\omega\tau \ll 1$) the mean free path is much lower than the penetration depth.

At high frequencies ($\omega\tau \gg 1$) the electron is required to travel short distances through a field period compared to the penetration depth.

Therefore, A17 represents the conditions in which the classical behavior happens; at very high and very low frequencies. The equation can also be written as:

$$\gamma\tau \ll \omega\tau \left(1 + \frac{1}{\omega^2\tau^2}\right)^{\frac{3}{4}}, \quad (A18)$$

where gamma is a constant. The function tends to the infinite in both $\omega\tau = 0$ and $\omega\tau = \infty$ and has a minimum for

$$\omega\tau = \frac{3^{\frac{3}{4}}}{2^{\frac{1}{2}}}. \quad (A19)$$

Equation A17 must be fulfilled for high and low frequencies at any collision time. Nevertheless, when temperatures are not very high and τ is large, there is a frequency where the relation is no longer valid.

In this case we have to go back to Equation A10, where $\frac{\partial f_1}{\partial z}$ cannot be neglected for the general case. The equation obtained after integrating is the following one:

$$f_1 = e^{-\frac{(1+i\omega\tau)z}{\tau v_z}} \left[F(\vec{v}) + \frac{e}{m v_z} \frac{\partial f_0}{\partial v_x} \int E(t) e^{-\frac{(1+i\omega\tau)t}{\tau v_z}} dt \right], \quad (A20)$$

where $F(\vec{v})$ is an arbitrary function that needs to be determined. In order to achieve it, two different situations with two different equations are studied: $f_1^{(1)}$ y $f_1^{(2)}$, where the first one is for $v_z < 0$ and the second one for $v_z > 0$. Besides, f_1 must be small when $z \rightarrow \infty$, so:

$$f_1^{(1)} = -\frac{e}{m v_z} \frac{\partial f_0}{\partial v_x} e^{-\frac{(1+i\omega\tau)z}{\tau v_z}} \int_z^\infty E(t) e^{-\frac{(1+i\omega\tau)t}{\tau v_z}} dt \quad (A21)$$

For the second function the scattering is considered the following way: a fraction p of the electrons will be dispersed specularly while the rest $(1-p)$ will do it diffusely. p is considered to be independent of the electron movement direction. Therefore, the electrons that abandon the surface will have the following distribution function:

$$\begin{aligned} f_0 + f_1^{(2)}(v_x, v_y, v_z, z = 0) = \\ = p \left[f_0 + f_1^{(1)}(v_x, v_y, -v_z, z = 0) \right] + (1-p)f_0. \end{aligned} \quad (A22)$$

This determines $F(\vec{v})$ for $v_z > 0$.

$$\begin{aligned} f_1^{(2)} = p f_1^{(1)}(v_x, v_y, v_z, z = 0) = \\ = \frac{e}{m v_z} \frac{\partial f_0}{\partial v_x} e^{-\frac{(1+i\omega\tau)z}{\tau v_z}} p \int_z^\infty E(t) e^{-\frac{(1+i\omega\tau)t}{\tau v_z}} dt = \end{aligned}$$

$$\frac{e}{mv_z} \frac{\partial f_0}{\partial v_x} e^{-\frac{(1+i\omega\tau)z}{\tau v_z}} \left[p \int_0^\infty E(t) e^{-\frac{(1+i\omega\tau)t}{\tau v_z}} dt + \int_0^z E(t) e^{-\frac{(1+i\omega\tau)t}{\tau v_z}} dt \right]. \quad (A23)$$

If we take into account that $E(z) = E(-z)$; $z < 0$, we observe that:

$$\begin{aligned} f_1^{(2)} &= \frac{e}{mv_z} \frac{\partial f_0}{\partial v_x} e^{-\frac{(1+i\omega\tau)z}{\tau v_z}} p \int_{-\infty}^z E(t) e^{-\frac{(1+i\omega\tau)t}{\tau v_z}} dt + \\ &+ \frac{e}{mv_z} \frac{\partial f_0}{\partial v_x} e^{-\frac{(1+i\omega\tau)z}{\tau v_z}} (1-p) \int_0^z E(t) e^{-\frac{(1+i\omega\tau)t}{\tau v_z}} dt. \end{aligned} \quad (A24)$$

These two equations are precisely the solutions we were looking for.

Now that we know the distribution function the current density can be calculated.

$$J(z) = -2e \left(\frac{m}{h} \right)^3 \iiint v_x (f_0 + f_1) dv_x dv_y dv_z. \quad (A25)$$

Using the equations A21 and A24 in polar coordinates we have that:

$$\begin{aligned} J(z) &= -\frac{2\pi e^2 m^2}{h^3} \int_0^\infty v^2 \frac{\partial f_0}{\partial v} dv \int_0^{\frac{\pi}{2}} \sin^3 \theta \sec \theta d\theta \times \\ &\left[p \int_{-\infty}^z E(t) e^{-\frac{(1+i\omega\tau)(t-z)}{\tau v_z} \sec \theta} dt + (1-p) \int_0^z E(t) e^{-\frac{(1+i\omega\tau)(t-z)}{\tau v_z} \sec \theta} dt \right] + \\ &+ \frac{2\pi e^2 m^2}{h^3} \int_0^\infty v^2 \frac{\partial f_0}{\partial v} dv \int_{\frac{\pi}{2}}^\pi \sin^3 \theta \sec \theta d\theta \int_z^\infty E(t) e^{-\frac{(1+i\omega\tau)(t-z)}{\tau v_z} \sec \theta} dt. \end{aligned} \quad (A26)$$

When integrating on v , the fact that the electron gas is degenerated, where $\bar{v}^2 = \overline{v^2}$, needs to be considered. After a simple transformation the expression is

$$J(z) = -\frac{2\pi e^2 m^2 \bar{v}^2}{h^3} p \int_{-\infty}^{+\infty} k_a\left(\frac{z-t}{l}\right) E(t) dt - \frac{2\pi e^2 m^2 \bar{v}^2}{h^3} (1-p) \int_0^{\infty} k_a\left(\frac{z-t}{l}\right) E(t) dt, \quad (A27)$$

where $a = \omega\tau$, $l = \tau\bar{v}$ and

$$k_a(u) = Ei_1\{(1+ia)|u|\} - Ei_3\{(1+ia)|u|\}; \quad Ei_n(u) = \int_1^{\infty} \frac{e^{-su}}{s^n} ds. \quad (A28)$$

Once it is obtained we replace it into equation A4.

$$\frac{d^2 \vec{E}}{dz^2} + \frac{\omega^2}{c^2} \vec{E} = \frac{8\pi^2 i \omega e^2 m^2 \bar{v}^2}{c^2 h^3} p \int_{-\infty}^{+\infty} k_a\left(\frac{z-t}{l}\right) E(t) dt + \frac{8\pi^2 i \omega e^2 m^2 \bar{v}^2}{c^2 h^3} (1-p) \int_0^{\infty} k_a\left(\frac{z-t}{l}\right) E(t) dt. \quad (A29)$$

This equation is simplified when adimensional coordinates such as $x = \frac{z}{l}$, $y = \frac{t}{l}$, $E(lx) = f(x)$, as well as $\alpha = \frac{8\pi^2 \omega e^2 m^2 \bar{v}^2}{c^2 h^3} l^3 = \frac{3}{2} \frac{l^3}{\delta^2}$ are introduced.

$$f''(x) + \frac{\omega^2 l^2}{c^2} f(x) =$$

$$= i\alpha \left[p \int_{-\infty}^{+\infty} k_a(x-y) f(y) dy + (1-p) \int_0^{\infty} k_a(x-y) f(y) dy \right]. \quad (A30)$$

To know the Z impedance it is not compulsory to solve $f(x)$, since:

$$Z = \frac{4\pi E(0)}{c H(0)} = -\frac{4\pi i\omega l}{c^2} \frac{f(0)}{f'(0)}. \quad (A31)$$

Classical theory

In this case we have that the mean free path is too little and as a consequence we can consider the electric field to be constant for practical reasons. Therefore, Equation A30 results in:

$$\begin{aligned} f''(x) + \frac{\omega^2 l^2}{c^2} f(x) &\simeq \\ &\simeq i\alpha f(x) \left[p \int_{-\infty}^{+\infty} k_a(x-y) dy + (1-p) \int_0^{\infty} k_a(x-y) dy \right] \simeq \\ &\simeq i\alpha f(x) \int_{-\infty}^{+\infty} k_a(u) du = \frac{4}{3} \frac{i\alpha}{1+i\omega\tau} f(x). \end{aligned} \quad (A32)$$

The $y'' + Ay = 0$ type equation is integrated so the impedance can be obtained. This way the solutions will be of the form $y = e^{iA^{\frac{1}{2}}x}$, and in this case:

$$A = \frac{\omega^2 l^2}{c^2} - \frac{4}{3} \frac{i\alpha}{1+i\omega\tau}. \quad (A33)$$

Obtaining $f(0)$ y $f'(0)$ and substituting in the equation A31:

$$Z_{cl} = R_{cl} + X_{cl} = \frac{4\pi\omega l}{c^2} \left(\frac{\omega^2 l^2}{c^2} - \frac{4}{3} \frac{i\alpha}{1 + i\omega\tau} \right)^{-\frac{1}{2}}, \quad (A34)$$

where:

$$\frac{\omega^2 l^2}{c^2} = \omega^2 \tau^2 \left(\frac{\bar{v}}{c} \right)^2 \simeq 10^{-5} \omega^2 \tau^2. \quad (A35)$$

Since $\bar{v} = ct$ for a given metal, it will be possible of studying the case for different frequency ranges

For very low frequencies ($\omega\tau \ll 1$), we have that $\frac{\omega^2 l^2}{c^2} \ll \alpha$. This provokes the neglecting of terms such as $\frac{\omega^2 l^2}{c^2}$ and $i\omega\tau$. In this case:

$$Z_{cl} = \frac{\frac{4\pi\omega l}{c^2}}{\sqrt{-\frac{4i\alpha}{3}}} = \frac{\pi\omega l}{c^2} \sqrt{\frac{6}{\alpha}} (1 + i) \quad (A36)$$

$$R_{cl} = X_{cl} = \frac{\pi\omega l}{c^2} \sqrt{\frac{6}{\alpha}} = \sqrt{\frac{2\pi\omega}{c^2\sigma}}. \quad (A37)$$

At room temperature is valid up until around $\lambda > 10^{-4}m$, but for noble metals at liquid helium temperature they stop being valid at $\lambda \approx 10^{-1}m$.

For frequencies around $\omega\tau \simeq 1$ the term $\frac{\omega^2 l^2}{c^2}$ keeps being neglected.

The resistance and reactance values are the following ones:

$$R_{cl} = \sqrt{\frac{2\pi\omega}{c^2\sigma}} \sqrt{-\omega\tau + \sqrt{1 + \omega^2\tau^2}} \quad (A38)$$

$$X_{cl} = \sqrt{\frac{2\pi\omega}{c^2\sigma}} \sqrt{\omega\tau + \sqrt{1 + \omega^2\tau^2}}. \quad (A39)$$

In the case where $\omega\tau \gg 1$:

$$R_{cl} = \sqrt{\frac{\pi}{c^2\tau\sigma}} \quad (A40)$$

$$X_{cl} = 2\omega\tau \sqrt{\frac{\pi}{c^2\tau\sigma}}. \quad (A41)$$

For high frequencies $\frac{\omega^2 l^2}{c^2}$ cannot be neglected and it can even become a dominant term. The critical frequency in which this happens is when $\frac{\omega^2 l^2}{c^2} = \frac{4\alpha}{3\omega\tau}$, where the dielectric function is zero and the metal becomes transparent.

From A34 it can be inferred that both R and X have a maximum at this critical frequency:

$$R_{max} = X_{max} = \frac{4\pi(\pi\tau\sigma)^{\frac{1}{4}}}{c}. \quad (A42)$$

General solutions

For the study of general solution the case where $p = 1$ will be considered. In the case of $p = 1$ we have that A30 becomes:

$$f''(x) + \frac{\omega^2 l^2}{c^2} f(x) = i\alpha \int_{-\infty}^{+\infty} k_a(x-y)f(y)dy. \quad (A43)$$

The equation is solved by assuming that the function $f(x)$ can be integrated in all the range and that it tends to zero when $x \rightarrow \infty$. Moreover,

both $f(x)$ and $f''(x)$ are continuous in the entire x interval and so is $f'(x)$ except for $x = 0$. $f'(x)$ will tend to a value μ when $x \rightarrow 0^+$ and $-\mu$ when $x \rightarrow 0^-$.

In order to proceed we need to introduce the following transforms:

$$\phi(t) = \int_{-\infty}^{+\infty} f(x)e^{-ixt} dx = 2 \int_0^{\infty} \cos(xt) f(x) dx \quad (A44)$$

$$k_a(t) = \int_{-\infty}^{\infty} k_a(x)e^{-ixt} dx . \quad (A45)$$

We integrate by parts:

$$\begin{aligned} \int_{-\infty}^{+\infty} f(x)e^{-ixt} dx &= -\frac{1}{it} f(x)e^{-ixt} \Big|_{-\infty}^{+\infty} + \int_{-\infty}^{+\infty} \frac{1}{it} f'(x)e^{-ixt} dx = \\ &= \frac{f'(x)}{t^2} e^{-ixt} \Big|_{-\infty}^{+\infty} - \int_{-\infty}^{+\infty} \frac{1}{t^2} f''(x)e^{-ixt} dx, \end{aligned} \quad (A46)$$

and

$$\int_{-\infty}^{+\infty} f''(x)e^{-ixt} dx = -t^2 \int_{-\infty}^{+\infty} f(x)e^{-ixt} dx = -t^2 \phi(t) - 2\mu . \quad (A47)$$

On the other hand, when we part from Equation A43 we have that:

$$\begin{aligned} \int_{-\infty}^{+\infty} f''(x)e^{-ixt} dx &= -\frac{\omega^2 l^2}{c^2} \phi(t) + \\ &+ i\alpha \int_{-\infty}^{+\infty} e^{-ixt} dx \int_{-\infty}^{+\infty} k_a(x-y)f(y) dy . \end{aligned} \quad (A48)$$

The integration needs to be permuted:

$$\int_{-\infty}^{+\infty} f''(x)e^{-ixt} dx = -\frac{\omega^2 l^2}{c^2} \phi(t) + i\alpha k_a(t)\phi(t). \quad (A49)$$

Then we match both results to obtain

$$-2\mu = \left[t^2 - \frac{\omega^2 l^2}{c^2} + i\alpha k_a(t) \right] \phi(t). \quad (A50)$$

If we go back to Equation A44 we do the inverse transformation:

$$\begin{aligned} f(x) &= \frac{1}{\pi} \int_0^{+\infty} \phi(t) \cos(xt) dt = \\ &= \frac{2\mu}{\pi} \int_0^{\infty} \frac{\cos(xt)}{t^2 - \frac{\omega^2 l^2}{c^2} + i\alpha k_a(t)} dt. \end{aligned} \quad (A51)$$

Afterwards we make a variable change with $s = it$ so $k_a(t) = K_a(s)$, which allows us using the following transformation:

$$K_a(s) = \int_{-\infty}^{+\infty} k_a(x)e^{-sx} dx = \frac{1}{1 + i\omega\tau} K\left(\frac{s}{1 + i\omega\tau}\right), \quad (A52)$$

where how $k_a(u)$ is defined has been taken into account and that the change from $K_a(s)$ to $K(s)$ is when $a = 0$.

This last equation can be written in an explicit way:

$$K(s) = \frac{1}{s^3} \left[2s - (1 - s^2 \ln\left(\frac{1+s}{1-s}\right)) \right]. \quad (A53)$$

The function is monovaluated in the entire s range that goes from $-\infty$ to -1 and from $+1$ to $+\infty$. Then we have that A51 is:

$$f(x) = \frac{2}{\pi} f'(0) \int_0^{\infty} \frac{\cos(xt)}{t^2 - \frac{\omega^2 l^2}{c^2} + \frac{i\alpha}{1 + i\omega\tau} K\left(\frac{it}{1 + i\omega\tau}\right)} dt. \quad (A54)$$

Thanks to that we are able to obtain:

$$\frac{f(0)}{f'(0)} = \frac{2}{\pi} \int_0^{\infty} \frac{dt}{t^2 - \frac{\omega^2 l^2}{c^2} + \frac{i\alpha}{1 + i\omega\tau} K\left(\frac{it}{1 + i\omega\tau}\right)} \quad (A55)$$

and from there we have the impedance:

$$Z = -\frac{8i\omega l}{c^2} \int_0^{\infty} \frac{dt}{t^2 - \frac{\omega^2 l^2}{c^2} + \frac{i\alpha}{1 + i\omega\tau} K\left(\frac{it}{1 + i\omega\tau}\right)}. \quad (A56)$$

Optical region

When studying high frequencies (infrared), the integration must be done without neglecting the $\omega\tau$ terms, which makes the calculations much more difficult. In our case we will again use the case where $p = 1$.

We are going to study the difference between the behaviors of R and R_{cl} . We part from the impedance (where the $\frac{\omega^2 l^2}{c^2}$ terms are neglected):

$$\begin{aligned} Z &= -\frac{4\pi i\omega l}{c^2} \frac{f(0)}{f'(0)} = \frac{8i\omega l}{c^2} \frac{1}{1 + i\omega\tau} \int_0^{\infty} \frac{dt}{t^2 + \frac{i\alpha}{(1 + i\omega\tau)^3} k(t)} = \\ &= \frac{8i\omega l}{c^2} \frac{1}{1 + i\omega\tau} I = \frac{8i\omega l}{c^2} \frac{1 - i\omega\tau}{1 + \omega^2\tau^2} I; \end{aligned}$$

$$I = \int_0^{\infty} \frac{dt}{t^2 + \frac{i\alpha}{(1+i\omega\tau)^3} k(t)} \quad (A57)$$

$$Z = \frac{8\omega l}{c^2} \frac{1}{1 + \omega^2\tau^2} [\omega\tau + i][Re(I) + iIm(I)] \quad (A58)$$

$$\begin{aligned} Z &= \left(\frac{8\omega l}{c^2} \frac{1}{1 + \omega^2\tau^2} \right) \{ [\omega\tau Re(I) - Im(I)] + i[\omega\tau Im(I) + Re(I)] \} = \\ &= R + iX. \end{aligned} \quad (A59)$$

Then we have the following quotients:

$$\begin{aligned} \frac{R}{R_{cl}} &= \frac{8\omega l}{c^2} \frac{1}{\sqrt{\frac{2\pi\omega}{c^2\sigma}}} \frac{1}{1 + \omega^2\tau^2} \frac{1}{\sqrt{-\omega\tau + \sqrt{1 + \omega^2\tau^2}}} \frac{[\omega\tau Re(I) - Im(I)]}{\sqrt{-\omega\tau + \sqrt{1 + \omega^2\tau^2}}}; \quad \sigma = \frac{c^2}{\delta^2 2\pi\omega} \\ \frac{R}{R_{cl}} &= \frac{4}{\pi} \sqrt{\frac{2\alpha}{3}} \frac{[\omega\tau Re(I) - Im(I)]}{(1 + \omega^2\tau^2)\sqrt{-\omega\tau + \sqrt{1 + \omega^2\tau^2}}}. \end{aligned} \quad (A60)$$

We analogously obtain a formula for the reactance:

$$\frac{X}{X_{cl}} = \frac{4}{\pi} \sqrt{\frac{2\alpha}{3}} \frac{[\omega\tau Im(I) + Re(I)]}{(1 + \omega^2\tau^2)\sqrt{\omega\tau + \sqrt{1 + \omega^2\tau^2}}}. \quad (A61)$$

Now we only need to obtain the emissivity which is given by the following formula [63]:

$$\varepsilon = \frac{cR}{\pi}. \quad (A62)$$

Bibliography

1. L. del Campo; *Diseño, construcción y calibración de un radiómetro para medir emisividad espectral direccional. Aplicación a materiales de interés tecnológico*; Ph.D. Dissertation, Universidad del País Vasco, Leioa (2007).
2. L. del Campo, R.B. Pérez-Sáez, X. Esquisabel, I. Fernández, M.J. Tello, *New experimental device for infrared spectral directional emissivity measurements in a controlled environment*, Review of Scientific Instruments **77** (2006) 133111.
3. E.T. Kwor, S. Matteï, *Emissivity measurements for Nextel Velvet Coating 811-21 between -36 and 82 °C*, High Temperature – High Pressures **33** (2001) 551-556.
4. L. del Campo, D. De Sousa Meneses, A. Blin. B. Rousseau, E. Veron, M. Balat-Pichelin, P. Echegut, *High-Temperature Radiative Properties of an Yttria-Stabilized Hafnia Ceramic*, Journal of the Ceramic Society **94**, 6 (2011) 1859-1864.
5. O. Rozenbaum, D. De Sousa Meneses, Y Auger, S. Chermane, P. Echegut, *A spectroscopic method to measure the spectral emissivity of semi-transparent materials up to high temperature*, Review of Scientific Instruments **70**, 10 (1999) 4020-4025.
6. R.M. Sova, M.J. Linevsky, M.E. Thomas, F.F. Mark, *High-temperature infrared properties of sapphire, AION, fused silica, yttria and spinel*, Infrared Physics and Technology **39** (1998) 251-261.
7. J. Ishii, A. Ono, *Uncertainty estimation for emissivity measurements near room temperature with a Fourier transform spectrometer*, Measurement Science and Technology **12** (2001) 2103-2112.

8. R.B. Pérez-Sáez, L. del Campo, M.J. Tello, *Analysis of the accuracy of the methods for the direct measurement of emissivity*, International Journal of Thermophysics **29** (2008) 1141-1155.
9. A. Shimota, H. Kobayashi, S. Kadodura, *Radiometric calibration for the airborne interferometric monitor for green house gases simulator*, Applied Optics **38** (1998) 5923-5931.
10. H.E. Revercomb, H. Buijs, H.B. Howel, D.D. LaPorte, W.L. Smith, L.A. Sromovsky, *Radiometric calibration of IR Fourier transform spectrometers: solution to a problem with the high-resolution interferometer sounder*, Applied Optics **27**, 15 (1988) 3210-3218.
11. E. Lindemeier, P. Haschberger, V. Thank, H. Dietl, *Calibration of Fourier transform spectrometer using three blackbody sources*, Applied Optics **31**, 22 (1992) 4327-4533.
12. S. Clausen, *Measurements of spectral emissivity by FT-IR spectrometer*, Proceeding of the 8th Symposium on Temperature and Thermal Measurements in Industry and Science, TEMPMEKO 2001 258-264.
13. J. Dai, X. Wang, G. Yuan, *Fourier transform spectrometer for spectral emissivity measurements in the temperature range between 60 and 1500 °C*, Journal of Physics Conference Series **13** (2005) 63-66.
14. D.B. Chase, *The sensitivity and limitations of condensed phase infrared emission spectroscopy*, Applied Spectroscopy **35** (1981) 77-81.
15. F.J. DeBlase, S. Compton, *Infrared emission spectroscopy: a theoretical and experimental review*, Applied Spectroscopy **45** (1991) 611-618.
16. P.C. Dufour, N.L. Rowell, A.G. Steele, *Fourier transform radiation thermometry: measurements and uncertainties*, Applied Optics **37** (1998) 5923-5931.

17. L. González-Fernández, R.B. Pérez-Sáez, L. del Campo, M.J. Tello, *Analysis of calibration methods for direct emissivity measurements*, Applied Optics **49**, 14 (2010) 2728-2735.
18. L. del Campo, R.B. Pérez-Sáez, M.J. Tello, *Iron oxidation kinetics study by using infrared spectral emissivity measurements below 570 °C*, Corrosion Science **50** (2008) 194-199.
19. R. Siegel, J. Howell, *Thermal Heat Transfer*, 4th ed., Taylor and Francis, Washington, 2002.
20. M.A. Ordal, R.J. Bell, R.W. Alexander Jr., L.L. Long, M.R. Query, *Optical properties of fourteen metals in the infrared and far infrared: Al, Co, Cu, Au, Fe, Pb, Mo, Ni, Pd, Pt, Ag, Ti, V, and W*, Applied Optics **24** (1985) 4493-4499.
21. <http://www.korth.de/index.php/162/items/15.html>
22. <http://www.crystran.co.uk/optical-materials/potassium-bromide-kbr>
23. T.C. Tszeng, G.F. Zhou, *A dual-scale computational method for correcting surface temperature measurement errors*, Journal of Heat Transfer **126** (2004) 535-539.
24. M.F. Modest, *Radiative Heat Transfer*, 2nd ed., Academic Press, San Diego, 2003.
25. E.D. Palik (Ed.), *Handbook of Optical Constants of Solids*, Academic Press, San Diego, 1985.
26. M.A. Havstad, S.A. Self, *Sensitivities of measurement methods for the thermal radiative properties and optical constants of metals in the spectral range 0.4 to 10 μm*, International Journal of Thermophysics **14** (1993) 1077.
27. A.D. Rakic, A.B. Djuricic, J.M. Elazar, M.L. Majewski, *Optical properties of metallic films for vertical-cavity optoelectronic devices*, Applied Optics **37** (1998) 5271-5283.
28. H.J. Hagemann, W. Gudat, C. Kunz, *Optical constants from the far infrared to the x-ray region: Mg, Al, Cu, Ag, Au, Bi, C, and*

- Al_2O_3 , Journal of the Optical Society of America **65**, 6 (1975) 742-744.
29. H.J. Yu, G.Y. Xu, X.M. Shen, X.X. Yan, R. Huang, F.L. Li, *Preparation of leafing Cu and its application in low infrared emissivity coatings*, Journal of Alloys and Compounds **484** (2009) 395-399.
30. X. Yan, G. Xu, *Corrosion and mechanical properties of polyurethane/Al composite coatings with low infrared emissivity*, Journal of Alloys and Compounds **491** (2010) 649-653.
31. I. Setién-Fernández, T. Echániz, L. González-Fernández, R.B. Pérez-Sáez, E. Céspedes, J.A. Sánchez-García, L. Pérez-Fraga, R. Escobar Galindo, J.M. Albella, C. Prieto, M.J. Tello, *First spectral emissivity study of a solar selective coating in the 150-600 °C temperature*, Solar Energy Materials & Solar Cells **117** (2013) 390-395.
32. K.G. Ramanathan, S.H. Yen, E.A. Estalote, *Total hemispherical emissivities of copper, aluminum, and silver*, Applied Optics **16** (1977) 2810-2817.
33. R. Smalley, A.J. Sievers, *The total hemispherical emissivity of copper*, Journal of the Optical Society of America **68** (1978) 1516-1518.
34. E. Estalote, K.G. Ramanathan, *High-temperature emissivities of copper, aluminum and silver*, Journal of the Optical Society of America **67** (1977) 32-38.
35. E. Estalote, K.G. Ramanathan, *Low-temperature emissivities of copper and aluminum*, Journal of the Optical Society of America **67** (1977) 39-44.
36. H. Watanabe, M. Susa, K. Nagata, *Near-Infrared spectral emissivity of Cu, Ag and Au in the liquid and solid states at their melting points*, International Journal of Thermophysics **24** (2003) 1105-1120.

37. H. Watanabe, M. Susa, K. Nagata, *Discontinuity in normal spectral emissivity of solid and liquid copper at the melting point*, Metallurgical and Materials Transactions A **28** (1997) 2507-2513.
38. C. Cagran, G. Pottlacher, *Normal spectral emissivities of liquid copper, liquid gold and liquid silver at 684.5 nm*, Journal of Non-Crystalline Solids **353** (2007) 3582-3586.
39. K. Nagata, T. Nagana, M. Susa, *Measurement of normal spectral emissivity of liquid copper*, ISIJ International **37** (1997) 399-403.
40. W. Bauer, H. Oertel, M. Rink, *Spectral emissivities of bright and oxidized metals at high temperatures*, in: 15th Symposium on Thermophysical Properties, Boulder, CO, USA, 2003.
41. S.I. Woods, T.M. Jung, D.R. Sears, J. Yu, *Emissivity of silver and stainless steel from 80 K to 300 K: Application to ITER thermal shields*, Cryogenics **60** (2014) 44-48.
42. W. Sabuga, R. Todtenhaupt, *Effect of roughness on the emissivity of the precious metals silver, gold, palladium, platinum, rhodium and iridium*, High Temperatures – High Pressures **33** (2001) 261-269.
43. M. Misale, C. Pisone, G. Tanda, *Influence of surface finishing operation on total normal emittance of nickel and titanium*, International Journal of Heat and Technology **6** (1988) 97-110.
44. S.X. Cheng, *Total hemispherical emissivities of cobalt and nickel in the range 350-1000 K*, Experimental Thermal and Fluid Science **2** (1989) 165-172.
45. T. Makino, H. Kawasaki, *Study of the radiative properties of heat resisting metals and alloys (1st report, optical constants and emissivities of nickel, cobalt and chromium)*, Bulletin of the Japan Society of Mechanical Engineers **25** (1982) 804-811.

46. G. Teodorescu, P.D. Jones, R.A. Overfeld, B. Guo, *Normal emissivity of high purity nickel at temperatures between 1440 and 1605 K*, Journal of Physics and Chemistry of Solids **69** (2008) 133-138.
47. K. Boboridis, A. Seifert, A.W. Obst, D. Basak, *Radiance temperature and normal spectral emittance (in the wavelength range 1.5 to 5 μm) of nickel at its melting point by a pulse heating technique*, International Journal of Thermophysics **28** (2007) 683-696.
48. E. Kaschnitz, J.L. McClure, A.Cezairliyan, *Radiance temperatures (in the wavelength range 530 to 1500 nm) of nickel at its melting point by a falseheating technique*, International Journal of Thermophysics **19** (1998) 1637-1646.
49. S. Krishnan, P.C. Nordine, *Optical properties of liquid nickel and iron*, Physical Review B **55** (1997) 8201-8206.
50. X.M. Shen, L.S. Li, X.R. Wu, Z.F. Gao, G.Y. Xu, *Infrared emissivity of Sr doped lanthanum manganites in coating form*, Journal of Alloys and Compounds **509** (2011) 8116-8119.
51. C.D. Wen, I. Mudawar, *Emissivity characteristics of roughened aluminum alloy surfaces and assessment of multispectral radiation thermometry (MRT) emissivity models*, International Journal of Heat and Mass Transfer **47** (2004) 3591-3605.
52. L. del Campo, R.B. Pérez-Sáez, L. González-Fernández, M.J. Tello, *Combined standard uncertainty in direct emissivity measurements*, Journal of Applied Physics **107** (2010) 113510.
53. L. del Campo, R.B. Pérez-Sáez, M.J. Tello, X. Esquisabel, I. Fernández, *Armco iron normal spectral emissivity*, International Journal of Thermophysics **27** (2006) 1160-1172.
54. L. González-Fernández, E. Risueño, R.B. Pérez-Sáez, M.J. Tello, *Infrared normal spectral emissivity of Ti-6Al-4V alloy in*

- the 500-1150 K temperature range*, Journal of Alloys and Compounds **541** (2012) 144-149.
55. L. del Campo, R.B. Pérez-Sáez, L. González-Fernández, M.J. Tello, *Kinetics inversión in isothermal oxidation of uncoated WC-based carbides between 450 and 800°C*, Corrosion Science **51** (2009) 707-712.
 56. E. Hagen, H. Rubens, *Metallic Reflection*, Annals of Physics **1**, 2 (1900) 352-375.
 57. C.Y. Ho, M.W. Ackerman, K.Y. Wu, T.N. Havill, R.H. Bogaard, R.M. Matula, S.G. Oh, H.M. James, *Electrical resistivity of ten selected binary alloy systems*, Journal of Physical and Chemical Reference Data **12**, 2 (1983) 183-322.
 58. F.C. Schewerer, L.J. Cuddy, *Spin-disorder scattering in iron- and nickel-base alloys*, Physical Review B **2** (1970) 1575-1587.
 59. R.A. Matula, *Electrical resistivity of copper, gold palladium and silver*, Journal of Physical and Chemical Reference Data **8**, 4 (1977) 1147-1298.
 60. T.C. Chi, *Electrical resistivity of alkaline earth elements*, Journal of Physical and Chemical Reference Data **8**, 2 (1979) 439-498.
 61. A.B. Pippard, *The surface impedance of superconductors and normal metals at high frequencies. II. The anomalous skin effect in normal metals*, Proceedings of the Royal Society of London A **191** (1947) 385-399.
 62. A.B. Pippard, *The surface impedance of superconductors and normal metals at high frequencies. III. The relation between impedance and superconducting penetration depth*, Proceedings of the Royal Society of London A **191** (1947) 399-415.
 63. G.E.H. Reuter, E.H. Sondheimer, *The theory of anomalous skin effect in metals*, Proceedings of the Royal Society of London A **195** (1948) 336-364.

64. K.L. Kliewer, R. Fuchs, *Collective electronic motion in a metallic slab*, Physical Review **153** (1967) 498-512.
65. K.L. Kliewer, R. Fuchs, *Anomalous skin effect for specular electron scattering and optical experiments at non-normal angles of incidence*, Physical Review **172** (1968) 607-624.
66. R.B. Dingle, *The anomalous skin effect and the reflectivity of metals. I*, Physica **19** (1953) 311-347.
67. R.B. Dingle, *The anomalous skin effect and the reflectivity of metals. II. Comparison between theoretical and experimental optical properties*, Physica **19** (1953) 348-364.
68. R.B. Dingle, *The anomalous skin effect and the reflectivity of metals. Evaluation of the integrals appearing in the expressions for the surface impedance*, Journal of Applied Science Research Section B **3** (1954) 69-96.
69. J.G. Collins, *The theory of the anomalous skin effect in metals for obliquely incident radiation*, Journal of Applied Science Research Section B **7** (1959) 1-40.
70. D.C. Mattis, J. Bardeen, *Theory of anomalous skin effect in normal and superconducting metals*, Physical Review **111** (1958) 412-417.
71. N.W. Ashcroft, N.D. Mermin, *Solid State Physics*, Brooks/Cole, Belmont, 1976.
72. P.W. Gilbert, *The anomalous skin effect and the optical properties of metals*, Journal of Physics F: Metal Physics **12**, (1982) 1845-1860.
73. K. Fuchs, *The conductivity of thin metallic films according to the electron theory of metals*, Proceedings of the Cambridge Philosophical Society **34** (1938) 100-108.
74. H.E. Bennett, J.M. Bennett, E.J. Ashley, J. Motyka, *Verification of the anomalous-skin-effect theory for silver in the infrared*, Physical Review **165** (1968) 755-764.

75. M.L. Théye, *Investigation of the optical properties of Au by means of thin semitransparent films*, Physical Review B **2**, (1972) 3060-3078.
76. R.F. Greene, *Surface transport*, Surface Science **2** (1964) 101-113.
77. E.W. Johnson, H.H. Johnson, *Frequency dependence of the anomalous skin effect in high-purity copper*, Journal of Applied Physics **36** (1965) 1286-1288.
78. G.E. Smith, *Anomalous skin effect in bismuth*, Physical Review **115** (1959) 1561-1568.
79. K.L. Chopra, L.C. Bobb, M.H. Francombe, *Electrical resistivity of thin single-crystal gold films*, Journal of Applied Physics **34** (1963) 1699-1702.
80. D.C. Larson, B.T. Boiko, *Electrical resistivity of thin epitaxially grown silver films*, Applied Physics Letters **5** (1964) 155-156.
81. R.F. Greene, *Boundary conditions for electron distribution at crystal surfaces*, Physical Review **141** (1966) 687-688.
82. K.L.F. Bane, G. Stupakov, J.J. Tu, *Reflectivity measurements for copper and aluminum in the far infrared and the resistive wall impedance in the LCLS undulator*, in: Proceedings of European Particle Accelerator Conference (THPCH073), Edinburgh, Scotland, 2006.
83. H.E. Bennett, J.M. Bennett, *Optical properties and electronica structure of Metals and Alloys*, edited by F. Abeles, North-Holland Amsterdam, 1966.
84. M.A. Ordal, R.J. Bell, R.W. Alexander, L.A. Newquist, M.R. Querry, *Optical properties of Al, Fe, Ti, Ta, W, and Mo at submillimeter wavelengths*, Applied Optics **27** (1988) 1203-1209.

85. S. Edalatpour, M. Francoeur, *Size effect on the emissivity of thin films*, Journal of Quantitative Spectroscopy & Radiative Transfer **118** (2013) 75-85.
86. C.E. Kennedy, *Review of mid-to-high-temperature solar selective absorber materials*, NREL/TP-520-31267. Available from: <http://www.nrel.gov/docs/fy02osti/31267.pdf>
87. G.A. Niklasson, C.G. Granqvist, *Selective solar-absorbing surface coatings: optical properties and degradation*, in C.G. Granqvist (ed.), *Materials Science for Solar Energy Conversion Systems*, Pergamon Press, Oxford, 1991, p. 70.
88. M. Nejati, *Cermet based solar absorbers; further selectivity improvement and developing new fabrication technique*, Ph.D. Dissertation, Saarbrücken, 2008.
89. O.T. Inal, A. Sherer, *Optimization and microstructural analysis of electrochemically deposited selective solar absorber coatings*, Journal of Materials Science **21** (1986) 729-736.
90. L. Katulza, A. Surca-Voc, B. Orel, *Structural and IR spectroscopy analysis of sol-gel processed CuFeMnO_4 spinel and $\text{CuFeMnO}_4/\text{silica}$ films for solar absorbers*, Journal of Sol-Gel Science and Technology **20** (2001) 61-83.
91. Z.C. Orel, M.K. Gunde, *Spectral selective paint coatings preparation and characterization*, Solar Energy Materials & Solar Cells **68** (2001) 337-353.
92. M. Farooq, M.G. Hutchins, *A novel design in composites of various materials in solar selective coatings*, Solar Energy Materials & Solar Cells **71** (2002) 523-535.
93. I.T. Ritchie, B. Window, *Application of thin graded index films to solar absorbers*, Applied Optics **16** (1997) 1438-1443.
94. M.R. Nejati, V. Fathollahi, M.K. Asadi, *Computer simulation of the optical properties of high temperature cermet solar selective coatings*, Solar Energy **78** (2005) 235-241.

95. B.O. Seraphin, *Thin films in photothermal solar energy conversion*, Thin Solid Films **90** (1982) 395-403.
96. N. Selvakumar, H.C. Barshilia, *Review of physical vapor deposited (PVD) spectrally selective coatings for mid- and high-temperature solar thermal applications*, Solar Energy Materials & Solar Cells **98** (2012) 1-23.
97. Q.C. Zhang, *Recent progress in high-temperature solar selective coatings*, Solar Energy Materials & Solar Cells **62** (200) 63-74.
98. S. Esposito, A. Antonaia, M.I. Addonizio, S. Eprea, *Fabrication and optimization of highly efficient cermet-based spectrally selective coatings for high operating temperature*, Thin Solid Films **517** (2009) 6000-6006.
99. C.E. Kennedy, H. Price, *Progress in development of high-temperature solar-selective coatings*, NREL/CP-520-36997, in: Proceedings of the 2005 International Solar Energy Conference ISEC2005-76038, Orlando, Florida, USA, 2005.
100. C.G. Granqvist, *Transparent conductors as solar energy materials: a panoramic review*, Solar Energy Materials & Solar Cells **91** (2007) 1529-1598.
101. E. Céspedes, M. Wirz, J.A. Sánchez-García, L. Álvarez-Fraga, R. Escobar Galindo, C. Prieto, *Novel Mo-Si₃NO₄ based selective coating for high temperature concentrating solar power applications*, Solar Energy Materials & Solar Cells **122** (2014) 217-225.
102. P. Blanco-Rodriguez, J. Rodriguez-Aseguinolaza, E. Risueño, M.J. Tello, *Thermophysical characterization of Mg49-Zn51 eutectic metal alloy: a phase change material for heating energy storage in direct steam generation applications*, Energy **72** (2014) 414-420.
103. J. Rodriguez-Aseguinolaza, P. Blanco-Rodriguez, E. Risueño,

- M.J. Tello, S. Doppiu. *Thermodynamic study of the eutectic Mg₄₉Zn₅₁ alloy used for heating energy storage*, Journal of Thermal Analysis and Calorimetry **73** (2014) 93-99.
104. E. Risueño, A. Faik, J. Rodríguez-Aseguinolaza, P. Blanco-Rodríguez, A. Gil, M. Tello, B. D'Aguanno. *Mg-Zn-Al eutectic alloys as a phase change material for latent heat thermal energy storage*, Energy Procedia **69** (2015) 1006-1013.
105. C.E. Birchenall, NASA reports: *Heat storage in alloy transformations*, NASA report CR-159787 (1980). Available from: <http://ntrs.nasa.gov/archive/nasa/casi.ntrs.nasa.gov/19800016266.pdf>
106. C.E. Birchenall, A.F. Riechman. *Heat storage in eutectic alloys*, Metallurgical and Materials Transactions A **11** (1980) 1415-1420.
107. D. Farkas, C.E. Birchenall. *New eutectic alloys and their heats of transformation*, Metallurgical and Materials Transactions A **16** (1985) 323-328.
108. H. Okamoto. *Comment on Mg-Zn (Magnesium-Zinc)*, Journal of Phase Equilibria **15** (1994) 129-130.
109. P. Andonov, P. Chieux. *Structural study of eutectic Mg_{0.72}Zn_{0.28} alloy.1. Local order in the amorphous and liquid states comparison with the crystalline phase Mg₅₁Zn₂₀*, Journal of Non-Crystalline Solids **93** (1987) 331-349.
110. P. Andonov, P. Chieux. *Structural study of eutectic alloy Mg_{0.72}Zn_{0.28}. 2. Crystallization processes in the amorphous, liquid and undercooled states of the eutectic alloy Mg_{0.72}Zn_{0.28}*, Journal of Non-Crystalline Solids **108** (1989) 58-74.
111. I. Dinçer, M.A. Rosen. *Heating energy storage systems and applications*, Wiley, New York, 2002.
112. H.P. Garg. *Advances in solar energy technology*, Vol. 1. D. Reider/Kluwer, Dordrecht, 2010.

113. B. Zalba, J.M. Marin, L.F. Cabeza, H. Mehling. *Review on heating energy storage with phase change: materials, heat transfer analysis and applications*, Applied Thermal Engineering **23** (2003) 251–283.
114. M.M. Kenisarin. *High-temperature phase change materials for heating energy storage*, Renewable & Sustainable Energy Reviews **14** (2010) 955-970.
115. M. Liu, W. Saman, F. Bruno. *Review on storage materials and heating performance enhancement techniques for high temperature phase change heating storage systems*, Renewable & Sustainable Energy Reviews **16** (2012) 2118-2132.
116. A. Gil, M. Medrano, I. Martorell, A. Lazaro, P. Dolado, B. Zalba, L.F. Cabeza. *State of the art on high temperature heating energy storage for power generation. Part 1-concepts, materials and modelization*, Renewable & Sustainable Energy Reviews **14** (2010) 31-55.
117. A. Sharma, V.V. Tyagi, C.R. Chen, D. Buddhi. *Review on heating energy storage with phase change materials and applications*, Renewable & Sustainable Energy Reviews **13** (2009) 318-45.
118. F. Agyenun, N. Hewitt, P. Eames, M. Smyth. *A review of materials, heat transfer and phase change problem formulation for latent heat heating energy storage systems (LHTESS)*, Renewable & Sustainable Energy Reviews **14** (2010) 615-28.
119. R. Parameshwaran, R. Jayavel, S. Kalaiselvam. *Study on heating properties of organic ester phase-change material embedded with silver nanoparticles*, Journal of Thermal Analysis and Calorimetry **114** (2013) 845-58.
120. X. Meng, H. Zhang, L. Sun, F. Xu, Q. Jiao, Z Zhao, J. Zhang, H. Zhou, Y. Sawada, Y. Liu. *Preparation and heating properties of fatty acids/CNTs composite as shape-stabilized phase*

- change materials*, Journal of Thermal Analysis and Calorimetry. **111** (2013) 377-84.
121. S. Harikrishnan, K. Deepak, S. Kalaiselvam. *Heating energy storage behaviour of composite using hybrid nanomaterials as PCM for solar heating systems*, Journal of Thermal Analysis and Calorimetry **115** (2013) 1563-1571.
122. J.L. Zeng, Z. Cao, D.W. Yang, F. Xu, L.X. Sun, X.F. Zhang, L. Zhang. *Effects of MWNTS on phase change enthalpy and heating conductivity of a solid-liquid organic PCM*, Journal of Thermal Analysis and Calorimetry **95** (2009) 507-12.
123. D. Laing, C. Bahl, T. Bauer, D. Lehmann, W. D. Steinmann *Heating energy storage for direct steam generation*, Solar Energy **85** (2011) 627-633.
124. D. Laing, T. Bauer, N. Breidenbach, B. Hachmann, M. Johnson. *Development of high temperature phase-change-material storages*, Applied Energy **109** (2013) 497-504.
125. V. Zipf, A. Neuhaeuser, D. Willert, P. Nitz, S. Gschwander, W. Platzer. *High temperature latent heat storage with a screw heat exchanger: Design of prototype*, Applied Energy **109** (2013) 462–469.
126. W. Xiang, L. Hong-Mei, L. Xin-Lin, L. Li, Z. Yu-Feng. *Effect of cooling rate and composition on microstructures and properties of Zn-Mg alloys*, Transactions of Nonferrous Metals Society of China **17** (2007) 122-125.

Resumen en castellano

Dentro del marco industrial mundial y en del País Vasco en particular, el sector metalúrgico ha tenido y tiene un peso muy importante. En muchos de los materiales utilizados es vital conocer las pérdidas de calor por radiación, ya bien sea durante el proceso de obtención de éstos o mientras están en funcionamiento. Para ello es necesario estudiar las propiedades termorradiativas y ópticas de estos materiales, siendo la medida de la emisividad espectral la mejor forma de entender los procesos de radiación.

La tesis se planteó con tres objetivos muy concretos basados en que el laboratorio del Departamento de Física de la Materia Condensada de la UPV/EHU dispone de un radiómetro de alta precisión (HAIRL) que permite realizar medidas de emisión térmica espectrales y direccionales en el infrarrojo en función de la temperatura y en una atmósfera controlada.

El primer objetivo era completar los análisis que se hicieron hasta ahora sobre los métodos de medida, precisión de las medidas de emisividad y temperatura, sistema y parámetros de calibración, etc. (estudiado en el Capítulo 2). El segundo objetivo estaba dirigido a medidas espectrales de los metales puros entre 200 y 800 °C y al estudio del efecto skin anómalo en metales bajo emisivos (desarrollado en los Capítulos 3 y 4). El tercer objetivo estaba relacionado con los materiales utilizados en centrales termosolares para la absorción de la luz por un lado y para el almacenamiento térmico en otro, ya que es necesario conocer las pérdidas de calor por radiación en ambos casos y en la literatura no se encontraban estudios a temperatura de trabajo (realizado en los Capítulos 5 y 6).

A continuación se hace un breve resumen de los cinco capítulos presentados:

Experimental: métodos de medida y calibración. En este capítulo se indican las principales características del radiómetro HAIRL (diseñado y construido en el laboratorio) utilizado para las medidas de emisividad, las cuales son la base experimental fundamental en esta tesis. Además, se describen brevemente los métodos de medida y de calibración del aparato utilizados previamente. Estos métodos han sido analizados y completados para realizar esta memoria. Las modificaciones introducidas permiten hacer más precisa la medida de la emisividad espectral. Esta mejora es muy notable para los materiales bajoemisivos como los estudiados en este trabajo, donde la radiación emitida por la muestra puede llegar a ser del orden de magnitud de las radiaciones espurias que son detectadas también por el radiómetro. Además, se analizan y añaden otras contribuciones. Por ejemplo, un método de medida de temperatura alternativo a la soldadura intrínseca utilizada anteriormente para muestras metálicas y un método para la integración de los espectros de emisividad.

Emisividad espectral de metales puros. La ausencia de estudios en los que aparezcan bien definidas las condiciones experimentales de la emisividad espectral en función de la temperatura de la mayoría de los metales puros ha impulsado el trabajo presentado en este capítulo. Aquí se presentan brevemente las medidas de emisividad del cobre, la plata, el níquel y el magnesio, cuatro metales presentes, tanto en su estado puro como en aleaciones, en diversas aplicaciones industriales. Entre otros aspectos, se estudia la relajación de tensiones superficiales producidas en el mecanizado de las muestras, así como las dependencias con la temperatura y la longitud de onda de la emisividad. Además, se analizan las curvas de emisividad dentro de la aproximación clásica dada por la función de Hagen-Rubens. Esto ha

permitido obtener valores de la resistividad eléctrica y compararlos con los encontrados en la bibliografía. Por último, pensando en aplicaciones industriales, se hace un cálculo de la emisividad normal total y se observa su dependencia lineal con la temperatura.

Propiedades ópticas de metales: el efecto skin anómalo. En metales con una conductividad eléctrica muy alta, el recorrido libre medio de los electrones de conducción puede ser del orden de la profundidad de penetración del campo eléctrico. En estos casos la aproximación de Drude de campo constante deja de ser válida y surge el efecto skin anómalo. Cuando se resuelven las ecuaciones de transporte con una fuerza debida al campo eléctrico que depende del tiempo, se observa que en el caso de reflexión especular aparece un mínimo en la reflectividad, el cual hasta ahora no se ha detectado experimentalmente. Solo existen indicios de su existencia. En este capítulo se hace un análisis teórico del efecto skin anómalo para los doce metales puros con mayor conductividad eléctrica (los cálculos detallados se desarrollan en el Apéndice I). En el caso del cobre el análisis es más detallado con el fin de obtener el comportamiento de la emisividad con la temperatura y el ángulo de emisión. En la parte experimental se observa que las medidas experimentales de la emisividad espectral del cobre a 250 °C, muestran un máximo del mismo orden y en la misma región que aquél predicho por la teoría del efecto skin anómalo. Este resultado es una evidencia de la presencia de este fenómeno incluso a altas temperaturas donde el efecto es más débil.

Emisividad de recubrimientos selectivos para la energía termosolar a temperatura de trabajo. Uno de los problemas más importantes a los que se enfrenta la industria de la energía termosolar es el desarrollo de recubrimientos selectivos capaces por un lado, de ser capaces de absorber la mayoría de la radiación proveniente del sol, y por otro, de tener la menor cantidad de pérdidas por irradiación infrarroja.

Los recubrimientos están formados por un conjunto de capas de espesor nanométrico en donde destacan las de nanocomposites cerámico-metálicos. Hasta el trabajo realizado como parte de esta tesis no se había planteado la necesidad de caracterizar las propiedades ópticas de estos recubrimientos a la temperatura de trabajo. Las propiedades ópticas del recubrimiento a alta temperatura se extrapolaban de los resultados a temperatura ambiente admitiendo que el recubrimiento no presentaba un comportamiento anómalo con la temperatura. En este capítulo se obtienen por primera vez medidas de emisividad infrarroja espectral, así como total, de recubrimientos entre 200 y 600 °C. Además se muestra la necesidad de medir a temperatura de trabajo ya que las extrapolaciones pueden llevar a errores que repercuten *a posteriori* en la eficiencia y como consecuencia en el rendimiento económico de estos recubrimientos.

Emisividad de aleaciones de cambio de fase de tipo Mg-Zn-Al para el almacenamiento térmico de la energía termosolar. Este capítulo pone la mirada en el otro gran problema que presenta la energía termosolar: el almacenamiento térmico. Hoy día el almacenamiento térmico se hace con sales inorgánicas las cuales a pesar de que su precio aún no es alto, almacenan energía haciendo uso del calor sensible. Este hecho presenta, entre otros, dos problemas: grandes dimensiones de complejos sistemas de almacenamiento y un rendimiento pobre. Desde hace años se están estudiando materiales con cambio de fase (PCMs) que el almacenamiento de energía por calor latente. En este capítulo se estudian, con medidas de emisividad, el comportamiento de tres aleaciones eutécticas pertenecientes al sistema Mg-Zn-Al. Estas aleaciones poseen una buena conductividad térmica y alta densidad energética. Se ha medido la emisividad espectral y total infrarroja entre 200 °C y la temperatura de fusión. Este estudio forma parte de un marco en donde es necesario conocer las pérdidas

por radiación de los materiales utilizados para almacenamiento térmico. Además, se ha puesto en evidencia la sensibilidad de las medidas de emisividad en las transiciones de fase sólido-sólido resultado que demuestra la alta sensibilidad del radiómetro utilizado.

Agradecimientos

Cuando estaba en el último año de la carrera, el profesor Ángel López Echarri me dio una lista de profesores con los cuales podía hacer el trabajo de fin de grado en un laboratorio. Decidí ir a hablar con Raúl, y en el momento en el que le comenté lo que buscaba dejó de lado todo lo que estaba haciendo y estuvo más de una hora hablándome del mundo de la emisividad. Yo, que en mi vida había oído tal palabro y que en el momento tampoco me cautivó, vi que se me presentaba una oportunidad de oro ante un profesor con tal atención, humildad y entusiasmo, por lo que no dudé en embarcarme en el proyecto. Junto a él he tenido de director de tesis estos años a Manolo, *alma mater* del Departamento de Física de la Materia Condensada, cuya predisposición a ayudarme no tenía nada que envidiarle a la de Raúl. El trabajar día a día con ellos estos últimos cinco años me ha demostrado que lo importante no es el destino que uno elige, si no con quién comparte el camino. Mi relación con ellos ha trascendido la de alumno-director y por ello les voy a estar agradecido toda la vida.

Gracias también a todos los doctorandos que me han acompañado estos años. En especial a Peio, por haberme aguantado desde los inicios de la carrera y haber estado ahí en todo momento (*eutsi gogor!*). También a Luis por haber ejercido de mentor en el laboratorio, por su paciencia y su capacidad de resolver cualquier problema y a Iñigo por haber compartido conmigo en los tres primeros años de laboratorio codo con codo. Y por supuesto a Gerardo, con quien he compartido grandes momentos dentro y fuera de la facultad, y a Sofía y Gemma por haberme alegrado las mañanas con las charlas en el becádro. Gracias a Iñaki y a Unai por haberme ayudado con el mecanizado de muestras siempre que lo he necesitado.

No me puedo olvidar tampoco de los profesores de la facultad que me han ayudado. Gracias en especial al profesor Tomasz Breczewski por haberme ayudado con el diseño de sistemas de calentamiento y con las medidas de DSC. También quiero agradecer a los profesores Ángel López Echarri e Isabel Ruiz Larrea por haberme permitido instalarme en su laboratorio y por haberme prestado material necesario para los experimentos, así como a José María San Juan por permitirme acceder a sus laboratorios de metalurgia.

He de agradecer además a todo el equipo de almacenamiento térmico del CIC energiGUNE y en especial a Elena Risueño, por haberme permitido participar en su proyecto de aleaciones para el almacenamiento térmico y por haberme ayudado en todo aquello que necesitaba. Del mismo modo tengo que agradecer al profesor Jose María Albella y a los investigadores Carlos Prieto y Ramón Escobar por haberme permitido trabajar con el ICMM en Madrid y por haber colaborado en el proyecto de láminas delgadas selectivas. Muchísimas gracias también a Leire y a Aurélien por haberme acogido durante mi estancia en Orléans durante tres meses y haberme permitido trabajar y aprender en el CEMTHI. No podía haber recibido un trato mejor.

Agradezco además la ayuda otorgada por el Gobierno Vasco en forma de una beca predoctoral sin la cual no hubiera realizado esta tesis.

Tengo que agradecer tanto o más que a nadie a mi madre Marisabel y a mi padre Álvaro por haberme inculcado desde pequeño la curiosidad por el conocimiento, por haberme empujado a hacer una tesis y por haberme apoyado en todo momento. También a mi hermano, que aún desde la distancia se preocupa siempre por mis progresos y sirve como apoyo necesario.

Por último, quiero acordarme de mi amor, Amalia, la cual me ha acompañado en la trayectoria final de esta tesis y que se ha preocupado sin parar por mí y mi labor. Ha sido y es todo lo que necesito.

Eskerrak benetan danori.

Publications

Part of the work presented here has been published in the following references:

1. I. Setién-Fernández, T. Echániz, L. González Fernández, R.B. Pérez Sáez, M.J. Tello. *Spectral emissivity of copper and nickel in the mid-infrared range between 250 and 900 °C*, Journal of Heat and Mass Transfer **71** (2014) 549-554.
2. T. Echániz, I. Setién-Fernández, R.B. Sáez, M.J. Tello. *Experimental verification of the anomalous skin effect in copper using emissivity measurements*, Applied Physics Letters **102** (2013) 244106.
3. T. Echániz, R.B. Pérez-Sáez, M.J. Tello. *Optical properties of metals: infrared emissivity in the anomalous skin effect spectral region*, Journal of Applied Physics **116** (2014) 093508.
4. I. Setién-Fernández, T. Echániz, L. González-Fernández, R.B. Pérez-Sáez, E. Céspedes, J.A: Sánchez-García, L. Pérez-Fraga, R. Escobar Galindo, J.M. Albella, C. Prieto, M.J. Tello, *First spectral emissivity study of a solar selective coating in the 150-600 °C temperature*, Solar Energy Materials & Solar Cells **117** (2013) 390-395.
5. T. Echániz, I. Setién-Fernández, R.B. Pérez-Sáez, C. Prieto, R. Escobar Galindo, M.J. Tello. *Importance of the spectral emissivity measurements at working temperature to determine the efficiency of a solar selective coating*, Solar Energy Materials & Solar Cells **140** (2015) 249-252.

